CHRONIC INFLAMMATION SURROUNDING INTRA-CORTICAL ELECTRODES IS CORRELATED WITH A LOCAL NEURODEGENERATIVE STATE

A Thesis
Presented to
The Academic Faculty

by

George Charles McConnell

In Partial Fulfillment
of the Requirements for the Degree
Doctor of Philosophy in the
School of Biomedical Engineering

Georgia Institute of Technology
December 2008

CHRONIC INFLAMMATION SURROUNDING INTRA-CORTICAL ELECTRODES IS CORRELATED WITH A LOCAL NEURODEGENERATIVE STATE

Approved by:

Dr. Ravi V. Bellamkonda, Advisor
School of Biomedical Engineering
Georgia Institute of Technology

Dr. Julie E. Babensee
School of Biomedical Engineering
Georgia Institute of Technology

Dr. Robert J. Butera
School of Electrical and Computer Engineering
Georgia Institute of Technology

Dr. Stephen P. DeWeerth
School of Biomedical Engineering
Georgia Institute of Technology

Dr. Robert H. Lee
School of Biomedical Engineering
Georgia Institute of Technology

Dr. Robert J. McKeon
Department of Cell Biology
Emory University

Date Approved: 13 November 2008

ACKNOWLEDGEMENTS

This dissertation would not exist without the guidance, encouragement, and support of many individuals.

First, I would like to express my gratitude for my advisor, Dr. Ravi V. Bellamkonda. He has given me the freedom, the resources, and the guidance so that I could become a confident researcher. He never turned down my purchase requests. He has taught me many important lessons, which have made me a better scientist and will serve me in my future endeavors. I will always be grateful to him for modeling for me a mindset of centering everything that I do in research around paper writing.

I would also like to thank the members of my thesis committee, Dr. Julie E. Babensee, Dr. Robert J. Butera, Dr. Stephen P. DeWeerth, Dr. Robert H. Lee, and Dr. Robert J. McKeon, for the valuable feedback they have given me in my research. I have been the beneficiary of the many hours they have spent critiquing my work, and the different perspectives that each one has brought to this research.

There are many in the Neurolab who have helped me while a grad student. I would like to thank especially the members of the DeWeerth and Butera groups for the advice that they have given me in all things electrical, especially Edgar Brown, Dr. Jim Ross, Dr. Murat Sekerli, and Ben Haeffele.

To all my friends in the Bellamkonda Group (aka NeuroBAT), thank you for all of your encouragement and criticism along the way. Isaac Clements and Dr. Katie McNeeley were exceptional writing room roommates, always ready to help when I needed it. Several talented post-docs in the lab have inspired me with their level of excellence as scientists. Dr. Wei He taught me so much about the importance of teamwork, because she's such a great example, and was instrumental in my studies.

Dr. Yinghui Zhong gave me an appreciation for the complexity of the tissue response to microelectrode arrays. Dr. Young-tae Kim inspired me with his amazing work ethic and was always eager to teach me a technique (like immunohistochemistry) or advice on how to be a successful grad student. Dr. Rupal Thazhath always asked me thought-provoking questions and gave me an incredible deal on her computer. Dr. Anjana Jain obviously took Dr. Bellamkonda's advice, since she's so good at making others around her better and I've valued working with her. Dr. Efstathios Karathanasis and Dr. Lohitash Karumbaiah have given me good advice time and time again (in addition to many laughs). Michael Tanenbaum has always been ready to lend me a helping hand, for which I'm very grateful. Douglas Swehla has ordered many of my research supplies for which I'm thankful.

Dr. Laura O'Farrell played a significant role in helping me develop the in vivo surgical methods and even drove me to Georgia State to watch a surgery. I appreciate the friendly staff in the PRL and their patience with me (especially in the beginning).

Dr. Allan I. Levey has provided me with expert advice on neurodegeneration, and I'm grateful for his collaboration. I appreciate the hospitality of the Levey group. It's been a pleasure to work with you. Dr. Howard D. Rees has been a great help to me with immunohistochemistry and is an exceptional teacher. Dr. Robert G. Gross kindly provided me with DBS tissue samples. Dr. Claire-Anne Gutekunst has been helpful in getting these samples to me.

I would like to thank my friends at Sovereign Grace Church for all of your prayers and encouragement, especially my pastors John Butler, Aaron Anderson, and Chad Rogers.

My parents, George and Harriet, have always encouraged me in whatever I set my mind to do. I could never thank them enough. They'll make wonderful grandparents for Lincoln... who deserves acknowledgement for not wanting to leave his Mommy until induced, thus giving me two unexpected weeks post-due date of "no baby yet, I

should take advantage of this silence and keep writing". My sister, Kelly, always told me I could be a Dr. I believe her pre-school classes helped. I love you all.

Finally, to my beautiful wife, Chris, thank you for being my best friend and giving me laughs everyday. It truly is a joy to be your husband. I'll always remember the sacrifices you've made in order to allow me to complete my degree. I love you most of all.

TABLE OF CONTENTS

LIST OF TABLES

LIST OF FIGURES

LIST OF SYMBOLS OR ABBREVIATIONS

AD	Alzheimer's Disease.
α	Angle of depression ranging between 0 and 1.
α-**MSH**	α-Melanocyte-stimulating Hormone.
ALS	Amyotrophic Lateral Sclerosis.
BIA	Body Impedance Analysis.
CNS	Central Nervous System.
Coll I	Collagen Type I.
DAPI	4',6-diamidino-2-phenylindole.
ECM	Extracellular Matrix.
f_c	Characteristic frequency.
GBWP	Gain Bandwidth Product.
GFAP	Glial Fibrillary Acid Protein.
GluR1	Glutamate Receptor 1.
IL-1	Interleukin-1.
IL-6	Interleukin-6.
LbL	Layer-by-layer.
LCM	Laser Cutting Microscopy.
LN	Laminin.
MAP-2	Microtubule-associated Protein 2.
MCP-1	Monocyte Chemotactic Protein-1.
MEA	Multielectrode Array.
NADPH	Nicotinamide Adenine Dinucleotide Phosphate.
NF-200	Neurofilament 200kDa.
NO	Nitric Oxide.
PBS	Phosphate Buffered Saline.

PD	Parkinson's Disease.
PEI	Polyethyleneimine.
pT231	PhosphoThreonine 231.
R_∞	Resistance at infinite frequency.
R_o	Resistance at zero frequency.
Si	Silicon.
SPICE	Simulation Program with Integrated Circuit Emphasis.
TNF-α	Tumor Necrosis Factor α.

SUMMARY

Thanks to pioneering scientists and clinicians, prosthetic devices that are controlled by intra-cortical electrodes recording one's 'thoughts' are a reality today, and no longer merely in the realm of science fiction. However, widespread clinical use of implanted electrodes is hampered by a lack of reliability in chronic recordings, independent of the type of electrodes used. The dominant hypothesis has been that astroglial scar electrically impedes the electrodes. However, recent studies suggest that the impedance changes associated with the astroglial scar are not high enough to interfere significantly impair neural recordings. Furthermore, there is a time delay between when scar electrically stabilizes and when neural recordings fail (typically >1 month lag), suggesting that scar, per se, does not cause chronic recording unreliability. In this study, an alternative hypothesis was tested in a rat model, namely, that chronic inflammation surrounding microelectrodes causes a local neurodegenerative state. Chronic inflammation was varied in three ways: 1) stab wound control, 2) age-matched control, and 3) inter-shank spacing of a multishank electrode. The results of this study suggest that chronic inflammation, as indicated by activated microglia and reactive astrocytes, is correlated with local neurodegeneration, marked by neuron cell death and dendritic loss. Surprisingly, axonal pathology in the form of hyperphosphorylation of the protein Tau (the hallmark of many tauopathies, including Alzheimer's Disease) was also observed in the immediate vicinity of microelectrodes implanted for 16 weeks. Additionally, work is presented on a fast, non-invasive method to monitor the astrocytic response to intra-cortical electrodes using electrical impedance spectroscopy. This work provides a non-invasive monitoring tool for inflammation, albeit an indirect one, and fills a gap which has slowed the development

of strategies to control the inflammatory tissue response surrounding microelectrodes and thereby improve the reliability of chronic neural recordings. The results of these experiments have significance for the field of neuroengineering, because a more accurate understanding of why recordings fail is integral to engineering reliable solutions for integrating brain tissue with microelectrode arrays.

CHAPTER I

INTRODUCTION

1.1 Statement of Problem

A variety of modalities for brain-computer interfaces (BCIs) have been proposed, including functional magnetic resonance imaging (fMRI), near-infra red (NIR) imaging, electroencephalography (EEG), intracranial electrodes, and intracortical electrode arrays. Among these, intracortical electrode arrays have several advantages for restoring voluntary motor control [59]. First, because the recordings are typically taken from the same brain center used to control voluntary limb movement prior to paralysis or amputation, prosthetic control can occur more naturally, without the need for extended training to learn new techniques. Second, this aspect also allows for the control to be performed independently of other activities, such as eating or talking. Finally, and particularly true for motor neuroprostheses, control signals from variables such as position, velocity, and force might all be used. However, the promise of intracortical electrodes has yet to be fully fulfilled due to their unreliability in providing stable chronic recordings. While the feasibility of long-term recordings from intracortical electrodes such as those from non-human primates has been demonstrated [135], the issue of recording reliability and chronic recording stability continues to thwart widespread clinical application of microelectrode recording technology.

The dominant hypothesis has been that astroglial scar electrically impedes the electrodes. However, recent studies suggest that the impedance changes associated with the astroglial scar are not high enough to interfere significantly impair neural recordings. Furthermore, there is a time delay between when scar electrically stabilizes and when neural recordings fail (typically >1 month lag), suggesting that scar,

per se, does not cause chronic recording unreliability.

1.2 Hypothesis

The primary hypothesis of this dissertation is that local chronic inflammation, due to electrode presence, causes local neurodegeneration.

Partly because of the dominant hypothesis involving astroglial scar-induced isolation of electrodes, most groups studying compatibility of neural electrodes have focused on characterizing and modulating glial scar with end points of 4 weeks [31, 7, 8, 127] with a few important exceptions looking at glial scar after 6 weeks [128, 131] and 12 weeks [142, 139, 79]. The rationale has been that there is little change in the composition or electrical properties of glial scar beyond this time point. Indeed in our group as well we have taken this approach and have successfully modulated scar formation at the end of 4-6 weeks [54, 55, 93].

However, we propose that scar tissue is 'chronically inflammatory' via its microglial and astrocytic constituents, although it may appear 'static' from an electrical impedance perspective. It is critical, therefore, to focus on evaluating neuronal state around the electrodes after at least 12 weeks for the important reason that recording loss often happens 8 weeks post-implantation or later, whereas scar stabilizes, from an electrical standpoint, within a period of 2-4 weeks. Moreover, it is critical that the fundamental molecular basis for recording loss be uncovered so appropriate strategies to prevent recording loss and enable stable recordings can be adopted.

1.3 Objectives

The goal of this work is to test the hypothesis that local chronic inflammation, due to electrode presence, causes local neurodegeneration. An outline of the work is as follows.

First, we establish a method for modulating the degree of chronic inflammation.

In Chapter III, we present data showing that narrowing the tip-to-tip spacing of multishank microelectrodes amplifies the chronic inflammatory response (after 4 weeks). We develop a means to control the degree of inflammation to microelectrode arrays through control of the intershank spacing of multi-shank silicon microelectrode arrays. We quantitatively study reactive microglia and reactive astrocytes, in relation to the electrode location, using immunohistochemical markers at 1 hour, 1 week and 4 weeks post-implant.

Second, in Chapter IV, we use the methods developed in Chapter III to evaluate the effect of the degree of inflammation on the neurodegenerative state. We investigate the level of inflammation, using a more extensive set of markers than that of Chapter III, at 2 weeks, and the more chronic time points of 8 weeks, and 16 weeks post-implant. At the most chronic time point of 16 weeks, we vary chronic inflammation in three ways: 1) stab wound control, 2) age-matched control, and 3) inter-shank spacing. We show that increased local inflammation results in increased local neurodegeneration through quantifying neurodegenerative markers (including neuronal viability, dendritic loss, and axonal pathology). As the primary goal of this thesis was to test for a correlation between chronic inflammatory markers and local neurodegeneration, non-functional electrodes were used to minimize variability between conditions. The functional effects of local neurodegeneration will be important to fully understand the contribution of these findings on recording failure.

Third, in Chapter V, we present results from an in vivo study developing a non-invasive method to monitor scar using electrical impedance spectroscopy. It is undesirable to wait until neurodegeneration occurs to monitor inflammation. While the ideal measurement would be to non-invasively probe pro-inflammatory mediators, i.e. cytokines, at the molecular level, this is very difficult to do non-invasively. An easier target for non-invasive monitoring is astrogliosis, due to the large contribution to the electrical impedance properties of these cells in response to the implant (cell

proliferation and hypertrophy). Therefore, we characterize impedance spectra using bioimpedance modeling methods, and correlate these modeled parameters with cellular density and astrogliosis, as an indirect measure of activated microglia (the primary cellular contributors to inflammation).

Figure 1 shows our hypothesis for how inflammation relates to neurodegeneration and neural recording failure, as well as how extraction force (Chapter III) and electrical impedance (Chapter V) relate to the primary hypothesis.

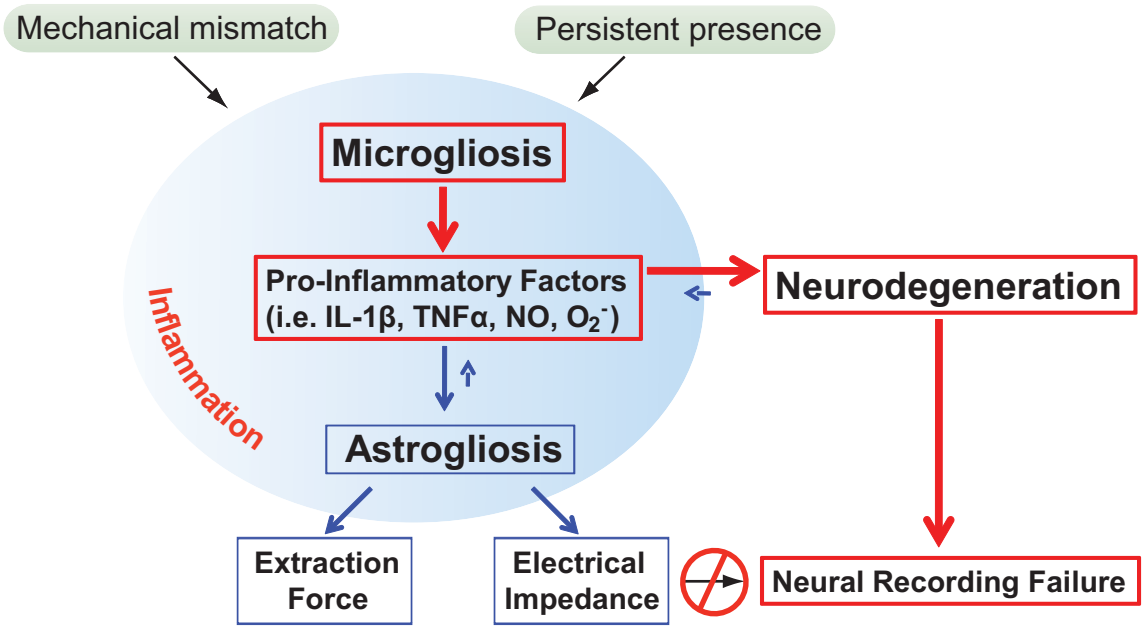

Figure 1: Cartoon showing our hypothesized relationship between inflammation, neurodegeneration, and recording failure. The relationship between electrode extraction force and astrogliosis is discussed in Chapter III, the relationship between inflammation and neurodegeneration is discussed in Chapter IV, and the relationship between electrical impedance and astrogliosis is discussed in Chapter V. While the dominant hypothesis in the field has been that astrogliosis leads to an increase in electrical impedance, which then leads to recording failure, we propose an alternative hypothesis. This cascade is indicated by the red arrows, where microgliosis results in the production of pro-inflammatory mediators, which in turn cause neurodegeneration leading to recording failure.

CHAPTER II

RELEVANT BACKGROUND

2.1 Chronic Neural Recordings have the Potential to Improve the Quality of Life for Paralyzed Persons

A major application of chronic neural recording is neural prosthetics. Electrodes implanted in the primary motor cortex can record motor commands from neurons; the commands are then decoded into electrical signals that bypass injured or damaged nerves to re-animate paralyzed muscles or to control artificial limbs and/or external devices, such as a robotic arm [125]. With chronic neural recording, paralyzed patients and amputees can turn their thoughts into actions, dramatically improving their mobility and interaction with the environment [125]. For example, with electrode arrays implanted in the brain, a paralyzed patient was able to control a cursor to perform computer tasks by thoughts alone [60]. The ability to stably record with implantable electrodes in the CNS will have profound implications for the field of neuroprosthetics. Figure 2 shows an example of a Si-based electrode, the 'Michigan probe', implanted in a rat brain.

2.2 Chronically Implanted Electrodes Trigger a Persistent Glial Scar and Inflammatory State

The initial insertion of the electrodes causes a natural inflammatory response in the brain tissue. However, this initial, acute injury is superseded by a chronic response, which is attested to by studies showing that in stab wounds the electrode tracks could not be located after several months [161, 116, 29], and that inflammation appeared to have subsided after several weeks using silicon microelectrode arrays [7]. In contrast to stab wounds, glial scar surrounding chronic implants persist, suggesting that in

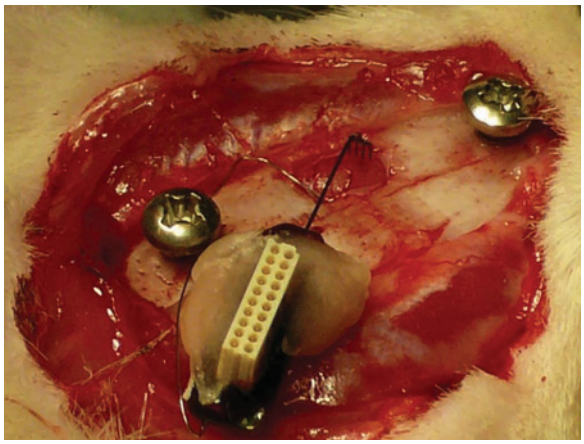

Figure 2: Micrograph of a Michigan electrode implanted in motor cortex.

addition to the initial inflammatory response upon electrode insertion, a foreign body response persists. In chronic inflammation, reactive microglia migrate to the insertion site in an attempt to degrade the foreign body, and activated astrocytes form a tightly interwoven network around the electrodes [142, 139]. This persistent response by microglia has been referred to as "frustrated phagocytosis" and is not unique to microelectrode arrays, but is common to chronic implants in general, and is perhaps analogous to persistent inflammation observed around senile plaques in Alzheimers disease (AD) [148]. The persistent inflammatory response to microelectrodes in non-human primates, shares many similarities with that in rodents. In a study by Griffith and Humphrey, where two rhesus macaques with chronic electrode implants were observed at 3 and 36-month time points [48], there is clear demonstration of a chronic inflammatory response around the electrodes.

The response to implants in the CNS is a complex response involving interplay between at least 4 primary cell types: macrophages (brain and blood-borne), astrocytes, meningeal fibroblasts, and neurons (see Figure 3). Microglia are the resident macrophages of the CNS, and respond to an injury by a change in both phenotype and function, a response commonly referred to as "activation". Pro-inflammatory cytokines released by activated microglia in turn activate astrocytes, which respond

with increased expression of glial fibrillary protein (GFAP) and a change in morphology [41]. Although, the astroglial scar effectively seals off the implant, it is also known to block neurite growth and axonal regeneration both chemically and physically [130]. It has been shown that one class of molecules, chondroitin sulfate proteoglycans (CSPGs), are up-regulated by reactive astrocytes and are one of the main inhibitory molecules in astroglial scar [41].

Astrogliosis is vital for normal tissue repair in the CNS. This has been powerfully demonstrated by a study which investigated the response to spinal cord injury after selective ablation of dividing, reactive astrocytes ([40]). In both stab and crush injuries the absence of reactive astrocytes resulted in inability to repair the blood brain barrier, increased infiltration of leukocytes, along with neurodegeneration and motor deficits. Increased neurodegeneration in hippocampus, which spread to thalamus, of GFAP-KO mice has also been reported ([104]). These results indicate that astrogliosis is an essential mechanism in restricting inflammation and preserving neuronal health (and function) after injury.

In this thesis, inflammation is used to refer to the response of both microglia and astrocytes to the electrode (see Figure 1). However, it is microglia that have been shown to be the primary source for pro-inflammatory factors, such as pro-inflammatory cytokines and reactive oxygen species, after CNS injury ([11, 12]).

2.3 Strategies to Improve Chronic Recording Stability

Given the inconsistency observed in the literature, along with the strict demands on long-term performance for clinical efficacy which neural interfaces must meet, several strategies have been adopted to improve the stability of chronically implanted MEAs [110]. Szarowski et al. studied the effect of electrode shape, size, texture and tip geometry and observed no difference in astroglial scar between any conditions

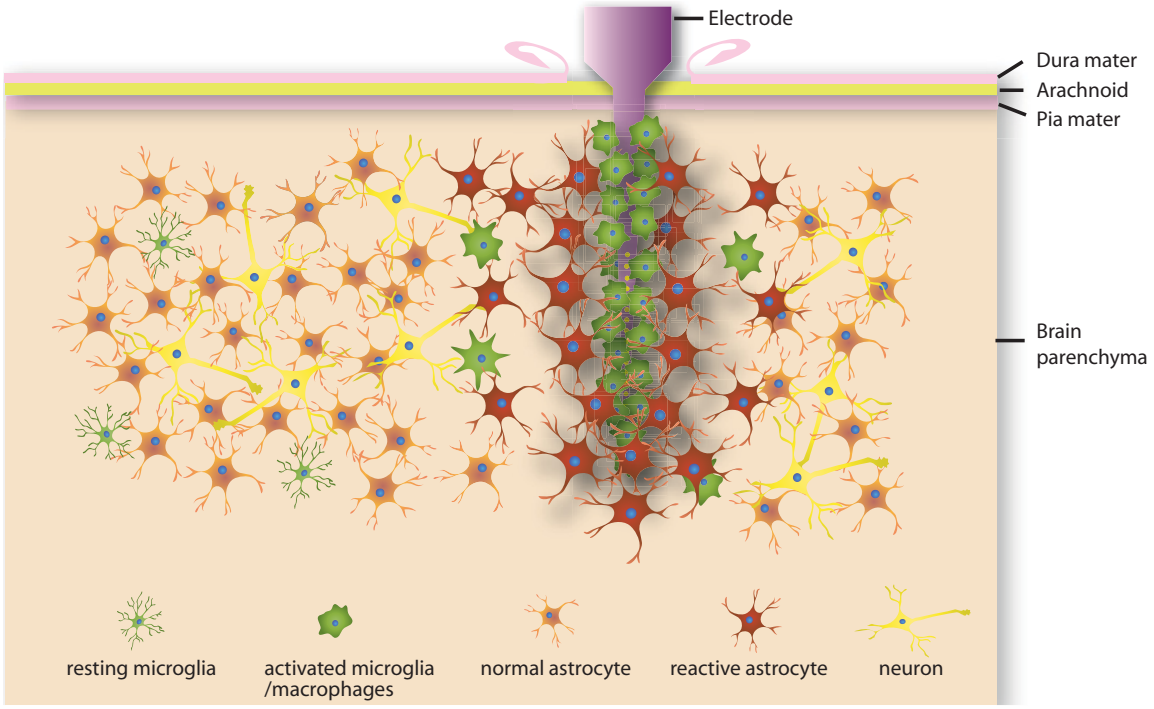

Figure 3: Cartoon showing the primary cell types involved in the tissue response to implanted microelectrodes. Phenotypic changes in microglia occur in response to the implant, from an on guard, "resting" state to a so-called "activated" state characterized by ameboid shape and release of pro-inflammatory factors. Astrocyte phenotypic changes also occur characterized by hypertrophy and an increase in GFAP expression (shown by darker red color). Reproduced, with permission, from [53].

tried after 6 and 12 weeks post-implant [139]. This study suggests that more than mechanical methods must be tried in order to minimize astrogliosis. Two recent studies have reported an attenuated astroglial scar through systemic doses via subcutaneous injections of dexamethasone [128, 132]. However, systemic drug administration induces undesirable side-effects, along with a large quantity of drug needed for efficacy. One strategy for improving the interface is to lower the electrode impedance. The Martin lab has published several reports on electroplating using conducting polymers including polypyrrole [30, 31] and PEDOT [158, 159, 157, 156]. Another strategy is the use of bioactive coatings to modulate cell interactions; examples which have been developed include a dextran monolayer [92] and alginate gel [67]. Another approach which is being developed is local release of anti-inflammatory drug controlled by electrical stimulation [145, 1]. None of these strategies effects on neural recordings have yet been published.

Our lab has demonstrated the feasibility of coatings for Si microelectrode arrays with several approaches tried including the local slow release of the anti-inflammatory drug dexamethasone [166] (a similar approach used by [66]) and neuropeptide α-MSH [165] and layer-by-layer assembly of laminin designed to improve cell attachment [52, 54]. Each of these coatings has been shown to mitigate astroglial scar in vivo, however, the effect of the coatings on chronic recording stability have not been studied.

2.4 The Relationship Between Inflammation and Neurodegenerative Disease

A growing number of studies support the hypothesis that neuroinflammation plays a pivotal role in the etiology of many neurodegenerative diseases, including AD, Parkinsons disease (PD), and Amyotrophic Lateral Sclerosis (ALS) [47, 164, 11]. Although there are a range of factors that can initiate neuronal damage in neurodegenerative diseases, there is substantial evidence that activation of neuroinflammatory cells

exacerbates neurodegeneration [153]. One piece of evidence includes the observation of elevated levels of IL-1 (Interleukin-1) and TNF-α (Tumor Necrosis Factor), pro-inflammatory cytokines released by activated microglia, in patients with neurodegenerative disease [42]. To further support the hypothesis, numerous studies have shown that people with early-life brain injuries are more likely to develop PD, implying that inflammation in the brain plays a crucial role in the pathogenesis of neurodegenerative disorder [82]. The final piece of evidence for the involvement of inflammation in the neurodegenerative disease is derived from its regiospecificity. It is well known that the primary cause of PD is degeneration of neurons in the central nervous system, specifically in the substantia nigra. According to studies, substantia nigra is heavily populated with microglia, and therefore, more vulnerable to the inflammation caused by activated microglia, providing further proof of a mechanistic link between inflammation and neurodegenerative disorders [68, 111]. We further hypothesize that similarities in many features of neurodegenerative diseases exist between diffuse neurodegenerative diseased tissue and the local tissue surrounding chronic microelectrodes.

2.5 Markers of Inflammation: Microglia are Mediators of Inflammation via Cytokine Production

Inflammation, a specialized immune response of the organism, is crucial and necessary if the invading agent is a pathogen or a dying cell [155]. However, an aggressive activation of immune cells can lead to scarring and damage of the tissue, often destroying host cells in its wake [155]. Unlike normal cells, neurons in the brain tissue lack the ability to divide and to recover, becoming more susceptible to auto-destructive immune and inflammatory process [45]. This inflammatory process is mainly caused by the activation of microglia, the resident immune cells in the brain [45]. Microglia are sensitive to alteration in their surroundings, activating in response to even the

slightest infection or injury [82, 11]. Additionally, activated microglia produce pro-inflammatory and neurotoxic cytokines such as IL-1, TGF-β, TNF-α, and IL-6, resulting in inflammation and degeneration of neurons ([45, 11, 98]. We hypothesize that microglia in a sustained active state at the electrode interface generate the molecular stimuli for a local neurodegenerative state.

2.6 Markers of Inflammation: NADPH induced Oxidative Stress Exacerbates Inflammation-Induced Neurodegeneration

Reactive oxygen species (ROS) act both directly and indirectly to promote neurodegeneration. Extracellular ROS is neurotoxic directly, while intracellular ROS amplifies pro-inflammatory cytokine production in microglia. Recent studies demonstrated that ROS production is attributable to activation of microglial nicotinamide adenine dinucleotide phosphate (NADPH) oxidase [106, 154]. Evidence for oxidative stress in Alzheimers diseased brains has suggested a mechanistic link with neurodegeneration [163]. Additionally, microglia-derived oxidative stress has also been suggested to mediate dopaminergic toxicity in PD, with NADPH oxidase playing a key role [45]. Dopaminergic neurons in the substantia nigra are more susceptible to microglia-mediated neurotoxicity than other cell types [85]. Therefore, evidence of reactive oxygen species is consistent with a) an inflammatory condition and b) neurodegeneration.

2.7 Molecular Markers of Neurodegeneration: Tau Protein Hyperphosphorylation is Neurotoxic and is a Hallmark of Neurodegenerative Diseases

Tau proteins, microtubule-associated proteins, are primarily located in neurons where they function to maintain cell shape and act as tracks for axonal transport [15]. Pathological hyperphosphorylation and ensuing aggregation is a feature of many neurodegenerative diseases, called "tauopathies", including AD [2]. Tau is vital to normal

axonal transport, and hyperphosphorylation of tau has been shown to "clog" synapses, prior to their aggregation into tangles, leading to abnormal synaptic function and enhanced oxidative stress [90] as well as functional synaptic loss [120, 36]. While the cause of tau tangles is still unknown, recent work has suggested that neuroinflammation, particularly microglial activation, may play a critical role in the progression of tauopathies. Synaptic pathology and microglial activation occur prior to the formation of tau tangles in a P301S tauopathy mouse model [160]. When the mice were immunosuppressed by F506, tau progression was significantly reduced, suggesting an interaction between activated microglia and tau pathology. Additionally, Melov et al. have reported that tau hyperphosphorylation is induced by oxidative stress and can be prevented by antioxidants [95]. Tau hyperphosphorylation is therefore a feature of neurodegenerative disease which is consistent with both persistent microglial activation and oxidative stress, features present at the chronic electrode interface.

2.8 Summary

The feasibility of thought-controlled prosthetic devices has within the last decade been powerfully demonstrated [149, 126, 141, 16, 76, 60]. However, for these important scientific and technological breakthroughs to affect a wider population and influence their quality of life, an important emphasis must be placed on gaining a better understanding of the factors that influence their success or failure, especially those that impact the reliability of chronically implanted intracortical microelectrodes.

A careful review of the literature suggests that a) it is unlikely that changes in electrical impedance due to glial scar are the primary cause of chronic recording failure of intracortical electrodes; b) implanted electrodes cause a persistent and chronic inflammation; c) chronic inflammation is strongly linked to neurodegenerative states; d) chronic inflammation is marked by local expression of pro-inflammatory cytokines,

NADPH-mediated reactive oxygen species and nitric oxide (NO); and e) neurodegeneration is likely to significantly influence long-term recordings.

While the influence of persistent inflammation in neurodegenerative diseases is a heavily researched topic, the relationship of persistent inflammation on the health of target neurons surrounding chronically implanted microelectrodes has not been explored.

CHAPTER III

CHRONIC INFLAMMATION SURROUNDING INTRA-CORTICAL MICROELECTRODE ARRAYS CAN BE MODULATED BY ELECTRODE SHANK SPACING

3.1 Abstract

Micromotion of implanted silicon multielectrode arrays (Si MEAs) is thought to influence the inflammatory response they elicit. The degree of strain that micromotion imparts on surrounding tissue is related to the extent of mechanical integration of the implanted electrodes with the brain. In this study, we quantified the force of extraction of implanted four shank Michigan electrodes in adult rat brains and investigated potential cellular and extracellular matrix contributors to tissue-electrode adhesion using immunohistochemical markers for microglia, astrocytes and extracellular matrix deposition in the immediate vicinity of the electrodes. Our results suggest that the peak extraction force of the implanted electrodes increases significantly from the day of implantation (day 0) to the day of extraction (day 7 and day 28 post-implantation) (1.68 ± 0.54 g, 3.99 ± 1.31 g, and 4.86 ± 1.49 g, respectively; mean SD;$n = 4$). For an additional group of four shank electrode implants with a closer intershank spacing we observed a significant increase in peak extraction force on day 28 post-implantation compared to day 0 and day 7 post-implantation (5.56 ± 0.76 g, 0.37 ± 0.12 g and 1.87 ± 0.88 g, respectively;$n = 4$). Significantly, only glial fibrillary acidic protein (GFAP) expression was correlated with peak extraction force in both electrode designs of all

the markers of astroglial scar studied. For studies that try to model micromotion-induced strain, our data implies that adhesion between tissue and electrode increases after implantation and sheds light on the nature of implanted electrode-elicited brain tissue reaction.

3.2 Introduction

Neural electrode technology holds the exciting potential of allowing direct communication between nervous tissue and external electronics. This burgeoning technology has already significantly enhanced the quality of life for many patients with sensory and/or motor deficits as is evident from both the prosthetic cochlear implant, commonly used for treatment of deafness [4, 112] and deep brain stimulation, which has been used to reduce motor symptoms associated with Parkinson's Disease [140, 83, 108]. Silicon multielectrode arrays (Si MEAs) have been a driving force in the advancement of neural interface technology with several advantages over competitive devices including high density recording sites, batch fabrication, highly reproducible geometry, and user-customizable dimensions [58]. These micromachined neural prosthetic devices have been used to stimulate and record from the central and peripheral nervous systems [118, 13, 70, 143, 60].

However, the long-term functionality of MEAs, especially in the recording mode, is compromised by the formation of scar tissue surrounding the devices [117, 152, 84, 100, 119]. This is presumably due to implant induced astrogliosis, a process which electrically and mechanically isolates the prosthesis from the nervous system [142, 139] and causes neuronal cell loss in close proximity of the electrode surface [7, 37].

Tissue response to implants is commonly described in terms of an acute response caused by the trauma of implantation and a chronic response [142, 139]. The acute response is due to the rapid adsorption (within a millisecond) of a layer of proteins on the material upon contact with blood. This protein layer promotes attachment

of platelets, neutrophils and macrophages which stimulate astrogliosis and ultimately lead to fibrous encapsulation. The chronic response is persistent due to the continued presence of the electrode: astrogliosis due to a stab wound injury is nearly absent after four weeks post-injury [7].

The response to implants in the CNS is a complex process involving interplay between at least four primary cell types: microglia/macrophages, astrocytes, meningeal fibroblasts, and neurons. Microglia are the resident macrophages of the CNS, and respond to an injury by a change in both phenotype and function, a response commonly referred to as "activation". Pro-inflammatory cytokines released by activated microglia in turn activate astrocytes, which respond with increased expression of the intermediate filament proteins vimentin and glial fibrillary acidic protein (GFAP), along with a change in morphology [41]. The astroglial scar effectively seals off the implant, blocks neurite growth and/or axonal regeneration, and presumably excludes neural cells by its presence immediately next to the electrode surface [130].

It has been suggested that micromotion, caused by the mechanical mismatch between Si and brain tissue, is a major factor in the chronic tissue reaction to these devices [110]. Recently, finite element modeling has been used to map the strain fields in brain tissue adjacent to Si MEAs [77, 133]. These studies concluded that the degree of electrode-tissue integration strongly influences both the distribution and magnitude of interfacial strain levels. In the bonded condition, in which tissue tightly adheres to the Si MEA, peak strain levels were lower by several orders of magnitude compared to the slip condition, in which tissue poorly adheres to the Si MEA. One study predicted regions of compression and delamination at the Si MEA tip in the case of poor adhesion between the electrode and brain tissue [133]. However, experimental data on the degree of mechanical integration of brain tissue with chronically implanted Si MEAs does not exist to inform modeling studies.

Previous studies have reported an increase in the attachment of muscle tissue

to intramuscular electrodes after 7d using extraction force measurements [5, 6]. We hypothesized that with increasing implantation time, brain tissue surrounding a Si MEA would similarly anchor the MEA, even in the absence of integrative coatings. In this study, we test this hypothesis by quantifying the force along the longitudinal axis while extracting chronically implanted Si MEAs from brain tissue <5h (0d) post-implant (p.i.), 7d p.i., and 28d p.i. Care was taken to ensure that the measured force was from electrode-cortical tissue integration, and not from dural reestablishment around the electrode. Dura regrowth was not observed in close proximity to the bondpad for all of the implanted electrodes at the time of extraction. Peak extraction forces were then tested for correlations with state-of-the-art markers of astroglial scar at the corresponding times to investigate a potential mechanism by which the electrodes were anchored (if at all).

3.3 Materials and Methods

3.3.1 Surgical Procedures for Chronic Implants

"Michigan probes" with four shanks were used in this study (NeuroNexus Technologies). A total of six rats, two rats per time point, were implanted with electrodes with thickness of 15μm, length of 4mm, shank width of 60-100μm, and tip spacing of 200μm (abbreviated 4mm_200). Two electrodes were implanted in each animal at different hemipheres for a total of 12 microelectrodes used. To determine the effect of inter-shank distance on astrogliosis and peak extraction force an additional six rats, two rats per time point, were implanted with electrodes with thickness of 15μm, length of 3mm, shank width of 30-100μm, and tip spacing of 125μm (abbreviated 3mm_125). Figure 4 shows the layout of the two probe designs.

Adult male Sprague-Dawley rats (275-299grams) were anesthetized for 5min with a mixture of 5% isoflurane and 1L/min O2 prior to surgery. Each rat was positioned

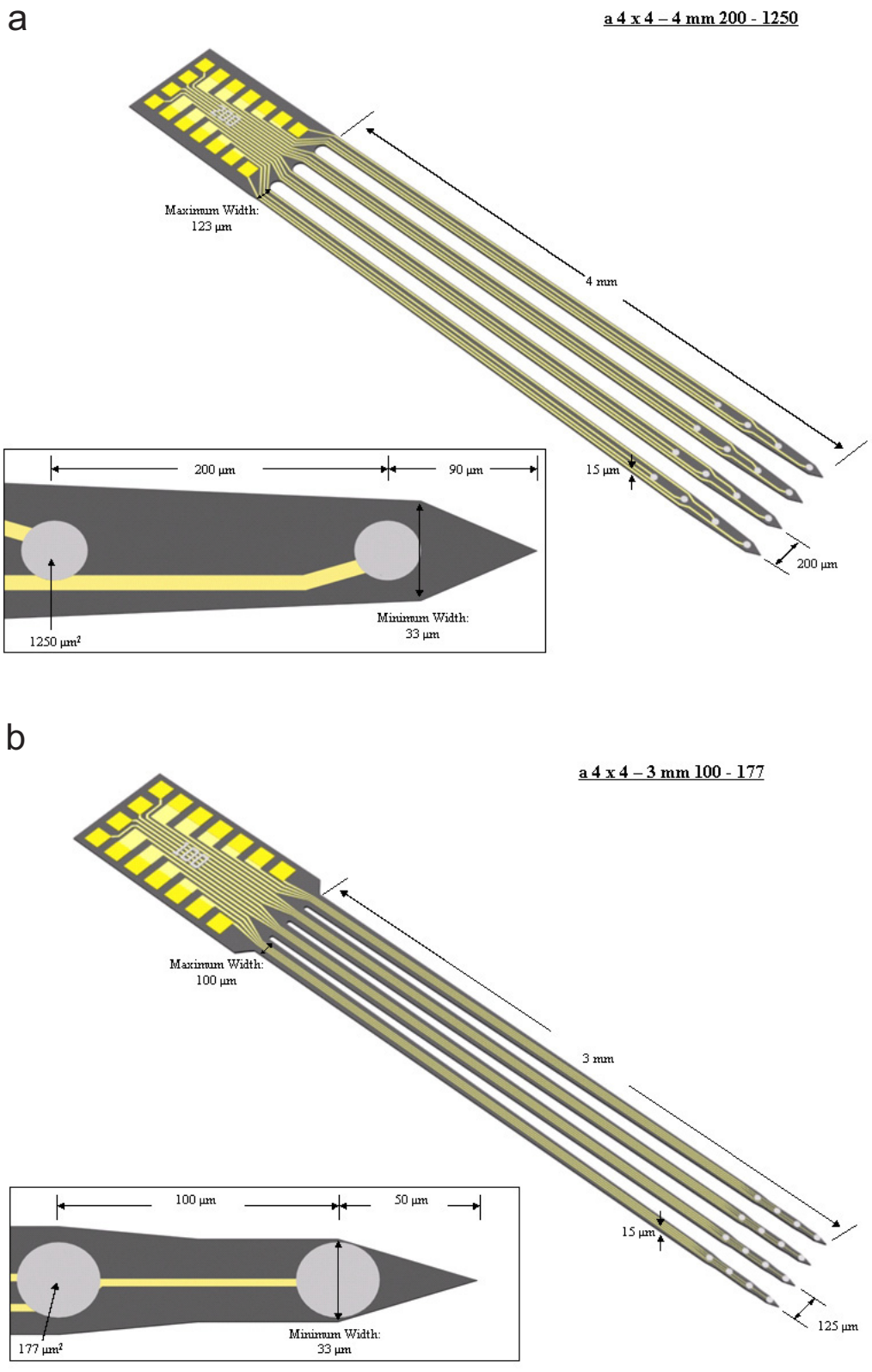

Figure 4: Dimensions of electrodes used in in vivo studies of Chapter III and Chapter IV. Probe design (b) elicited greater chronic inflammation compared with probe design (a). Schematics were obtained from NeuroNexus Technologies (`http://www.neuronexustech.com/`).

into a stereotactic frame (Kopf) where anaesthesia was maintained to effect (∼1-3% isoflurane and 0.3L/min O2) during surgery by monitoring the rat's breathing. The rat's head was shaven over the incision area and the skin was disinfected with isopropyl alcohol and chlorohexaderm using a slight scrubbing motion before making the incision. Ophthalmic ointment was applied to the eyes to prevent drying. A midline incision was made along the scalp, the skin retracted, and the periosteum cleared to expose the bregma. A dental drill was used to create a 3.2mm hole at +0.2mm anterior and +3.0mm lateral to the bregma with a custom trephine (24 tooth x 3mm O.D.) fabricated from stainless steel tubing (Small Parts). In order to minimize iatrogenic damage, room temperature saline was applied liberally to the spinning drill bit at the bone interface. The bone plug was carefully removed and the dura was gently pierced and retracted using a 28 gauge needle with the tip bent at a 45˚angle. The bond-pad region of the microelectrode was grasped with Teflon-coated microforceps and the penetrating shanks were inserted by hand through the pia mater into the cortex. Care was taken to minimize bleeding by avoiding insertion through large surface blood vessels. The electrode was inserted to the point where only the bond-pad region was visible outside of the cortical surface. After the insertion, the bond-pad region of the electrode and the craniotomy was covered with 1% SeaKem Agarose (Cambrex) gel in phosphate buffered saline (PBS). A craniotomy of identical diameter was made over the contralateral location (+0.2mm anterior to the Bregma and -3.0mm lateral to the midline suture) where an additional electrode was inserted and protected with agarose the same way as described above. The craniotomies were further sealed and protected using dental acrylic anchored to the skull with bone screws (Plastics One, Inc.). The skin was closed with wound clips and the rats were monitored until recovery from anesthesia. To minimize variability associated with the surgery, all implants were performed by the same surgeon. All procedures were approved by Georgia Tech Institutional Animal Care and Use Committee.

3.3.2 Measurement of Extraction Force

A ±30g force sensor with an accuracy of 0.015g (GSO Series Load Cell, TransducerTechniques) was mounted to a micromanipulator (Pi MP-235.5DG), which was stationed on an anti-vibration table. The micromanipulator was controlled via serial port from a computer. The output of the force sensor was low-pass filtered with a cut-off set at 150Hz (6dB/octave) and amplified with a gain of 2000 (Model TMO-2 Amplifier, Transducer Techniques). A 14-bit analog to digital I/O interface (USB 6009, National Instruments) was used to record the amplifier/conditioner signal output to a computer with a sampling rate of 1000Hz. The force sensor load point was attached with a smooth banana clip; the clip was protected using Teflon tape to avoid breaking the electrode. A schematic of the setup used to measure force while extracting the electrodes is given in Figure 5a.

Rats were prepared for force extraction and subsequent immunohistochemistry <5h (0d), 7d, and 28d after device insertion. The longest time point of 28d was chosen because previous data suggests that a compact glial sheath is fully organized by this time [139]. Each rat was anesthetized with ketamine (45.65mg/kg), xylazine (9.13mg/kg), and acepromazine (1.52mg/kg). Rats were then perfused intracardially with PBS prewash followed by 4% paraformaldehyde in PBS. The brains were removed by carefully cutting along the sides and anterior to the craniotomy sites and lifting off the top of the skull. Because the dura had not regrown around the implanted electrodes, when the top of the skull was lifted the electrode was not touched and remained in the brain. The brains, with electrodes in place, were postfixed for a maximum of 24h (4 ℃) in 4% paraformaldhyde in PBS followed by 2h in PBS (4 ℃). One brain at a time was then removed from the PBS and the bottom surface was dried and fixed to an aluminum plate using cyanoacrylate (LocTite). The glue was applied to the plate surface and the brain was held onto the aluminum surface for ∼30s while the glue dried. The plate was then positioned under the micromanipulator-mounted

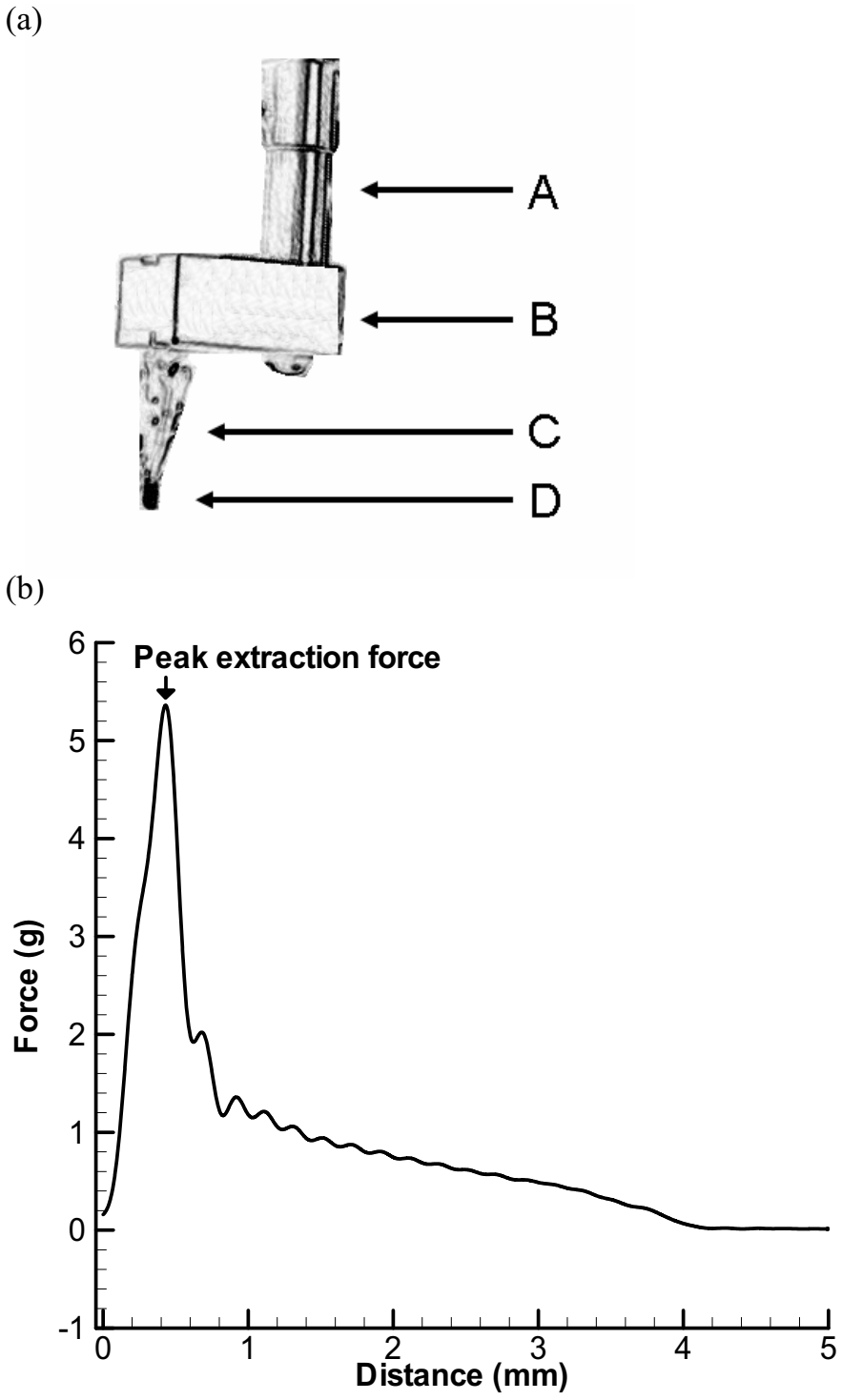

Figure 5: (a) Schematic of the setup used to measure force while simultaneously extracting implanted probes. A computer-controlled micromanipulator (A) is mounted to a 30g force sensor (B). A banana clip (C), coated with Teflon at the tip (D), established a connection with the exposed bond pad of the implanted electrode immediately prior to extraction of the electrode. (b) Force extraction data obtained from an electrode extracted 28d p.i.

force sensor.

Under visual magnification, the micromanipulator was lowered to the level of the bondpad and the clip was held open while the plate was adjusted such that the bondpad was between the teeth of the clip. The clip was then carefully closed, connecting the electrode to the force sensor. LabVIEW (National Instruments) was used to visualize and record the data collected from the force sensor. Once acquisition was started from the force sensor, the micromanipulator was raised at a constant velocity of 1mm/s. When it was observed that the electrode was completely removed from the brain, the micromanipulator and digital data acquisition was stopped.

3.3.3 Analysis of Extraction Force

Post processing of the force measurement data consisted of low-pass filtering, baseline subtraction and identification of the maximum force using custom routines written in MATLAB. Data sets were first truncated to contain only the first 30s of data. Including longer data sets caused errors due to inaccurate baseline calculations and/or detecting false peaks. Data were digitally filtered using a linear phase, low-pass filter (FIR1 function in MATLAB) with cutoff at 5Hz to remove high frequency noise while the micromanipulator was moving. Data were then baseline subtracted by subtracting the mean force during the last 100ms of the data set from the entire data set. The maximum force within each data set was identified, which we refer to as the peak extraction force. An example force-displacement recording is shown in Figure 5b following digital filtering and baseline subtraction. The peak extraction force, in this case, was identified as 5.32g.

3.3.4 Brain Tissue Preparation for Immunohistochemistry

Following the retrieval of the electrodes, rat brains were placed into 30% sucrose (4 ℃) until they sunk to the bottom. A tissue dye was then carefully applied to the left-posterior hemisphere to later identify the orientation of the brain sections and align

images with the same electrode orientation. The brains were then cryoprotected with Optimal Cutting Temperature (O.C.T.) compound (Tissue-Tek). Horizontal tissue sections were cut to a final depth of ∼2mm from the surface of the cortex for all brains. Serial sections were cut 30μm in thickness with the exception of every 13th section, which was cut 14μm in thickness. The 14μm sections were mounted directly to glass slide and stained with Hematoxylin and Eosin (H&E) using a Leica Autostainer XL, while the 30μm sections were serially stored in two six-well plates at 4 ℃in PBS with 0.01% sodium azide to minimize bacterial contamination. H&E was used to visualize general tissue morphology, while immunohistochemistry was used to visualize specific cellular and extracellular matrix (ECM) markers.

3.3.5 Immunohistochemistry of Brain Sections

To study brain tissue response, sections taken from all brains were stained simultaneously for the antibody of interest. Sections from adjacent wells, with six sections per well, were used to double-stain GFAP/vimentin, Collagen Type I (Coll I)/ED-1, and Laminin (LN)/Reca-1 respectively. These stains were used to visualize the presence of astrocytes (GFAP$^+$, GFAP$^+$/vimentin$^+$), microglia (ED-1$^+$, vimentin$^+$), blood vessels (Reca-1$^+$, LN$^+$, vimentin$^+$), fibroblasts (Coll I$^+$, GFAP$^-$/vimentin$^+$), and ECM deposition of LN. The six sections per well ranged from ∼200μm to ∼2mm below the surface of the cortex and were spaced at uniform intervals of 374μm. Sections were blocked in 4% normal goat serum (GIBCO) with PBS containing 0.5% Triton X-100 (Sigma) for 1h at room temperature. Sections were then immediately incubated overnight at 4 ℃with primary antibody prepared in blocking solution. Primary antibodies used are shown in Table 1. After washing in 0.5% triton in PBS, sections were incubated in secondary antibodies for 1h at room temperature. Secondary antibodies were diluted at a ratio of 1:220 in 0.5% triton in PBS, and included goat anti-rabbit IgG (H + L) Alexa 594 (Molecular Probes) and goat anti-mouse IgG1

Table 1: Primary antibodies used in this study

Primary	Host	Dilution	Isotype	Vendor	Specificity
GFAP	rb	1:2000	IgG	Dako	astrocytes
Vimentin	ms	1:500	IgG1	Sigma	immature & reactive astrocytes, microglia, endothelial cells and fibroblasts
Coll I	rb	1:250	IgG	Chemicon	ECM marker
CD68 (ED-1)	ms	1:1000	IgG1	Serotec	activated microglia/macrophages
LN	rb	1:500	IgG	Sigma	ECM marker
Reca-1	ms	1:500	IgG1	Serotec	endothelial cells

Alexa 488 (Molecular Probes). All sections were counterstained by incubation with the nuclear dye DAPI (Molecular Probes) that labels all cell nuclei. An additional cortical section from each rat brain was used to control for non-specific secondary antibody labeling, by omitting the primary incubation step (primary control). Tissue sections were mounted on glass microscope slides with Fluoromount-G (Southern Biotechnology Associates).

3.3.6 Quantitative Analysis of Coll I/ED-1 and GFAP/vimentin Expression

Fluorescent and brightfield images were acquired using a Microfire digital camera and a Zeiss Axioskop2 Plus upright microscope with a 10X objective, with the electrode sites centered in the camera field. Three sections approximately 200μm, 600μm and 1mm below the brain surface were imaged for quantification due to similarities in the cortical tissue response of this region. All tissue sections were imaged in a single session to minimize variability. The exposure time was consistent within each marker and was set below saturation of the digital camera.

Fluorescent intensity as a function of distance from the electrode-tissue interface was calculated for GFAP/vimentin and Coll I/ED-1 stained sections using MATLAB (with Image Processing Toolbox, Mathworks). Briefly, images were first rotated such

that the four insertion sites were aligned vertically. An ellipse was computed from five or more user-specified points around each of the four insertion sites using the brightfield image to easily delineate the electrode-tissue interface and the location of the ellipses were then saved to file. Saved ellipse points were then used in the corresponding immunostained images (either GFAP/vimentin or Coll I/ED-1) to segment rectangular regions from the middle of each ellipse to a distance of 500μm away for both the left and right sides. The intensity values of each of the boxed regions were then averaged along the y-axis to create two mean intensity profiles for each insertion site. The mean of the eight line profiles was then computed. To correct for background differences due to non-specific secondary antibody binding (particularly in the immediate vicinity of the insertion sites), mean profiles of identical length from primary control sections were subtracted within each group. The integral of the mean intensity profile at three different distances along the electrode (0-100μm, 100-300μm, and 300-500μm for GFAP/vimentin and 0-25μm, 25-50μm, and 50-100μm for Coll I/ED-1) was also calculated for each image. Figure 6 shows an example image with corresponding fluorescent intensity line profile.

In addition to the quantification of ED-1 intensity as a function of distance from the electrode site, ED-1 images were also quantified by estimating the number of microglia. DAPI images, which stain all cell nuclei, were used to aid in validating the presence of microglia. Images were processed with the end goal being to count only colocalized, segmented regions of ED-1 and DAPI signal indicative of microglia. ED-1 staining of microglia is highly irregular and therefore difficult to quantify by segmentation. DAPI staining of cell nuclei is more regular and thus simple, by comparison, and was segmented using a marker-based watershed algorithm. For the ED-1 images, primary controls from every condition were analyzed to estimate the common background signal. The background intensity was then subtracted from all of the ED-1 positive images. Most sections incubated with Alexa 488 secondary antibody

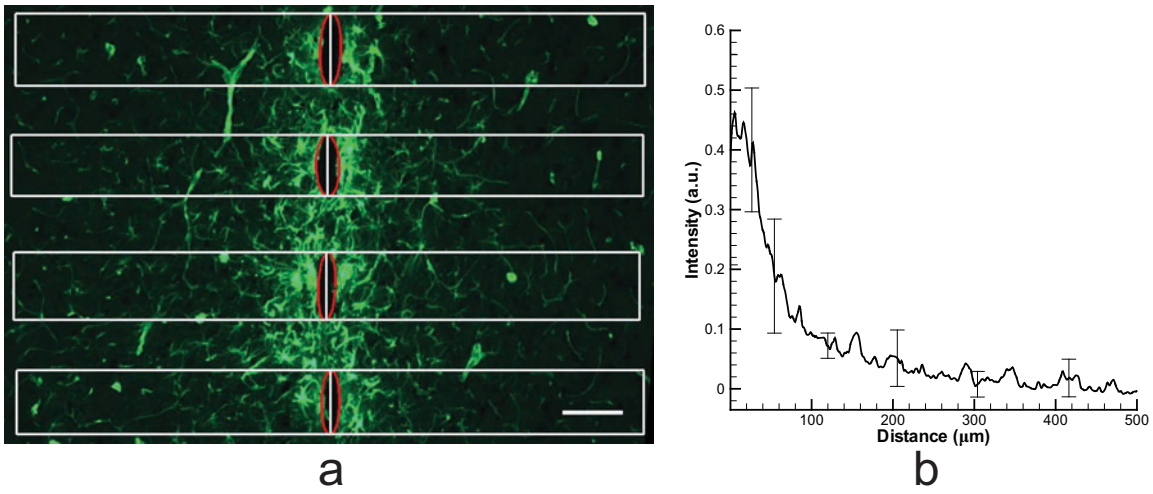

Figure 6: Quantification of fluorescent intensity as a function of distance from the interface. (a) Example Vimentin-stained image after delineating probe sites (red ellipses) and regions of interest (white rectangles). White boxes outline the region up to 500 μm away from interface. (b) Mean $\pm$ SD fluorescent intensity of eight white boxed regions in (a).

suffered from non-specific binding at tissue edges. In order to remove the background illumination in the immediate vicinity of the insertion site, top-hat transformation was performed. Top-hat transformation is a process which involves an estimation of background illumination followed by its subtraction from the original. The ED-1 image was then converted to a labeled image. The image of a single ED-1 label was compared with the entire segmented DAPI image. Groups of pixels with area above a pre-determined size, common in both DAPI and ED-1 images were counted as ED-1^+ cells.

3.3.7 Statistical Analysis

All statistical inferences were made between differing time points using one-way standard analysis of variance. When we found a significant difference between groups, we performed the Tukey's Honest Significant Difference (HSD) post-hoc test to identify pairwise differences. Correlations were tested using Pearson's correlation coefficient and the significance was tested using Student's t-test. For all tests, $p < 0.05$ was

considered significant.

3.4 Results

3.4.1 Extraction Force

We defined the peak extraction force as the maximum force within each data set acquired during electrode extraction. In both probe designs, peak extraction force increased from the day of implantation (0d p.i.) to the longest time point studied of 28d p.i. (Figure 7). For the 4mm_200 implants, baseline corrected raw peak extraction forces for 0d, 7d, and 28d p.i. were 1.68 ± 0.54g, 3.99 ± 1.31g, and 4.86 ± 1.49g (mean ± SD). The peak extraction force for both 7d p.i. and 28d p.i. was significantly higher than for 0d p.i. ($p < 0.05$). No significant difference was observed between 7d p.i. and 28d p.i. forces ($p = 0.57$).

For the 3mm_125 implants, the baseline corrected raw peak extraction forces for 0d, 7d, and 28d p.i. were 0.37 ± 0.12g, 1.87 ± 0.88g, and 5.56 ± 0.76g (mean ± SD). The peak extraction force for 28d p.i. was significantly higher than for both 0d p.i. and 7d p.i. ($p < 0.05$). A striking difference between the two designs was this significant increase in peak extraction force 28d p.i. No significant difference was observed between 0d p.i. and 7d p.i. forces ($p = 0.058$).

3.4.2 Investigating the Presence of Meningeal Fibroblasts

Coll I is a component of the ECM important in structural support. In normal healthy brain tissue Coll I is absent, but is ubiquitous in the meninges. Coll I is therefore a useful marker for visualizing the presence of meningeal-derived fibroblasts in brain tissue. A thin layer, approximately 20μm in thickness, of intense Coll I signal was observed in 7d and 28d sections immediately adjacent to the insertion sites (Figure 8k,l). Coll I signal was absent in 0d sections (Figure 8j).

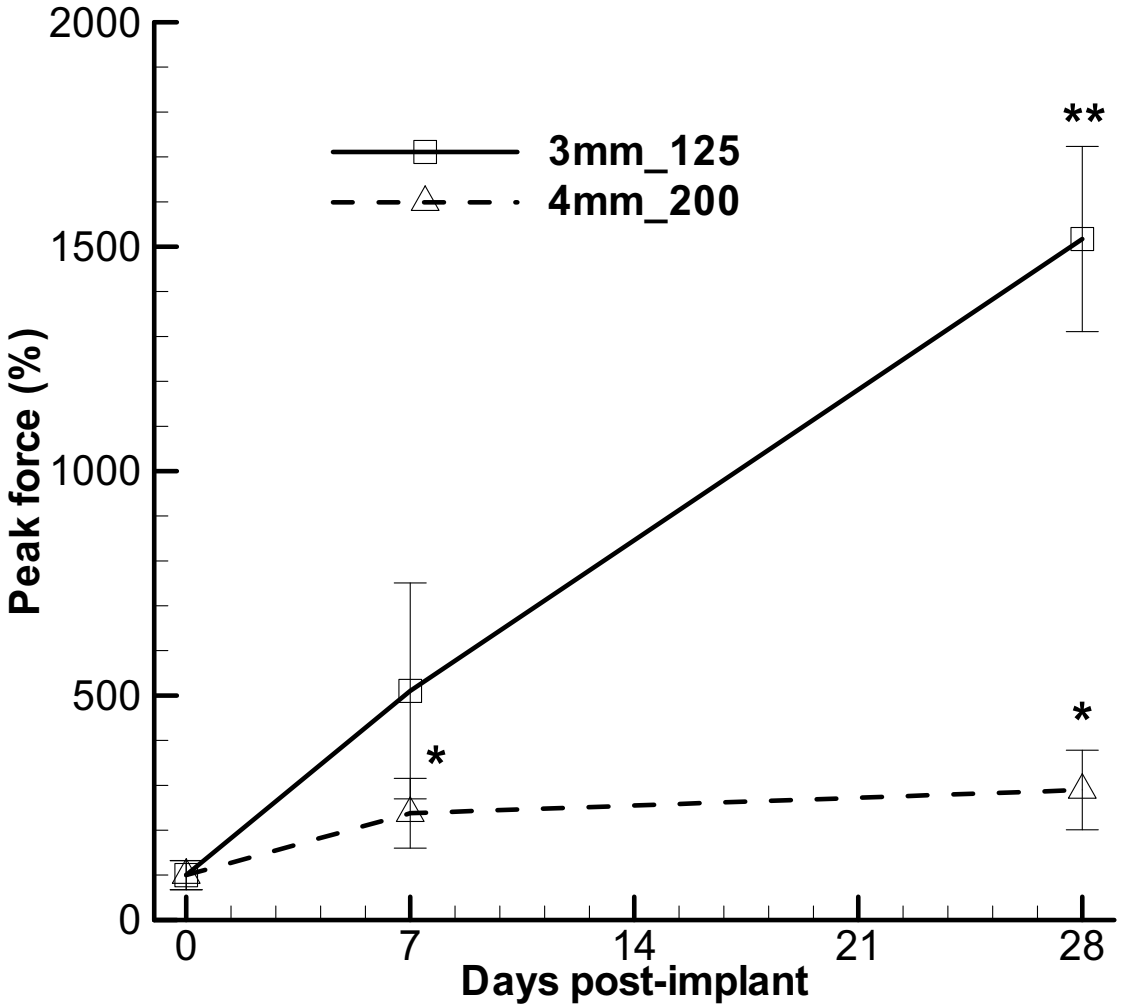

Figure 7: The maximum force was determined from each acquired force data set (one data set from each extracted probe; n = 4). Peak force is shown normalized to the 0d condition for two different probe designs used in this study. ** indicates a significant difference relative to both the 0d and 7d conditions ($p < 0.05$). * indicates a significant difference relative to the 0d condition ($p < 0.05$).

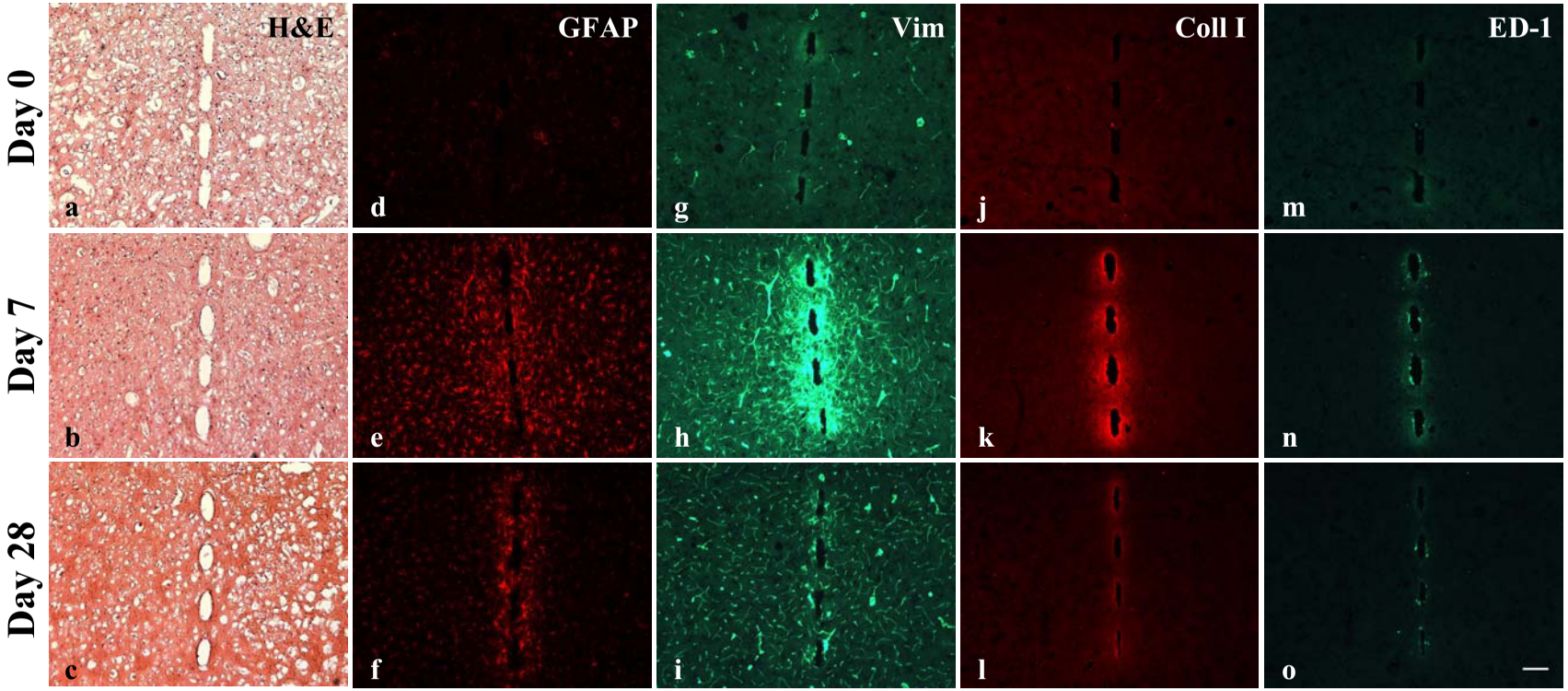

Figure 8: (a)-(o) Representative stained sections for each of the time points studied for H&E (a-c), GFAP (d-f), vimentin (Vim) (g-i), Collagen Type I (Coll I) (j-l), and ED-1 (m-o). Sections shown are from similar depth in the cortex ($\sim$600μm below the brain surface). Sections were double-stained with GFAP & Vimentin or Coll I & ED-1. Regions were imaged using a 10X objective with the probe sites centered. Immunostained images were subsequently quantified. As implant duration increased, the astroglial scar became more compact (a-f). Vimentin, Coll I and ED-1 expression were greatest surrounding the probe sites after 7d p.i. compared to 0d and 28d p.i. (g-o). Scale bar=100μm.

3.4.3 Investigating the Presence of Microglia

ED-1 is a marker specific for reactive microglia/macrophages. Immediately following implantation, no ED-1 signal was present surrounding the insertion sites (Figure 8m). After 7d ED-1 signal was present in the immediate vicinity of the insertion sites (Figure 8n). By 28d p.i., a decreased number of ED-1$^+$ cells were observed in comparison to 7d (Figure 8o). Both 7d and 28d p.i., ED-1$^+$ signal was primarily observed within 50μm of the insertion sites.

3.4.4 Quantifying Coll I/ED-1 Expression

The intensity of Coll I and ED-1 stained sections was quantified as a function of distance from the insertion sites. Figure 9a shows the distribution of Coll I surrounding the insertion site. The area under the intensity curve from 0-25μm, 25-50μm, and 50-100μm away from the interface are plotted as mean $\pm$ SD (Figure 9c). Comparatively, Coll I signal 7d p.i. was significantly higher than 0d and 28d p.i. within 0-25μm and 25-50μm ($p < 0.05$).

Figure 9b shows the distribution of ED-1 surrounding the insertion site. The area under the intensity curve from 0-25μm, 25-50μm, and 50-100μm away from the interface are plotted as mean $\pm$ SD (Figure 9d). ED-1 expression 7d p.i. was significantly higher than 0d and 28d p.i. within 0-25μm and 25-50μm ($p < 0.05$). While mean intensity profiles give an indication of ED-1 signal distribution from the insertion sites, along with the general trend over time, cell counting is a common method for quantification of ED-1 signal (Figure 9e). In agreement with the intensity distribution 0-50μm from the insertion site, there was a significant increase in the number of microglia 7d p.i. compared to 0d and 28d p.i. ($p < 0.05$).

3.4.5 Investigating the Presence of Astrocytes

GFAP is a commonly used marker to visualize astrogliosis, an astrocytic reaction to injury. On the day of the implant, the insertion sites show normal resting astrocytes

surrounding the implant (Figure 8d). After 7d there was a substantial increase in GFAP expression in astrocytes near the insertion sites (Figure 8e). In their reactive state, astrocytes surrounding the insertion sites became hypertrophic and elongated with thick processes. This was in contrast to astrocytes exhibiting a stellate appearance approximately >300μm away. GFAP expression was maximum immediately adjacent to the insertion site and declined progressively as a function of distance to the site. By 28d, the GFAP positive zone became compact around the insertion site, approximately <100μm in radius (Figure 8f). These astrocytes exhibited an interwoven appearance when examined at high magnification. The highly organized structure surrounding the insertion sites was similar to that observed in the H&E stained sections of the same time point (Figure 8c).

3.4.6 Investigating the Expression of Vimentin

Vimentin is expressed in immature and reactive astrocytes, microglia, fibroblasts, as well as endothelial cells. On the day of the implant, vimentin expression was observed only in vasculature primarily >100μm from the insertion sites (Figure 8g). After 7d p.i., an amplification in vimentin expression was observed <100μm from the insertion sites (Figure 8h). After 28d p.i., vimentin expression within 100μm from the insertion sites had decreased compared to 7d p.i. (Figure 8i).

3.4.7 Quantifying GFAP/vimentin Expression

The intensity of GFAP and vimentin stained sections was quantified as a function of distance from the insertion sites. Figure 10a shows the distribution of GFAP surrounding the insertion site. Figure 10b shows the distribution of vimentin surrounding the insertion site. The area under the intensity curve from 0-100μm, 100-300μm, and 300-500μm away from the interface are plotted as mean $\pm$ SD (Figure 10c-GFAP and Figure 10d-vimentin). Differences in intensity were observed as a function of time. GFAP intensity was greater within 100μm from the insertion site after 7d p.i. and

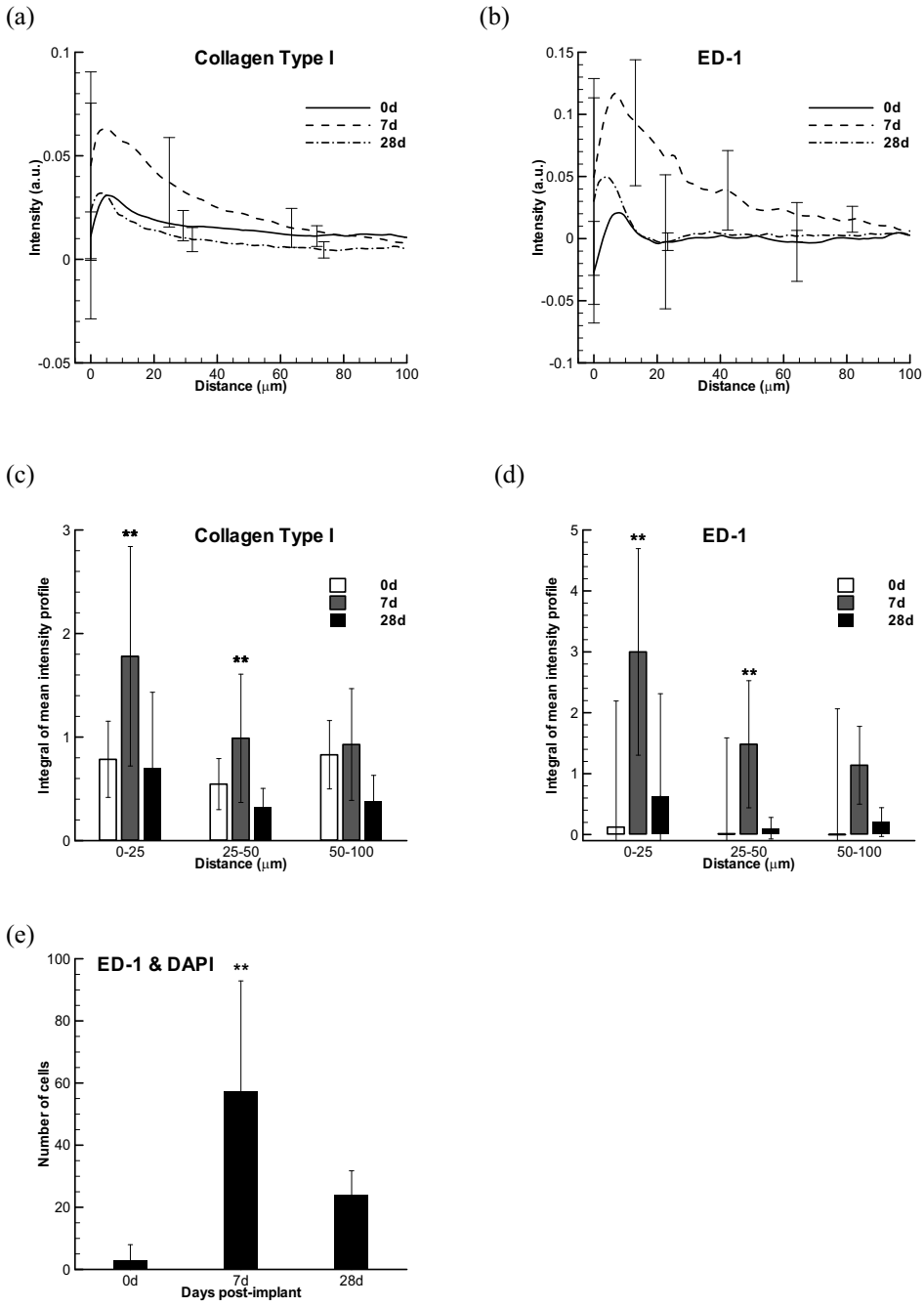

Figure 9: (a)-(e) Coll I and ED-1 image quantification results (summary of sections $\sim$200, 600 and 1000μm below the surface of the cortex). (a) Mean $\pm$ SD intensity profiles for Coll I. (b) Mean $\pm$ SD intensity profiles for ED-1. The integrals from the intensity profiles were calculated 0-25μm, 25-50μm and 50-100μm from the interface and used to compare intensity between groups as a function of distance from the probe site (Col I-(c), ED-1-(d)). ** indicates a significant difference relative to the 0d and 28d conditions within the same distance range ($p < 0.05$). (e) Segmentation and counting of colocalized ED-1$^+$ and DAPI$^+$ regions. ** indicates a significant difference relative to the 0d and 28d condition within the same distance range ($p < 0.001$ & $p < 0.05$ respectively).

28d p.i. compared with the 0d p.i. conditions ($p < 0.01$). Vimentin intensity was greater within 100μm from the insertion site after 7d p.i. compared with both the 0d p.i. and 28d p.i. conditions ($p < 0.01$). GFAP expression 7d p.i. was distributed over a wider region as indicated by significantly higher expression 100-300μm compared to the 0d condition ($p < 0.01$).

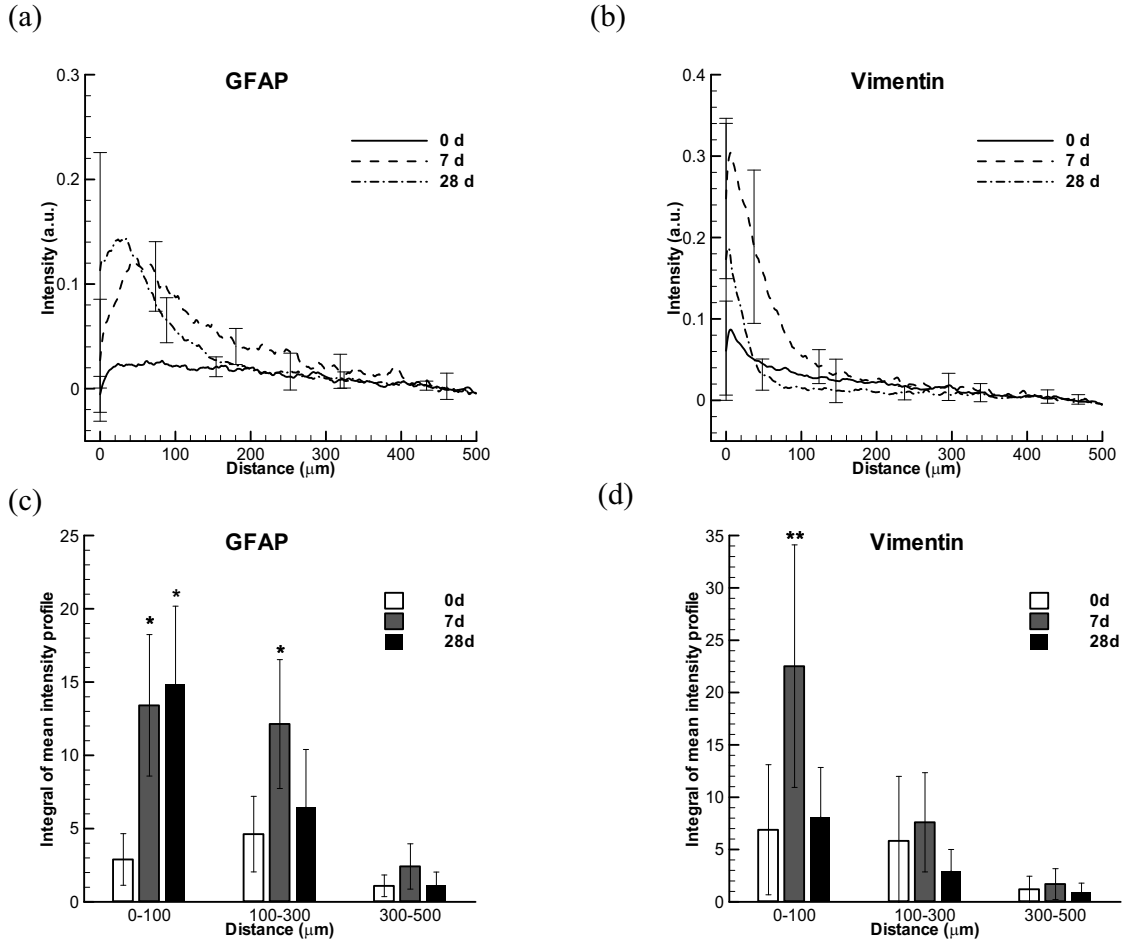

Figure 10: (a)-(e) GFAP and vimentin image quantification results (summary of sections ~200, 600 and 1000μm below the surface of the cortex). (a) Mean ± SD intensity profiles for GFAP. (b) Mean ± SD intensity profiles for vimentin. The integrals from the intensity profiles were calculated 0-100μm, 100-300μm and 300-500μm from the interface and used to compare intensity between groups as a function of distance from the probe site (GFAP-(c), vimentin-(d)). ** indicates a significant difference relative to the 0d condition and 28d condition within the same distance range (all $p < 0.01$).

Table 2: Results of correlation testing between integrated pixel intensity and peak force (data shown in Figure 11).

Primary	Probe design	Pearson's coefficient (r)	p-value
Coll I	3mm_125	0.61	0.046*
Coll I	4mm_200	0.44	0.16
ED-1	3mm_125	0.024	0.94
ED-1	4mm_200	0.49	0.1
GFAP	3mm_125	0.96	1.33e-6*
GFAP	4mm_200	0.68	0.016*
Vimentin	3mm_125	0.66	0.028*
Vimentin	4mm_200	0.11	0.74

* indicates a significant correlation between integrated pixel intensity and peak force for that particular marker ($p < 0.05$). GFAP was the only marker which we studied to be significantly correlated with peak extraction force within both electrode designs.

There was a significant correlation between GFAP intensity 0-100μm from the insertion site and peak extraction force ($r = 0.67$, $p < 0.05$; $r = 0.81$, $p < 0.01$ with removal of one outlier greater than 2.5 SD from the mean) (Figure 11c; Table 2). No significant correlations were observed between Coll I/ED-1/vimentin and peak extraction force for the 4mm_200 implants (Figure 11a, Figure 11b, and Figure 11d respectively; Table 2). The correlations between Coll I/vimentin and peak extraction force were still not significant after the removal of one outlier from each greater than 2.5 SD from the mean ($r = 0.39$, $p = 0.24$; $r = 0.44$, $p = 0.17$ respectively).

3.4.8 Investigating the Influence of Intershank Distance on Astrogliosis and Peak Extraction Force

To shed further light on the relationship between intershank distance, astrogliosis, and peak extraction force, six additional rats were implanted with 12 electrodes and subsequently extracted at identical time points as before (n = 4 per time point). It has been reported that closer shank spacing elicits a stronger astrocytic response [102].

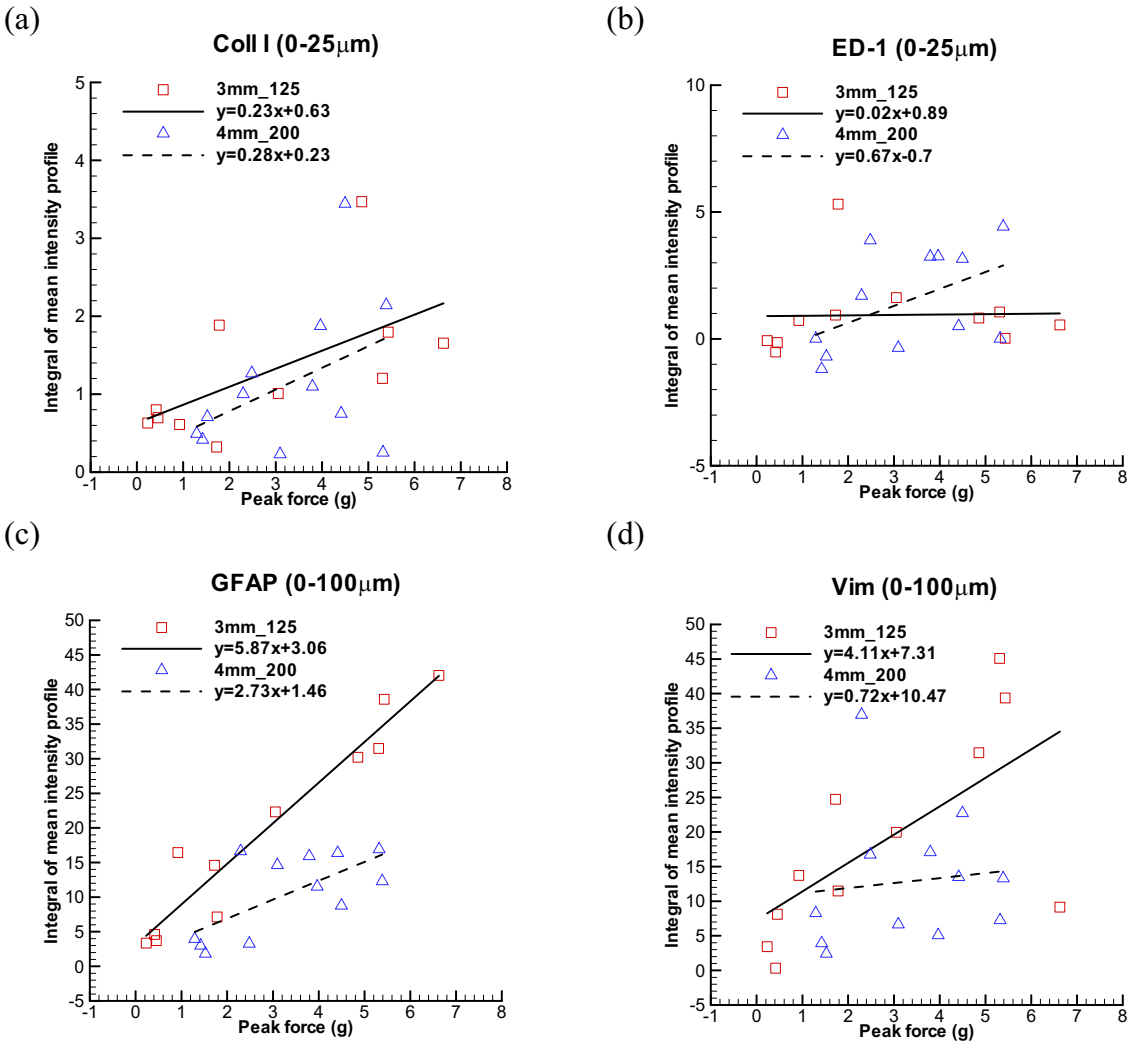

Figure 11: (a)-(d) Scatter plots of the integrated pixel intensity for Coll I (a), ED-1 (b), GFAP (c) and Vimentin (d) 0-25μm (a)-(b) and 0-100μm (c)-(d) from the interface vs. peak force measured for two different probe designs. The mean pixel intensity integrals were used to give a one to one mapping between intensity and peak force. Integrated pixel intensity was chosen over the distances of 0-25μm (a)-(b) and 0-100μm (c)-(d), since the primary differences in signal intensity were within these ranges (see Figure 9c,d & Figure 10c,d). Corresponding Pearson's coefficients, with p-values, are given in Table 2.

We therefore chose an electrode design with a closer shank spacing of 125μm tip-to-tip. The data from one trial in the 0d group was not collected due to breakage of the electrode bondpad during insertion.

Consistent with the 4mm_200 design, there was a strong correlation between GFAP and peak extraction force ($r = 0.96$, $p < 0.001$) (Figure 11c). Also of note was that 28d p.i., both the peak extraction forces and GFAP intensity 0-100μm from the insertion sites were higher for the 125μm spaced electrodes than for the 200μm spaced electrodes ($p < 0.001$).

Sections from the 3mm_125 implanted brains were also immunostained for Coll I, ED-1, and vimentin and quantified using the same methods that were used for the 4mm_200 implants. In contrast to the 4mm_200 electrode design, we observed a significant correlation between Coll I and peak extraction force (Figure 11a; Table 2) along with vimentin and peak extraction force (Figure 11d; Table 2). No significant correlation was observed between ED-1 and peak extraction force for the 3mm_125 implants (Figure 11b; Table 2).

3.4.9 Investigating Involvement of Laminin in a Mechanism for Astrocytic Adhesiveness

LN is a major component of the ECM and is found in basal lamina. It is also known that astrocytes produce LN and that the production of LN is amplified in their reactive state [80]. To study the potential influence of LN on the mechanical integration between astrocytes and the electrode, double staining of LN and Reca-1 staining was used. This method allowed detection of the presence of LN near the electrode-tissue interface, while excluding LN found in basal lamina of endothelial cells (Reca-1). We observed no LN around the interface in the 0d and 7d conditions, but sporadically observed LN at the interface for the 28d case. The intense LN signal surrounding the interface was not colocalized with Reca-1, a marker specific for endothelial cells (Figure 12).

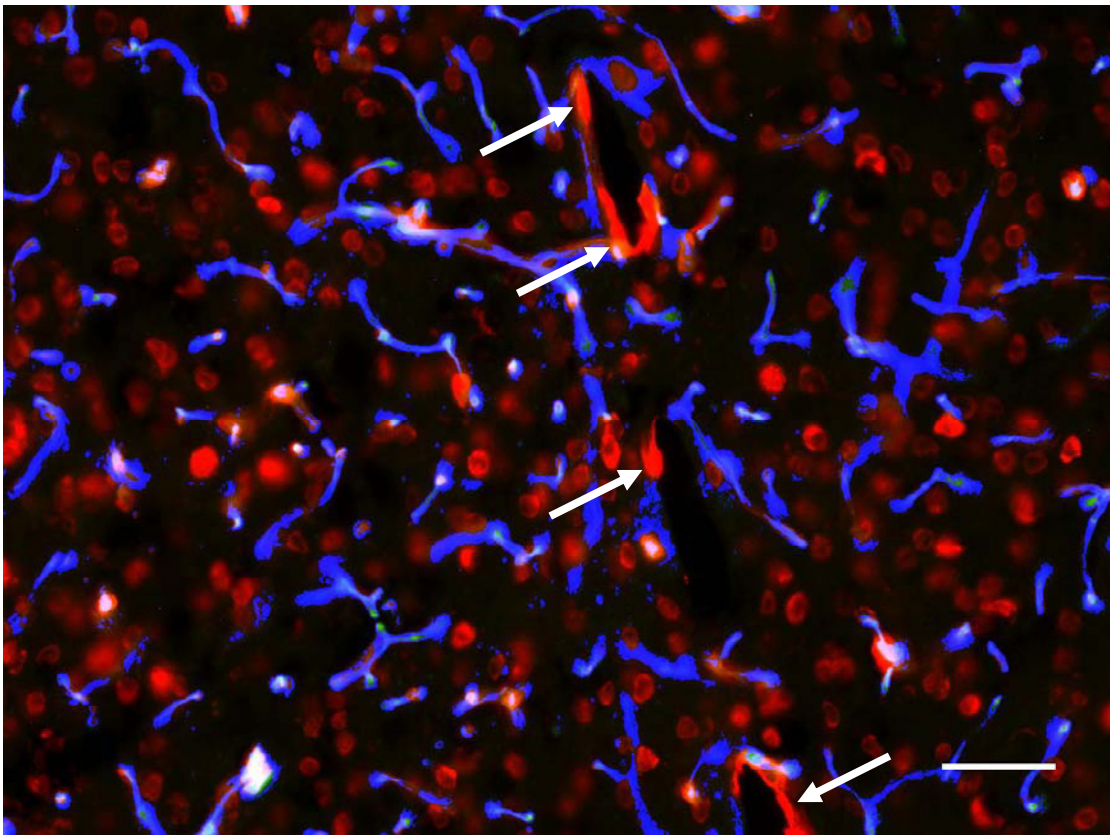

Figure 12: Representative overlay of LN (red) and Reca-1 (green) staining from a 28d p.i. brain section, imaged using a 40X objective. The section was collected at a depth of $\sim$600μm below the brain surface. To aid in visualization, colocalized pixels are shown in blue. Arrows point to the strong LN$^+$/Reca-1$^-$ signal observed at the electrode-tissue interface in the 28d condition. Scale bar=30μm.

3.5 Discussion

We observed an increase in peak extraction force while extracting electrodes as the post-implant time increased. At the onset of extraction of the electrode, the majority of the bonds between the electrode and surrounding tissue are broken which corresponds to our measurement of peak extraction force. Previous modeling results [77, 133] reported that attachment of tissue to the electrodes, as we detected in our measurement of peak extraction force, translates to a reduction in strain due to the anchoring of the electrode to the surrounding tissue. We hypothesized that over time tissue integration with the electrode would result in a higher peak extraction force, with a possible mechanism being cellular processes integrated with the surrounding ECM and the electrode. We investigated the possible cellular and matrix contributors to this increase by examining several candidate cell types including endothelial cells, microglia, astrocytes, and meningeal fibroblasts. Endothelial cells are an unlikely contributor to this increase in peak extraction force as we observed few blood vessels immediately adjacent to the insertion sites. This observation is in contradiction to the interpretation of the LN^+ signal observed on retrieved electrodes from a previously reported study, and implies that the vasculature is not in direct contact with the electrode surface [132]. This was also supported by the absence of Reca-1 signal on retrieved electrodes (data not shown).

We examined the possibility for activated microglia being a contributor to peak extraction force increase. These cells were observed on explants 7d and 28d p.i. and immediately adjacent to the insertion sites in corresponding tissue sections. ED-1 staining showed a decreased number of microglia encircling the electrode at 28d p.i. in comparison with 7d p.i. as previously reported in rats [142, 139, 7]. However, ED-1 was uncorrelated with peak extraction force in either electrode design, suggesting that these cells are not a primary contributor to the observed force increase (Figure 11b; Table 2).

We also examined the likelihood for meningeal cells contributing to the increase in peak extraction force. Meningeal cells are fibroblast-like cells found in the meninges, including both the dura mater and pia mater. The presence of meningeal cells at the electrode-cortical interface was evidenced by the presence of Coll I. Coll I is the most abundant form of collagen found in the body, however, it is absent in healthy neural tissue; Coll I is abundant in the pia mater [129]. The intense Coll I staining around the insertion sites near the cortical surface suggest that meningeal cells migrated, at least to some extent, along the electrode shanks into the cortical tissue. Quantitatively, however, no correlation between Coll I and peak extraction force or vimentin signal and peak extraction force was seen in the 4mm_200 implants (Figure 11a,d; Table 2). This data set suggests that it is unlikely meningeal cells are a primary contributor to peak extraction force. For the 3mm_125 implants a differing time course for Coll I and vimentin expression was observed. The reason for the differing response of Coll I and vimentin expression between electrode types is unclear. Due to the significant correlation between Coll I/vimentin and peak extraction force within the 3mm_125 implants, a contribution from fibroblasts to the peak extraction force cannot be excluded (Figure 11a,d; Table 2).

Along with previous studies investigating the electrode-tissue interface over time, we observed a compact layer of reactive astrocytes at the insertion site after 28d p.i. [142, 139]. Evidence for the contribution of astrocytes to peak extraction force is the strongest of any cell type. Qualitatively, the observed changes at the interface in astrocytes correlate temporally with peak extraction force in both electrode designs. Quantitatively, GFAP stained sections showed the strongest positive correlations between intensity surrounding the insertion sites and peak extraction force and was the only marker which was significantly correlated with peak extraction force for both of the electrode designs (Figure 11c; Table 2). We further investigated LN surrounding the electrode site, as a potential mechanism by which astrocytes adhere to the

electrodes. However, we observed a high variability in the presence of LN^+/Reca-1^- signal near the electrode sites. This may be due to disruption of the interface during removal of the electrodes and may require a technique capable of imaging the intact electrode-tissue interface.

Our observed relationship between intershank distance, astrogliosis, and peak extraction force warrants further investigation. Significant differences were observed between the different electrode designs of 125μm tip spacing and 200μm spacing with the latter design having less astrogliosis after 28d p.i. Considering that the width of each shank for the 4mm_200 electrodes was approximately twice that of the 3mm_125 electrodes, in the case of this study, spacing of multishank MEAs had a larger influence on the chronic astrogliotic response than shank size. Shanks spaced closer together may induce more tissue reaction due to overlapping areas of tissue reaction between shanks. It may also be that the tissue within these overlapping areas responds synergistically. These observations corroborate work previously presented [102].

The electrode was not tethered to the skull in the implantation model we used. Encasing the electrode in a hydrogel, untethered, allowed us to easily remove the brain from the skull while leaving the the electrodes intact. This enabled the measurement of extraction force in the absence of complications such as presence of the dura matter, or clotted blood. However, the use of an untethered electrode model likely underestimates the tissue reaction when compared to chronic electrodes which have been tethered to the skull [7].

Due to technical challenges, we were not able to measure force contribution as a function of distance along the electrode. Therefore we are able only to speculate on the distribution of tissue integration contributing to peak extraction force along the electrodes based on histology results from brain sections. Based on previous modeling results [77, 133], the distribution of force affects interfacial strain in two ways: in the case where 1) the force is entirely due to the pial-electrode interface

with integration at the bondpad, the strain would be increased at the tip compared with the case where 2) the force is largely due to the electrode-cortical interface, with strain distributed equally along the electrode. In case 2) the strain distribution would be reduced and more uniformly distributed along the shaft compared with case 1). While case 2) is strongly supported from our results, regardless of these two distribution profiles, previous modeling results [77, 133] found that the strain fields predicted in the case where surrounding tissue is adhered to the electrode are less than the case in which the tissue is non-adherent. In other words, attachment of tissue to the electrodes translates to a reduction in strain due to the anchoring of the electrode to the surrounding tissue. The results of this study combined with previous modeling studies suggest that astrogliosis, while injurious to recording quality, may limit further injury by stabilizing chronically implanted MEAs. How effective this stabilization is at minimizing strain is an interesting question for future studies. Currently, the precise levels of strain required to adversely affect glial cells are unknown.

3.6 Acknowledgements

The authors would like to thank Dr. Robert Lee for use of the micromanipulator and air table and Randy Weinstein for instruction in operating the micromanipulator. The authors would also like to thank Dr. Wei He and Dr. Young-tae Kim for many helpful discussions.

CHAPTER IV

CHRONIC INFLAMMATION SURROUNDING INTRA-CORTICAL MICROELECTRODE ARRAYS RESULTS IN NEURODEGENERATION IN TARGET NEURONS

4.1 Abstract

Thanks to pioneering scientists and clinicians, prosthetic devices that are controlled by intracortical electrodes recording one's 'thoughts' are a reality today, and no longer merely in the realm of science fiction. However, widespread clinical use of implanted electrodes is hampered by a lack of reliability in chronic recordings, independent of the type of electrodes used. The dominant hypothesis has been that astroglial scar electrically impedes the electrodes. However, there is a time delay between when scar electrically stabilizes and when recordings fail (∼1 month lag), suggesting that scar, alone, does not cause recording unreliability. In this study, we test an alternative hypothesis: that chronic inflammation, due to the persistent presence of the electrode, causes a local neurodegenerative state. Through modulation of chronic inflammation via stab wound, electrode geometry, and age-matched control, we found that after 16 weeks, animals with an increased level of chronic inflammation were associated with increased neuronal and dendritic, but not axonal, loss. We moreover, observed increased neuronal and dendritic loss 16 weeks after implantation compared to 8 weeks after implantation, suggesting that the local neurodegenerative state is progressive. After 16 weeks, we observed axonal pathology in the form of hyperphosphorylation of the protein Tau in the immediate vicinity of the microelectrodes (as observed in

Alzheimer's Disease and other tauopathies). The results of this study suggest that a local, progressive neurodegenerative disease-like state surrounds chronic electrodes and is a potential cause of chronic recording failure. These results also inform strategies to enhance our capability to attain reliable long-term recordings from implantable electrodes in the CNS.

4.2 Introduction

Thanks to pioneering scientists and clinicians, prosthetic devices that are controlled by intracortical electrodes recording one's 'thoughts' are a reality today, and no longer merely in the realm of science fiction [16, 20, 60, 76, 126, 141, 149]. However, widespread clinical use of implanted electrodes is hampered by a lack of reliability in chronic recordings, independent of the type of electrodes used. The dominant hypothesis in the field has been that astroglial scar, formed around implanted electrodes either due to insertion-associated injury, presence of a foreign material, and/or due to mechanical mismatch between the stiffness of the electrode and the brain, isolates the implanted electrodes from the brain, resulting in recording failure.

However, there are several reasons why astroglial scar, per se, may not be the cause of recording unreliability. First, the impedance changes due to scar are not so dramatic that it should interfere with ability to record [96]. Second, chronic recording failure often occurs several weeks after scar has developed and stabilized from an electrical perspective [84, 100, 115, 152]. Therefore, the observation that it is not until several weeks after electrical impedance has stabilized that neural signals fade implies that the electrical properties of the scar are likely not the primary reason for recording failure/unreliability.

Previous studies have suggested that chronic inflammation surrounding microelectrodes is persistent and is accompanied by neuronal cell death and loss of processes 4

weeks post implantation [7, 8]. However, little is known about the state of target neurons at more chronic end points, nor whether or not degeneration of target neurons is correlated with chronic inflammation at the electrode interface. In this study, we investigated the tissue response to implant durations of 8 weeks and 16 weeks, long after the astroglial scar electrically stabilized and more in line with when researchers have reported that recording failure occurs. We hypothesized that chronic recordings fail due to a local neurodegenerative state developing in the vicinity of chronically implanted electrodes, and that this neurodegenerative state is characterized by neuronal loss, dendritic loss, and axonal pathology in close proximity to the electrode surface, leading to recording signal loss/degradation due to the 'unplugging' of surviving neurons close to the electrode (<200 μm from the electrode surface) from their physiological networks. As a first step toward testing this hypothesis, in this study we show that chronic, local inflammation due to the continuous presence of implanted electrodes is correlated with local neurodegeneration characterized by neuronal loss, dendritic loss, and tauopathy.

4.3 Materials and Methods

4.3.1 Surgical procedures for chronic implants

'Michigan probes' with four shanks were used in this study (NeuroNexus Technologies). Three end points after electrode implantation were investigated and were chosen based on the time course of astroglial scar development: 2 weeks, 8 weeks, and 16 weeks. Rats were implanted with electrodes with thickness of 15 μm, length of 4mm, shank width of 60-100 μm, and tip spacing of 200 μm (abbreviated 4mm_200). As a control for the acute injury due to electrode insertion, an additional group of six rats were inserted with electrodes and retrieved 2 min after insertion (abbreviated S.W. for stab wound), then sacrificed 16 weeks later. In a previous study we found that decreased shank spacing resulted in increased astrogliosis after 4 weeks [93].

Table 3: Experimental design: Animal numbers for conditions

Duration (weeks)	4mm_200	3mm_125	4mm_200 (stab wound)	No implant
2	6	0	0	0
8	5	0	0	0
16	6	6	6	2

Therefore, an additional group of animals were implanted with an electrode design of closer inter-shank spacing, to study the influence of increased chronic inflammation on nearby neurons. Six rats were implanted with electrodes with thickness of 15 μm, length of 3 mm, shank width of 30-100 μm, and tip spacing of 125 μm (abbreviated 3mm_125) at only the 16 week end point (Table 3) for experimental design).

Adult male Sprague-Dawley rats (275-299 grams) were anesthetized for 5 min with a mixture of 5% isoflurane and 1 L/min O_2 prior to surgery. Each rat was positioned into a stereotactic frame (Kopf) where anaesthesia was maintained to effect ($\sim$1-3% isoflurane and 0.3 L/min O_2) during surgery by monitoring the rat's breathing. The rat's head was shaven over the incision area and the skin was disinfected with isopropyl alcohol and chlorohexaderm using a slight scrubbing motion before making the incision. Ophthalmic ointment was applied to the eyes to prevent drying. A midline incision was made along the scalp, the skin retracted, and the periosteum cleared to expose the bregma. A dental drill was used to create a 3.2 mm hole at +0.2 mm anterior and +3.0 mm lateral to the bregma with a custom trephine (24 tooth x 3 mm O.D.) fabricated from stainless steel tubing (Small Parts). In order to minimize iatrogenic damage, room temperature saline was applied liberally to the spinning drill bit at the bone interface. The bone plug was carefully removed and the dura was gently pierced and retracted using a 28 gauge needle with the tip bent at a 45°angle. The bond-pad region of the microelectrode was grasped with Teflon-coated microforceps and the penetrating shanks were inserted stereotaxically through the pia mater into the cortex. Care was taken to minimize bleeding by avoiding insertion

through large surface blood vessels. The electrode was inserted to the point where only the bond-pad region was visible outside of the cortical surface. After the insertion, the bond-pad region of the electrode and the craniotomy was covered with 1% SeaKem Agarose (Cambrex) gel in phosphate buffered saline (PBS). A craniotomy of identical diameter was made over the contralateral location (+0.2 mm anterior to the Bregma and -3.0 mm lateral to the midline suture) where an additional electrode, of identical design to that implanted in the contralateral hemisphere, was inserted and protected with agarose the same way as described above. The craniotomies were further sealed and protected using dental acrylic anchored to the skull with bone screws (Plastics One, Inc.). The skin was closed with wound clips and the rats were monitored until recovery from anesthesia. To minimize variability associated with the surgery, all implants were performed by the same surgeon. All procedures were approved by Georgia Tech Institutional Animal Care and Use Committee.

4.3.2 Brain tissue preparation for immunohistochemistry

After 2 weeks, 8 weeks, or 16 weeks, each animal was anesthetized with a mixture of ketamine (45.65 mg kg^{-1}), xylazine (9.13 mg kg^{-1}) and acepromazine (1.52 mg kg^{-1}), then transcardially perfused with PBS prewash followed by 4% paraformaldehyde in PBS. The brains were removed and postfixed overnight (4 ℃). Following the retrieval of the electrodes, rat brains were placed into 30% sucrose (4 ℃) until they sunk to the bottom. A tissue dye was then carefully applied to the left-posterior hemisphere to later identify the orientation of the brain sections and align images with the same electrode orientation. The brains were then cryoprotected with Optimal Cutting Temperature (O.C.T.) compound (Tissue-Tek). Horizontal tissue sections were cut to a final depth of $\sim$2 mm from the surface of the cortex for all brains. Serial sections were cut 30 μm in thickness with the exception of every 13th section, which was cut 14 μm in thickness. The 14 μm sections were mounted directly to glass slide and

stained with Hematoxylin and Eosin (H&E) using a Leica Autostainer XL, while the 30 μm sections were serially stored in two six-well plates at 4 ℃ in PBS with 0.01% sodium azide to minimize bacterial contamination.

4.3.3 Immunohistochemistry

To study brain tissue response, sections taken from all brains were stained simultaneously for the antibody of interest. Sections from adjacent wells, with five sections per well, were used to stain for ED-1, MAP-2 and double-stain for GFAP/NeuN, and NF-200/Tau-1 respectively. These stains were used to visualize the presence of activated microglia/macrophages (ED-1), astrocytes (GFAP), neuronal nuclei (NeuN), dendrites (MAP-2), and axons (NF-200 and Tau-1) (Table 4). The five sections per well ranged from $\sim$200 μm to $\sim$2 mm below the surface of the cortex and were spaced at uniform intervals of 374 μm. Sections were blocked in 4% normal goat serum (GIBCO) with PBS containing 0.5% Triton X-100 (Sigma) for 1 hr at room temperature. Sections were then immediately incubated overnight at 4 ℃ with primary antibody prepared in blocking solution. Primary antibodies used are shown in Table 4. After washing in 0.5% triton in PBS, sections were incubated in secondary antibodies for 1 hr at room temperature. Secondary antibodies were diluted at a ratio of 1:220 in 0.5% triton in PBS, and included goat anti-rabbit IgG (H + L) Alexa 488 (Molecular Probes) and goat anti-mouse IgG1 Alexa 594 (Molecular Probes). All sections were counterstained by incubation with the nuclear dye DAPI (Molecular Probes) that labels all cell nuclei. An additional cortical section from each rat brain was used to control for non-specific secondary antibody labeling, by omitting the primary incubation step (primary control). Tissue sections were mounted on glass microscope slides with Fluoromount-G (Southern Biotechnology Associates).

Table 4: List of primary antibodies

Primary	Host	Isotype	Dilution	Vendor	Antigen	Cell Specificity
CD68 (ED-1)	Ms	IgG1	1:1000	Serotec	Lysosomal glycoprotein	Activated microglia/macrophages
GFAP	Rb	IgG	1:2000	DAKO	Glial fibrillary acidic protein	Astrocytes
NeuN	Ms	IgG1	1:500	DAKO	Neuronal nuclei	Neurons
MAP-2	Ms	IgG1	1:1000	Chemicon	Microtubule-associated protein	Neurons
NF-200	Rb	IgG	1:1000	Sigma	Heavy neurofilament polypeptide	Neurons
Tau-1	Ms	IgG2a	1:200	Chemicon	Microtubule-associated protein	Neurons
pT231	Ms	IgG1	1:2000	Chemicon	PhosphoThreonine 231	Neurons

For hyperphosphorylated Tau staining, two additional rats were implanted with four-shank silicon microelectrode arrays (4mm_200 design) and perfused 16 weeks later using 4% paraformaldehyde + 0.1% glutaraldehyde. Brains were then postfixed 1 hr in the same solution and sectioned using a vibratome (thickness = 50 μm). Additionally, human brain sections, acquired using a cryostat to 50 μm thickness, were stored in cryoprotectant. After 5 rinses in PBS, sections were incubated for 10 min in 3% hydrogen peroxide. Sections were rinsed, and blocked for 1 hr at 4 ℃ in blocking solution containing 8% horse serum, avidin (10 μg/ml), and 0.1% Triton-X. Sections were then incubated with pT231 (see Table 4), AT8 (Pierce; 1 μg/ml), or Alz50 (diluted 1:100) in solution with 2% horse serum and biotin (50 μg/ml). Next, sections were incubated with biotinylated donkey anti-mouse secondary (Jackson Immunochemicals; dilution 1:200 for 1 hr at 4 ℃, and then visualized using a VECTASTAIN Elite ABC kit (Vector Laboratories).

4.3.4 Fluoro-Jade C staining

Sections were stained using Fluoro-Jade C, a sensitive marker for degenerating neuronal cell bodies and processes, as previously described [121]. Briefly, sections were mounted onto gelatinized slides and dried overnight at room temperature. Slides were immersed in 100% EtOH for 3 min, followed by 70% EtOH for 1 min, and rinsed with distilled water. Slides were placed in 0.06% KMnO4 on a shaker plate for 15 min. After rinsing in distilled water for 1 min, slides were stained in a solution of 0.001% Fluoro-Jade C dissolved in 0.1% acetic acid vehicle. Sections were rinsed three times in distilled water, then dried at room temperature, cleared, and coverslipped.

4.3.5 Quantitative analysis of histological images

Fluorescent and brightfield images were acquired using a Microfire digital camera and a Zeiss Axioskop2 Plus upright microscope with a 10X objective, with the electrode sites centered in the camera field (Figure 13 and Figure 16). Four sections

approximately 200 μm, 600 μm, 1000 μm, and 1400 μm below the brain surface were imaged for quantification to investigate the response at different depths in the cortical column. All tissue sections were imaged in a single session to minimize variability. The exposure time was consistent within each marker and was set below saturation of the digital camera. Fluorescent intensity as a function of distance from the electrode-tissue interface was calculated for GFAP, ED-1, MAP-2, Tau-1, NF-200, and Fluoro-Jade C stained sections using MATLAB (with Image Processing Toolbox, Mathworks), as previously described [93]. Briefly, images were first rotated such that the four insertion sites were aligned vertically. An ellipse was computed from five or more user-specified points around each of the four insertion sites using the brightfield image to delineate the electrode-tissue interface and the location of the ellipses were then saved to file. Saved ellipse points were then used in the corresponding immunostained images to segment rectangular regions from the middle of each ellipse to a distance of 500 μm away for both the left and right sides. The intensity values of each of the boxed regions were then averaged along the y-axis to create two mean intensity profiles for each insertion site. The mean of the eight line profiles was then computed. For normalization, the average intensity from 400-500 μm in each image was subtracted from the intensity profile 0-500 μm. The integral of the mean intensity profile at six different distance increments along the electrode (0-50 μm, 50-100 μm, 0-100 μm 100-200 μm, 200-300 μm and 300-500 μm) was also calculated for each image. NeuN images were segmented using a marker-based watershed algorithm.

4.3.6 Statistical analysis

All statistical inferences were made between differing time points using one-way standard analysis of variance. When we found a significant difference between groups, we performed the Tukey's Honest Significant Difference (HSD) post-hoc test to identify pairwise differences. For all tests, $p < 0.05$ was considered significant.

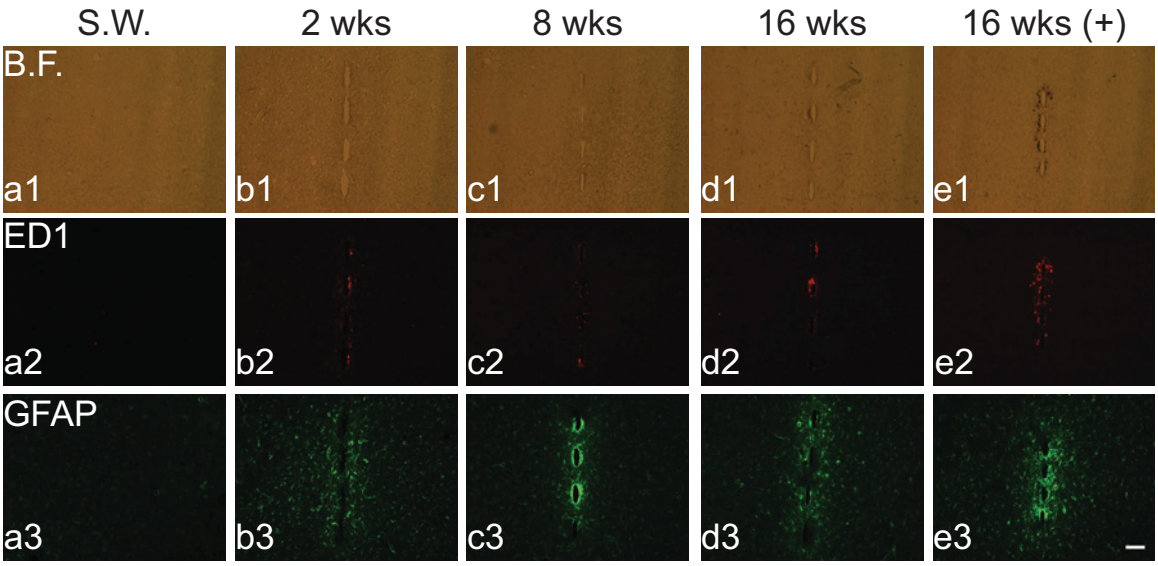

Figure 13: Representative brightfield (B.F.) (a1)-(e1), ED-1 (a2)-(e2), and GFAP (a3)-(e3) stained images from all conditions. Horizontal sections contain the four electrode tracks in the center of each image. S.W. = stab wound. (a1)-(e1) Hemosiderin-laden macrophages were observed primarily in the 16 week (+) control condition. (a2)-(e2) ED-1 was present primarily within the first one to two cell lengths away from the electrode. (a3)-(e3) GFAP expression was most compact at the inteface after 8 weeks and 16 weeks compared to 2 weeks. The stab wound condition showed no positive signal for hemosiderin-laden macrophages, ED-1, or increased GFAP relative to background, indicating the acute trauma associated with the insertion of the electrode does not result in a persistent inflammatory response.

4.4 Results

4.4.1 Evidence for local, persistent inflammation

4.4.1.1 Activated Microglia (ED-1)

Activated microglia form a front line of defense, and their presence was primarily at the electrode interface. Predominantly, they were found within the first 25 μm away from the electrode (Figure 14a). Few activated microglia were observed after 2 weeks. After 8 weeks, the numbers were slightly larger, and had decreased again after 16 weeks (Figure 14b). After 16 weeks, the 125 μm spaced electrode design showed the greatest number of activated microglia compared to any condition. In the case of stab wound, no ED-1 (+) signal was observed.

4.4.1.2 Astrocytes (GFAP)

As expected from previous studies, GFAP expression was increased in the tissue surrounding the microelectrodes [139, 142]. The characteristics of the GFAP expression differed with distance from the electrode at the three different end points (2, 8, 16 weeks) (Figure 13 and Figure 14c). After 2 weeks, the peak of the intensity curve was at $\sim$50 μm away from the electrode. After 8 weeks, the peak in GFAP expression was even closer to the electrode. After 16 weeks, the expression levels of GFAP were next to the electrode, but were more distant from the electrode compared to the 8 week time point and had decreased in intensity. Any indication of increased GFAP relative to background surrounding the electrode tracks was not observed in the case of the stab wound. GFAP levels for the 125 μm, 16 week (+) control, electrode design had a similar profile to that of the 8 week 200 μm spaced electrode design, both being significantly higher than the 16 week condition (Figure 14d).

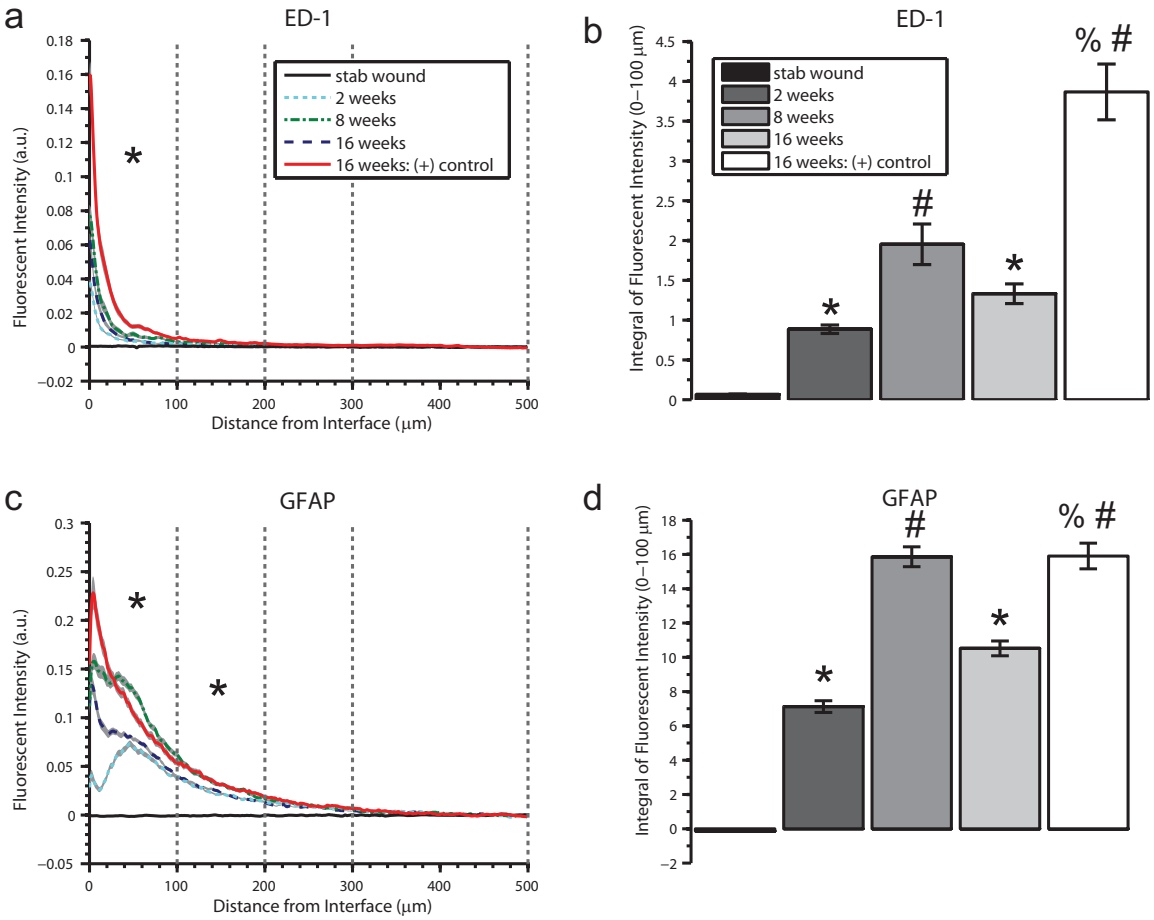

Figure 14: Quantified ED-1 expression (for activated microglia) and GFAP expression (for astrocytes). Results are the mean of the four most superficial sections and are spaced 374 μm through the cortical column. In (a) and (c) the mean $\pm$ SEM (SEM indicated by gray filled area surrounding lines) are shown. Bar graphs in (b) and (d) represent mean $\pm$ SEM. * represents significantly higher than stab wound condition ($p < 0.05$). % represents significantly higher than 8 wk condition (and stab wound). # represents significantly higher than 16 wk condition (and stab wound) ($p < 0.05$). (a) ED-1(+) microglia are located primarily within the first 50 μm away from the electrode. (b) Quantified total ED-1 fluorescent intensity 0-100 μm from the electrode. No ED-1 (+) signal is observed 16 weeks after stab wound injury. For groups in which the electrode remained in the brain for 16 weeks, the 125 μm spaced electrode design had significantly more ED-1 (+) signal, compared to the 200 μm spaced electrode design ($p < 0.05$). (c) Differences in GFAP expression from stab wound group were significant over the first 300 μm. (d) Quantified total GFAP fluorescent intensity 0-100 μm from the electrode.

4.4.1.3 Hemosiderin-Laden Macrophages

Hemosiderin is an iron-binding molecule in the blood, closely related to wüstite, an Fe2+ iron oxide. The presence of hemosiderin indicates that the lesion was hemorrhagic and has been speculated to be a byproduct of oxidative stress [101]. Since oxidative stress has been shown to lead to neurodegeneration [11, 12], we quantified the presence of hemosiderin-laden macrophages next to the electrode. The characteristic granular, olive brown appearance of hemosiderin-laden macrophages under brightfield was used to identify the cells for counting (Figure 15a-c). The deposits were co-localized with ED-1 staining (Figure 13). Quantified hemosiderin-laden macrophages are shown in Figure 15d. Hemosiderin-laden macrophages were only present in three condition: 8 weeks, 16 weeks, and 16 weeks (+) control. These three conditions showed variability in the number of implants surrounded by hemosiderin-laden macrophages (8 weeks: 3/12 implants, 16 weeks: 8/12 implants, 16 weeks (+) control: 11/12 implants). The 16 weeks (+) control condition contained significantly greater numbers of hemosiderin-laden macrophages compared to the other conditions (Figure 15d).

4.4.2 Evidence for local, progressive neurodegeneration

In this section we discuss markers of neuronal health, first at the anatomical level and then at the molecular level.

4.4.2.1 Anatomical markers of neurodegeneration: Neuronal viability (NeuN, Fluoro-Jade C)

Neuronal loss was evident for all conditions except the stab wound in the first 100 μm from the electrode Figure 17a. After 16 weeks, neuronal loss had significantly increased compared to 8 weeks p.i. up to 300 μm from the electrode surface. Comparing NeuN loss between the two electrode designs after 16 weeks, there was significantly more loss in the case of the 3mm_125 design compared to the 4mm_200 design over

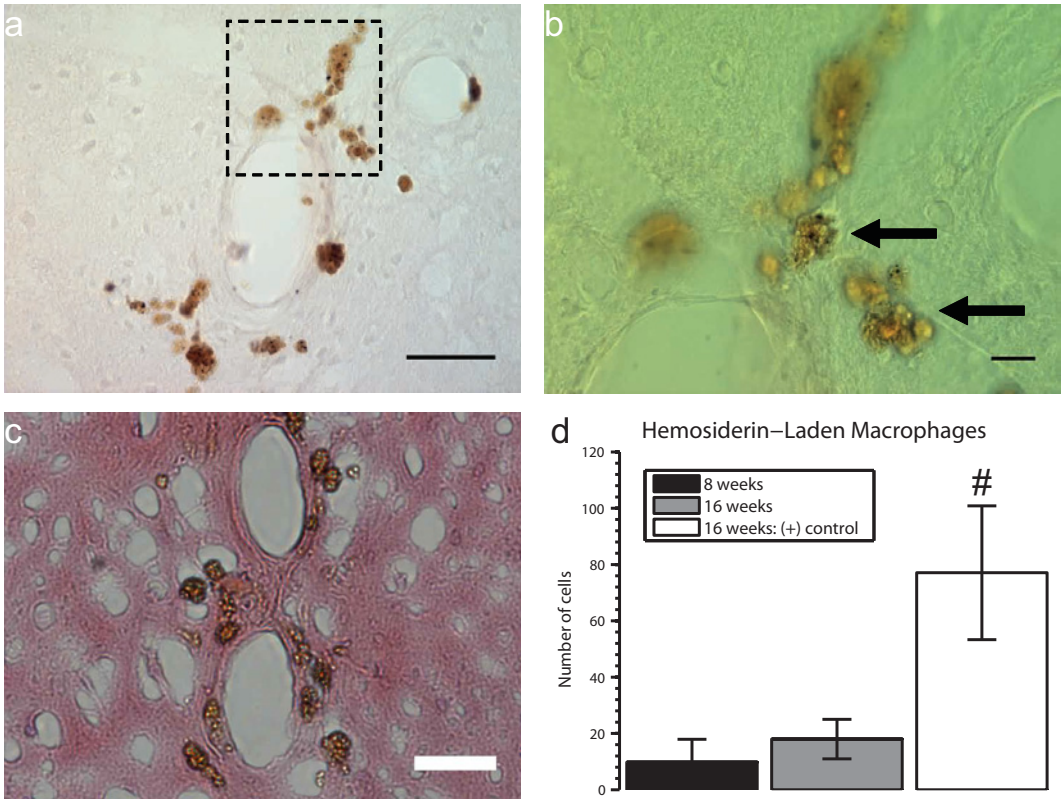

Figure 15: (a) Representative brightfield image 16 weeks post implantation showing hemosiderin-laden macrophages. Scale bar = 50 μm. (b) Boxed region in (a) at higher magnification. Arrows point to granular dark brown structures indicative of hemosiderin-laden macrophages. Scale bar = 10 μm. (c)Hematoxylin and eosin-stained section 8 weeks p.i. showing golden-brown hemosiderin granules. Scale bar = 50 μm. (d) Quantified hemosiderin-laden macrophages. Bar represents mean $\pm$ SEM. # indicates significantly greater than 8 week and 16 week conditions ($p < 0.05$).

the 0-100 μm and 200-300 μm intervals. Fluoro-Jade C staining was confined to processes (Figure 16c2-e2). Fluoro-Jade C staining of similar implants 1 hr and 24 hr post implantation showed staining of neuronal bodies (data not shown), however there was no evidence of apoptosis or necrosis for the 2, 8, and 16 week end points. Fluoro-Jade C intensity in the first 100 μm was significantly higher after 16 weeks compared to 8 weeks (Figure 17c).

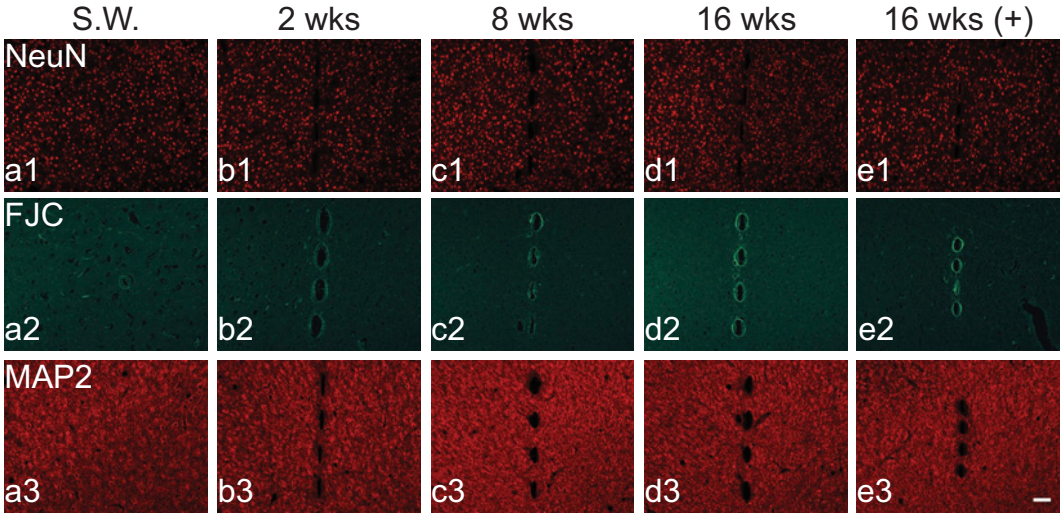

Figure 16: Representative NeuN (a1)-(e1), Fluorojade C (a2)-(e2), and MAP-2 (a3)-(e3) staining from all conditions. Horizontal sections contain the four electrode tracks in the center of each image. S.W. = stab wound.

4.4.2.2 Anatomical markers of neurodegeneration: Dendrites (MAP-2)

While the Fluoro-Jade C stain suggested neuronal processes were dying back near the electrode, it was unclear from these data whether the loss of processes was occurring due to dendrites and/or axons dying back. To further explore where this degeneration is occurring, we used specific immunohistochemical stains for dendrites and axons. To investigate dendritic arborization surrounding the electrode, MAP-2 was fluorescently labeled, while NF-200 and Tau-1 were used to investigate axonal arborization.

No loss in MAP-2 expression was observed in the case of the stab wound (Figure 17d). For the other conditions MAP-2 staining intensity generally followed an

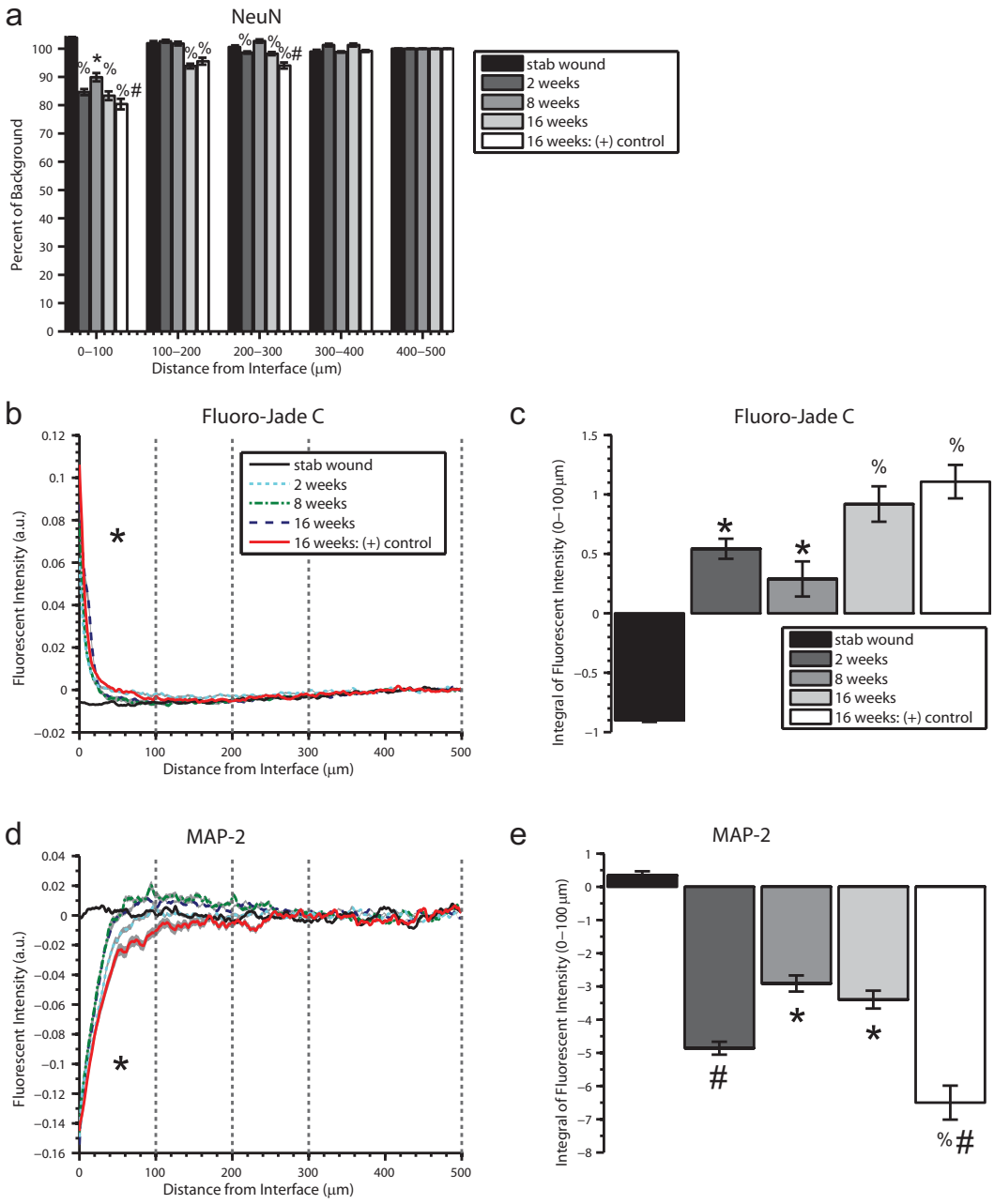

Figure 17: Quantified NeuN expression (for neuronal nuclei), Fluoro-jade C (for degenerating/dying neurons), and MAP-2 (for dendrites). Results are the mean of the four most superficial sections and are spaced 374 μm through the cortical column. In (b) and (d) the mean $\pm$ SEM (SEM indicated by gray filled area surrounding lines) are shown. Bar graphs in (a), (c), and (e) represent mean $\pm$ SEM. * represents significantly higher than stab wound condition ($p < 0.05$). % indicates significantly greater than 8 wk condition (and s.w.) ($p < 0.05$). # indicates significantly greater than 16 wk condition (and s.w. and 8 wk) ($p < 0.05$). (a) Number of NeuN (+) cells, represented as percent of cells 400-500 μm. (b) Fluoro-Jade C as a function of distance from the electrode. (c) Integral of Fluoro-Jade C intensity 0-100 μm from the electrode. (d) MAP-2 staining intensity as a function of distance from the electrode. (e) Integral of MAP-2 intensity 0-100 μm from the electrode. Note: negative intensity denotes loss relative to background intensity.

inverse relationship with ED-1 expression (Figure 17d). The 3mm_125 electrode design had significantly less MAP-2 signal, compared to the 4mm_200 electrode design in the first 100 μm from the electrode (Figure 17e). Dendritic loss was most prominent at deeper depths of the cortical column, at depths of $\sim$1000 μm and $\sim$1400 μm (Figure 18d).

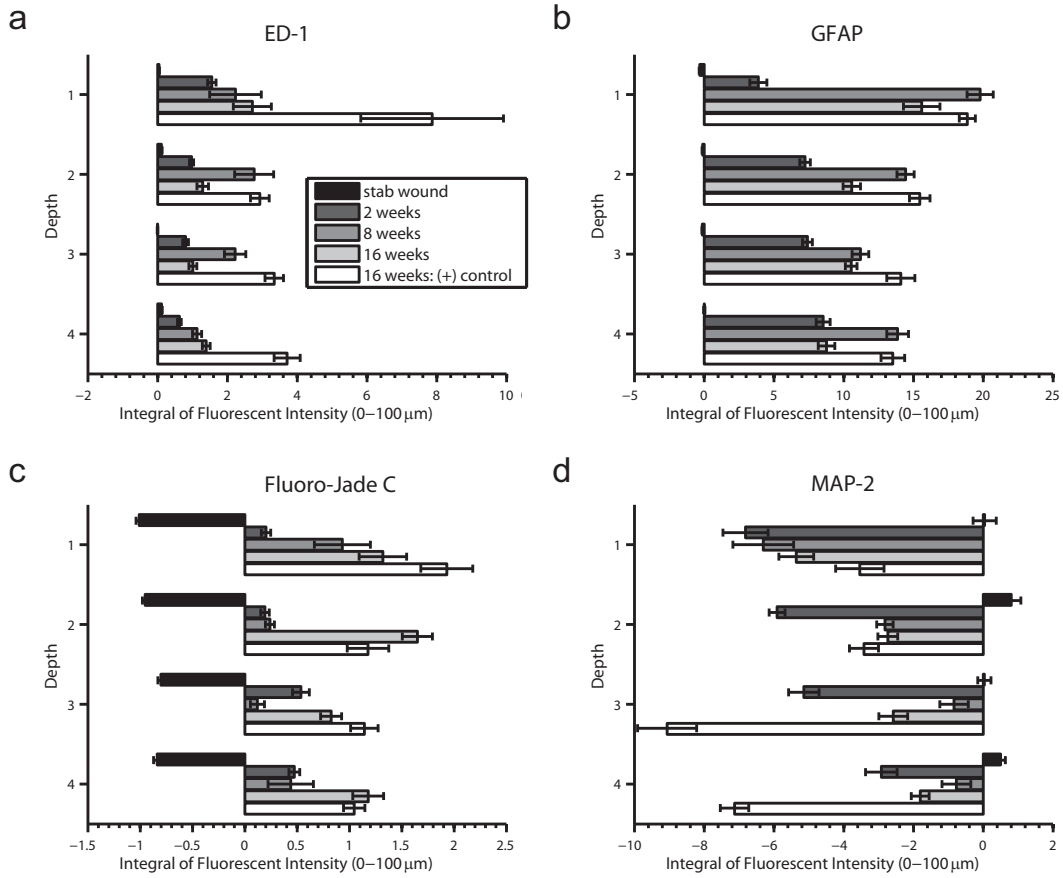

Figure 18: Quantified fluorescent intensity 0-100 μm from the electrode for (a) ED-1, (b) GFAP, (c) Fluoro-Jade C, and (d) MAP-2 for sections at the four different depths studied. On the y-axis, section 1 is $\sim$200 μm below the cortex, section 2 is $\sim$600 μm, 3 is $\sim$1000 μm, and section 4 is $\sim$1400 μm.

4.4.2.3 Anatomical markers of neurodegeneration: Axons (Tau-1, NF-200)

Unlike MAP-2, no differences were observed between conditions for the axonal markers Tau-1 and NF-200.

4.4.2.4 Molecular markers of neurodegeneration: Phospho-Tau (pT231)

A characteristic feature of many neurodegenerative diseases is axonal pathology manifested by hyperphosphorylation of protein Tau (see Table 1 of [78] for a list of neurodegenerative tauopathies). Given the association between oxidative stress and hyperphosphorylated Tau in neurodegenerative diseases such as Alzheimer's Disease (AD), several markers for hyperphosphorylated Tau were used. Tau protein, predominately located in axons, contains at least 30 epitopes which become abnormally phosphorylated in tauopathies like AD. There was no positive staining for Alz50 or AT8 (data not shown). PT231 staining was present only next to the electrode track, with negative controls showing an absence of staining. Within the first 50 μm from the electrode punctate staining was observed within neuron somas. Out to a distance of 700 μm from the electrode pT231 (+) dystrophic neurites and neuropil threads were observed, closely resembling those observed in an AD diseased human tissue section stained simultaneously (Figure 19).

While DBS electrodes are mainly stimulatory, they are an example of a chronically implanted electrode in humans. Human brain tissue was obtained from a patient implanted with a deep brain stimulation electrode, that had remained for 5 months. pT231 is upregulated in close proximity to the electrode (Figure 20a), but upregulated pT231 expression was not observed surrounding recording lead tracks used to locate the DBS electrode position (but not left in the brain) (Figure 20b).

4.5 Discussion

4.6 Discussion

While viability is a necessary condition for recordings, it is not sufficient. Not only must neurons be alive, they must also have normal network connectivity. In this study, we investigated neurodegeration surrounding chronically implanted electrodes at 2 weeks, 8 weeks, and 16 weeks after implantation. We varied the degree of

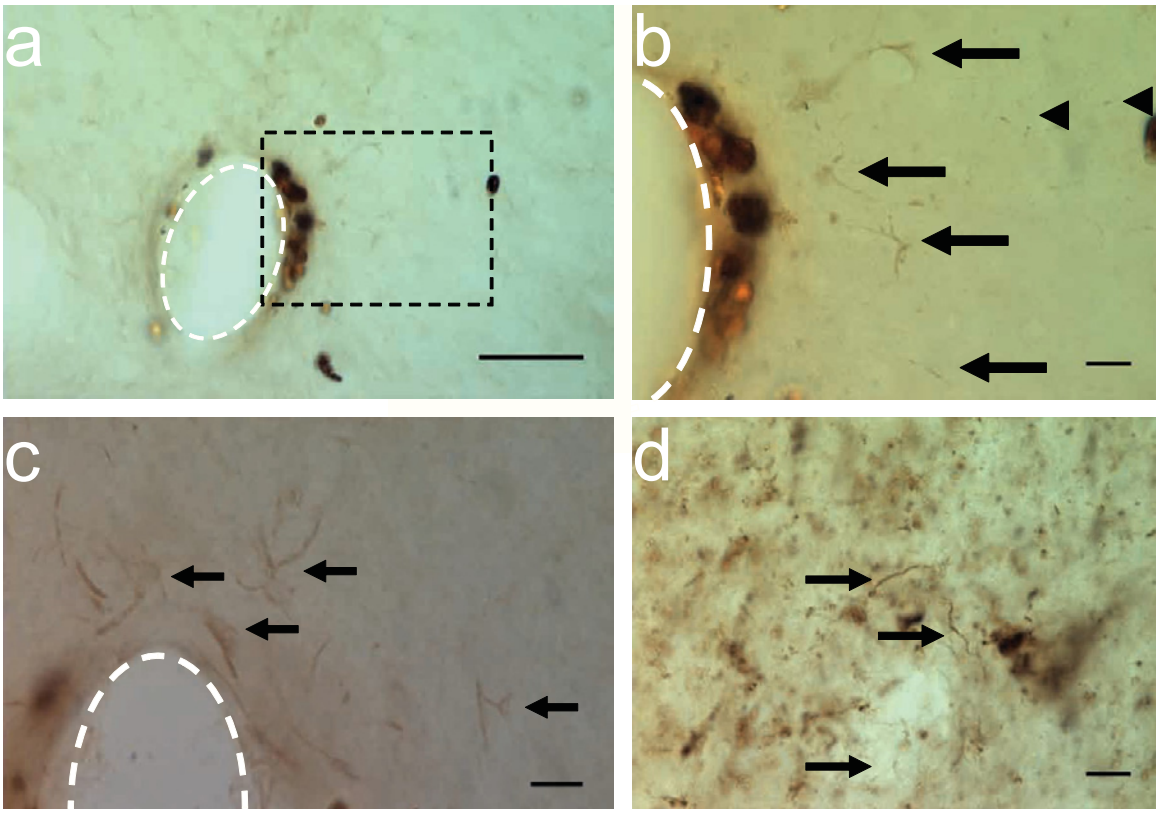

Figure 19: Hyperphosphorylated tau surround chronically implanted microelectrodes 16 weeks post implant. (a)-(c) Representative images of pT231 immunostained pretangles. (b) Boxed region in (a) at higher magnification. Note the increased presence of pT231 staining near non-specifically stained hemosiderin-laden macrophages. (c) Additional example from another implant showing pT231 positive signal surrounding electrode Arrows indicate labeled diffuse granular pretangles and arrow heads indicate rodlike dystrophic neurites. (d) Positive control- Human Alzheimer's case sections contained stained processes similar to those seen around electrodes. Scale bar = 50 μm (a) and 10 μm (b)-(d).

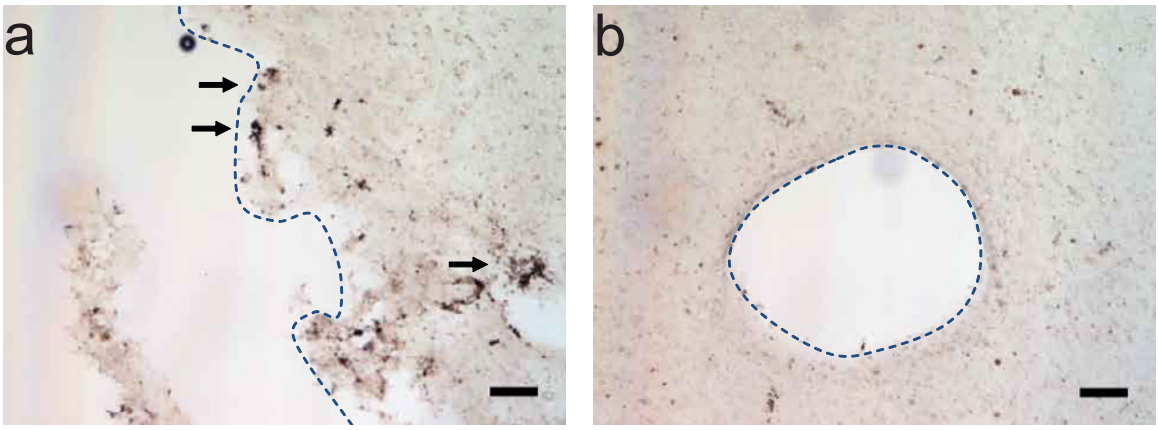

Figure 20: Hyperphosphorylated tau surround chronically implanted electrodes in human. (a) Deep brain stimulation electrode was implanted in a human Parkinson's Disease patient ∼five months after implant. Tissue adjacent to electrode track showed upregulated expression of pT231, an abnormally hyperphosphorylated site on the Tau protein. Arrows indicate regions of high pT231 expression. Scale bar = 100 μm (b) Electrode track from recording lead, a stab wound injury, did not show increased pT231 staining relative to background levels. Dashed blue lines outline the electrode track. Scale bar = 100 μm

chronic inflammation at the 16 week time point to test the hypothesis that chronic inflammation associated with the presence of the electrode is correlated with a neurodegenerative state. These data show that higher levels of activated microglia and reactive astrocytes are correlated with increased neuronal loss, dendritic loss, and tauopathy surrounding the electrodes. These data support an intriguing hypothesis for the inconsistency commonly observed with chronic neural recordings: that the glial scar causes recording failure indirectly through local neurodegeneration.

Edell et al. reported a 'kill zone' a distance of 10 μm away from the electrode [37]. Biran et al. reported neuronal death surrounding electrodes at chronic time points (2 and 4 weeks) [7]. This paper also showed loss in Neurofilament-160 within the first 100 μm from the electrode. The authors speculated that neurotoxic factors released by microglia best explain the neuronal loss. Our data show a progressive loss in number of neurons at chronic end points (increased loss at 16 weeks compared to 8 weeks). Furthermore, after 16 weeks there was greater neuronal loss in the case of

the 3mm_125 electrode design, associated with more inflammation, than in the case of the 4mm_200 electrode design. The NeuN loss we observed was ¿20% less than that reported by Biran et al. This may be explained by our use of an untethered model compared to a tethered model used by Biran et al., known to result in a larger inflammatory response [8].

To further study axonal and dendritic degeneration along with neuronal viability, we used FluoroJade C staining, a useful marker for neurodegeneration [18, 26, 39, 56]. Compared to its predecessors, Fluorojade B and Fluorojade, Fluoro-Jade C is brighter and stains degenerating neuronal processes in addition to the soma. We hypothesized that axonal and dendritic degeneration, would accompany neuronal death. The staining results revealed an early degeneration of neurons within 50 μm of the electrode at 1 hr and 24 hr post-implantation, but at 8 and 16 weeks post-implantation the marker revealed that degeneration is largely found in neuronal processes rather than in cell bodies. These data are consistent with a feature of neurodegenerative disease, that degeneration begins at the tip of the processes and works back toward the soma. Using immunohistochemistry, we further specifically labeled both dendrites (MAP-2) and axons (NF-200/Tau-1). We observed significant loss from 8 weeks to 16 weeks in dendrites, but no significant difference in axonal markers. Dendritic loss was most striking at deeper depths of the cortical column (Figure 21). Dendritic loss would be expected to have significant impact on processing of synaptic input and thus neural recordings.

No significant differences in NF-200/Tau-1 staining suggest that axons were spared, or may indicate axonal sprouting. We further investigated axonal state by looking for evidence of Tau pathology. Positive staining was found for the marker pT231 [63], but not AT8 or Alz50. It is well known that there is a temporal sequence of phosphorylation of Tau, with certain residues of the protein phosphorylated earlier than others. pT231 is one of the earliest sites of the Tau protein to be phosphorylated [3].

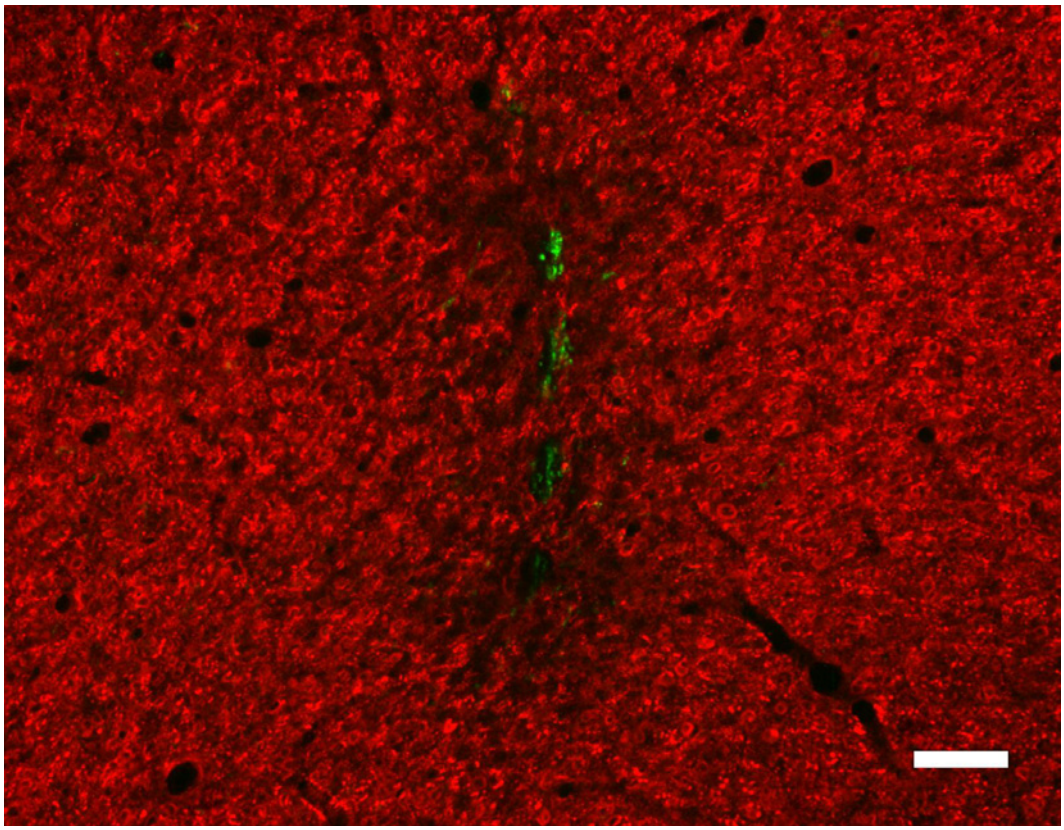

Figure 21: Merged Map-2 and ED-1 staining from consecutive sections. Section from 16 week (+) control condition at depth ∼1 mm below cortical surface. Scale bar = 100 μm.

T231 phosphorylation, occurring primarily in pre-tangles, precedes AT8, which occurs primarily in late stage extra-neuronal tangles [3]. It has also been shown that pT231 precedes Alz50 [89], and is therefore labeled as an early marker for Tau tangles [147]. Therefore, our observation of pT231 positive signal with an absence of AT8 and Alz50 positive signal, suggests that the Tau pathology present surrounding microelectrodes in this study after 16 weeks is in the early stages of Tau pathology. This is not to say, however, that there would not be functional consequences to pT231 alone. pT231 plays an important functional role in synaptic health [21, 81]. While paired helical filaments (PHFs), which are derived from hyperphosphorylation [2], are not apparent around electrodes after 16 weeks, pT231 precedes PHFs [144] and further studies are needed to investigate whether PHFs form >16 weeks.

The relationship between microglia and neurodegeneration has been an exciting topic of study in the neurodegenerative disease literature [11, 12, 82]. In one study, a single systemic injection of LPS caused chronic inflammation and progressive neurodegeneration. Other studies have investigated the relationship between inflammation and Tau hyperphosphorylation, with oxidative stress reported to cause Tau pathology [34, 95]. Kitazawa et al. showed that inflammation induced by LPS exacerbates Tau pathology [71]. Microglial activation has been shown to precede Tau tangles in a P301S tauopathy mouse model and can be diminished by non-steroidal anti-inflammatory drugs (NSAIDs) suggesting a causative role by inflammation in the formation of Tau tangles [160]. These studies are consistent with the human staining from this study, where pT231 expression was only present surrounding the DBS electrode, but not the stab wound injury caused by the recording lead, suggesting that chronic inflammation is necessary for hyperphosphorylation of Tau.

Hemosiderin-laden macrophages present suggest hemorrhaging of microvasculature in vicinity of the electrode. Hemosiderin is also present in the vicinity of DBS

electrodes, as reported recently in a postmortem study of a patient 71 months after implant [134]. The number of electrodes surrounded by hemosiderin-laden macrophages increased with time. The time course indicates that local hemorrhaging occurs not only from the acute injury, but at chronic time points as well. Vascular damage likely exacerbates the sustained activation of microglia next to the electrodes. Additionally, the effects of local ischemia at the electrode interface could be a cause of neurodegeneration. As mentioned previously, hemosiderin has been hypothesized as being a product of free radicals with ferritin [101], which suggests the local presence of reactive oxygen species (ROS) at the electrode. ROS are therefore a potential inflammatory mediator for the observed neurodegenerative features next to the electrode. Indeed, persistent thrombin signaling induces oxidative stress and has been shown to lead to Tau hyperphosphorylation and delayed neuronal death [136, 22]. In addition to ROS, the contribution of other pro-inflammatory mediators of inflammation, including cytokines and nitric oxide, should be considered as a mechanistic link(s) between chronic inflammation and local neurodegeneration in future studies.

The results of this study suggest that reducing inflammation through delivery of anti-inflammatory agents would be beneficial for chronic recordings, since the consequent neurodegeneration might also be slowed or halted. Experimental data suggest that target neurons for recordings must be within 100 μm [57]. We observed increased neuronal death, dendritic loss, and tau pathology within this critical region. Further studies are needed to determine the functional consequences of these neurodegenerative features on target neurons.

4.7 Acknowledgements

Funding support was provided by the NIH, R01 DC06849 (RVB) and NIH NS 045072 (RVB). GTEC, an NSF funded ERC located at Georgia Institute of Technology and Emory University (EEC-9731643), is also acknowledged for the use of core facilities.

CHAPTER V

CHRONIC INFLAMMATION SURROUNDING INTRA-CORTICAL MICROELECTRODES CAN BE INDIRECTLY MONITORED BY ELECTRICAL IMPEDANCE SPECTROSCOPY

5.1 Abstract

The widespread usefulness of neural prosthetic devices is currently hindered by the inability to reliably record neural signals from chronically implanted electrodes. The extent to which the local tissue response influences recording failure is not well understood. Impedance spectroscopy has shown promise for use as a non-invasive tool to estimate the local tissue response to microelectrodes. We describe modeling results of impedance spectra from chronically implanted rats using the well-established Cole model, and results of a correlation analysis of modeled parameters with histological markers of astroglial scar. Correlations between modeled parameters and histology were significant for only two independent parameters studied and in both cases were confined to the first 50 μm from the interface. These parameters were: 1) the Py value, a parameter previously shown to be highly correlated with cell volume fraction in cell suspensions (GFAP: $r = 0.85$, $p < 0.01$; DAPI: $r = 0.92$, $p < 0.01$) and 2) the characteristic frequency, (f_c), the frequency at which the reactive component is maximal (GFAP: $r = -0.87$, $p < 0.01$; DAPI: $r = -0.71$, $p < 0.05$). Our experimental results, along with computer simulations, suggest that reactive astrocytes are the predominant cellular player affecting electrical impedance spectra. The results also suggest that the largest contribution from reactive astrocytes on impedance spectra

occurs in the first 50 μm from the interface. These results form the basis for future approaches where impedance spectroscopy can be used to evaluate neural implants or related strategies aimed at minimizing the astroglial scar.

5.2 Introduction

Neural prosthetics is a burgeoning field with clinical applications in the treatment of spinal cord injuries, Amyotrophic Lateral Sclerosis (ALS), and other debilitating diseases/injuries [60, 124]. However, the widespread usefulness of neural prosthetics is currently hindered by the inability to reliably record neural signals for durations beyond several months. To assess the contribution of local tissue response to chronic recording failure, there is an urgent need to develop tools to non-invasively determine the extent of local tissue response surrounding microelectrodes.

The time course of the tissue response to microelectrodes is well defined, and culminates in the formation of a glial scar, composed primarily of reactive astrocytes [110, 142, 139, 7, 8]. The gold standard for determining the degree of tissue reaction surrounding microelectrodes is histology. Gross histological stains, such as Hematoxylin & Eosin, have been complemented by the advancement of immunohistochemical methods to allow the visualization of specific proteins. The disadvantages of these methods are 1) an inability to follow the tissue reaction time course in a living animal, 2) the large amount of time and labor required for histological work, and 3) the qualitative nature of assessment. Establishing a quantitative, non-destructive method to assess the degree of tissue reaction surrounding microelectrodes would expedite study of the influence of tissue reaction on the reliability of microelectrode recordings. Furthermore, such a technique would be invaluable for evaluating the efficacy of novel strategies to improve chronic recording reliability.

The biophysics of the passive electrical properties of heterogeneous material, including biological tissue, has been intensely studied for over 60 years [23, 24]. The

complex permittivity of biological tissue is known to vary as a function of frequency [33, 123]. In the 10 kHz to 10 MHz frequency range, the electric field penetrates across cellular membranes in biological tissue. This frequency range, called the β dispersion, is useful in predicting changes in the structure of biological tissue [50].

While the magnitude of the impedance at 1 kHz is a common measure for assessing the performance of chronic electrodes, measuring impedance at multiple frequencies has several advantages due to the ability to then model the impedance spectra. The advantages of multiple frequencies over one frequency has been an area of contention in the field of body impedance analysis (BIA), however, modeling of multiple frequencies using the Cole model results in more accurate predictions of total body water [27, 33].

Pioneering work by Williams et al. showed that impedance spectra from chronic microelectrodes display a characteristic feature for tissue reaction when plotted in the complex plane [151]. Implants surrounded by severe tissue reactions, as assessed using DAPI and GFAP, showed a more pronounced circular arc in the complex plane. This circular arc locus in the complex plane is not, however, unique to chronic microelectrodes in the brain. Indeed, it occurs in impedance measurements of all biological tissues [50]. The characteristic semicircle with the center depressed below the real axis is empirically expressed in the Cole equation [23]:

$$Z = R_\infty + \frac{\Delta R}{1 + (j\omega\tau_c)^\alpha}, \tag{1}$$

where $\Delta R = R_o - R_\infty$ and $\tau_c = 1/\omega_c = 1/(2\pi f_c)$. In (1), Z is complex impedance at frequency ω and $j = \sqrt{-1}$. The impedance circular arc locus is fully defined by four independent variables: R_o: resistance at zero frequency, R_∞: resistance at infinite frequency, α: the angle of depression ranging between 0 and 1, and f_c: the characteristic frequency, which defines the frequency scale. Because of the advantages of bioimpedance modeling over measurement of a single frequency such as 1 kHz, along

with the wide use of the Cole model to relate impedance spectroscopy with tissue structure [87, 10, 94, 103, 17, 50, 33], we chose to study the usefulness of Cole model parameters for estimating the tissue response to chronic microelectrode arrays. An index derived from the Cole model parameters R_o and R_∞, the Py value, was also investigated. The Py value represents the normalized extent of the β dispersion and has been shown to be highly correlated with cell volume fraction in cell suspensions [109]. Cell volume fraction is the ratio of intracellular volume to total tissue volume (both intracellular and extracellular volume combined). Since astrocyte proliferation and hypertrophy are known to occur in the glial scar, both of which affect cell volume fraction, we hypothesized that Py might be correlated with these changes.

In this study, we present our work on the application of bioimpedance modeling for the estimation of the tissue response to chronic microelectrodes. Correlation results of modeling parameters with histology, show that two independent parameters, Py and f_c, are well correlated with reactive astrocytes in the first 50 μm surrounding microelectrodes.

5.3 Materials and Methods

5.3.1 Surgical procedures for chronic implants

Four adult male Sprague-Dawley rats (275-299 grams) were implanted with stainless steel microwires, 200 μm in diameter and 300-500 kΩ impedance at 1 kHz, insulated with Epoxylite (FHC, Inc.). All implanted materials were sterilized using ethylene oxide at least 48 hrs prior to surgeries. Rats were anesthetized for 5 min with a mixture of 5% isoflurane and 1 L/min prior to surgery. Each rat was positioned into a stereotactic frame (Kopf), where anesthesia was maintained to effect (1-3% isoflurane and 0.3 L/min) during surgery by monitoring the rat's breathing. The rat's head was shaven over the incision area and the skin was disinfected with isopropyl alcohol and chlorohexaderm using a slight scrubbing motion prior to making the incision.

Ophthalmic ointment was applied to the eyes to prevent drying. A midline incision was made along the scalp, the skin retracted, and the periosteum cleared to expose the Bregma. Five stainless steel skull screws were inserted (dimensions = 0-80x(1/16); Plastics One, Inc.). One skull screw (0 mm lateral and ∼2 mm posterior to the Lambda) was wrapped with fine metal wire soldered to a Molex connector to serve as the counter electrode during impedance measurements. A dental drill was used to create a 3.2 mm hole at 0.2 mm anterior and 3.0 mm lateral to the Bregma with a custom trephine (24 tooth 3 mm O.D.) fabricated from stainless steel tubing (Small Parts). In order to minimize iatrogenic damage, room temperature saline was applied liberally to the spinning drill bit at the bone interface. The bone plug was carefully removed and, with the aid of a surgical scope, the dura was gently pierced using a 28 gauge needle with the tip bent at a 45°angle, cut using dura scissors, and then reflected back over the skull. Two electrodes were implanted, one in each hemisphere, of the motor cortex region (3 mm lateral and 0.2 mm anterior to the Bregma). The microwires were implanted ∼1 mm below the surface of the cortex using a stereotaxic apparatus at a rate of ∼0.1 mm/sec. After 5 minutes, during which the brain surface was kept moist with saline, the craniotomy was covered with 1% SeaKem Agarose (Cambrex) gel in phosphate buffered saline (PBS). The craniotomies were further sealed and protected using dental acrylic, which was anchored to the skull by the bone screws. All implants were performed by the same surgeon. All procedures were approved by Georgia Tech Institutional Animal Care and Use Committee.

5.3.2 Impedance analysis: Impedance spectroscopy measurement

After 11 weeks, a time point long after the electrical properties of the astroglial scar have stabilized, the electrical impedance spectra of the electrode-tissue interface were measured. A constant voltage AC 10 mV signal was applied to the microelectrode, and impedance magnitude and phase were measured twice at a counter electrode

(stainless steel skull screw), located at a fixed distance away, from 100 Hz to 1 MHz using a logarithmic sweep of 40 points, and additionally at 1 kHz. Constant voltage, as opposed to constant current, was used to minimize the contribution of parasitic impedance, in parallel with the electrode-tissue impedance. The measurement setup consisted of a lock-in amplifier (Signal Recovery Model 7280), along with a current-to-voltage converter (Figure 22). For the current-to-voltage converter, a high-speed op-amp, AD829 (Analog Devices), was chosen for its high gain bandwidth product (GBWP) of 120 MHz. Impedance magnitude and phase were calculated using the voltage measured at input A and at input B. Both inputs could not be read simultaneously, so two sweeps were made sequentially, one for input A and one for input B. The tissue properties were assumed to be stable over the course of the measurement, which is reasonable given that each sweep took ∼30 sec to complete, and sweeps were made consecutively. Additional impedance sweeps were made after the removal of the electrode in PBS in order to test the electrical properties of the electrode alone.

5.3.3 Impedance analysis: Estimation of Cole parameters and Py from impedance spectra

Data points from the complex impedance locus plot, with the real part of the impedance versus the negative imaginary part of the impedance, were selected to optimally fit to a circle using least squares minimization [44]. The best-fit curves all had a goodness-of-fit of $r > 0.99$, and impedance from a minimum of 10 frequencies were modeled. The zero-intercepts of the curves were then calculated (R_o and R_∞). From these two parameters, Py was calculated using the formula $(R_o - R_\infty)/R_o$ (see Figure 23a).The characteristic frequency, f_c, and parameter α were calculated using the "$ln(u/v)$" method [123, 146] (see Figure 23b and Figure 23c).

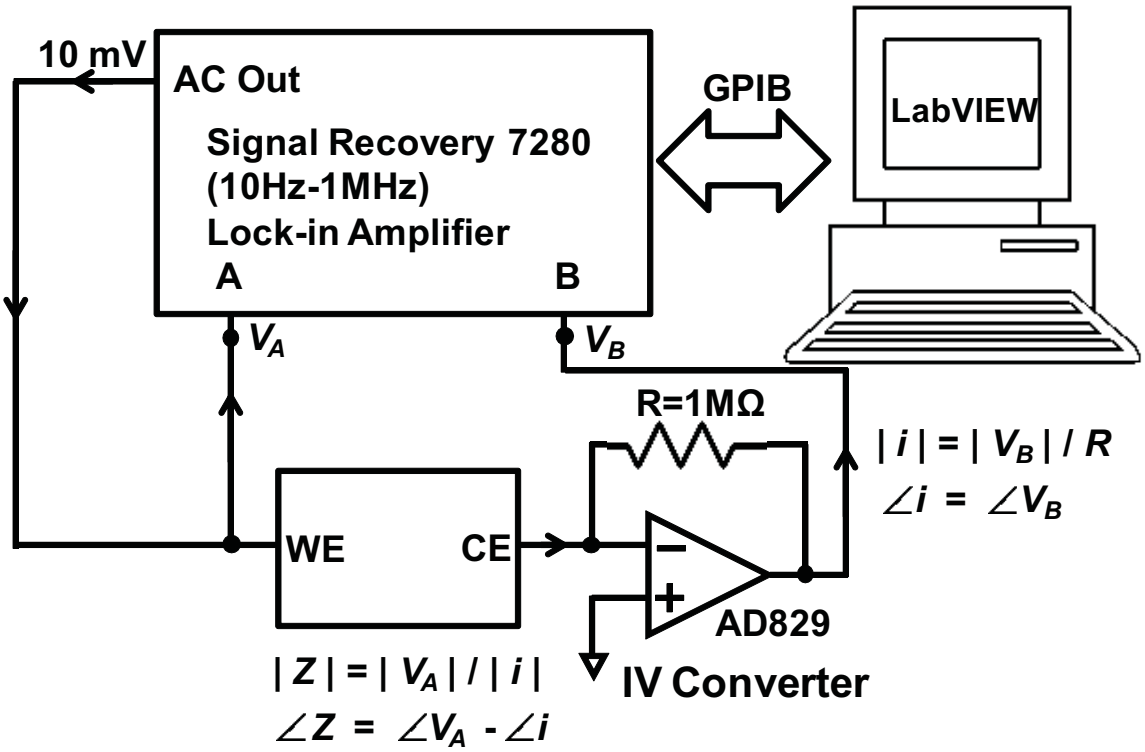

Figure 22: Schematic showing the setup used to measure electrical impedance spectra. The setup consists of a lock-in amplifier with a constant voltage output of 10 mV connected to the working electrode (WE) and measured at input A. The counter electrode (CE) is connected to an current-to-voltage converter and the voltage measured at input B. Physically, WE = microwire and CE = skull screw.

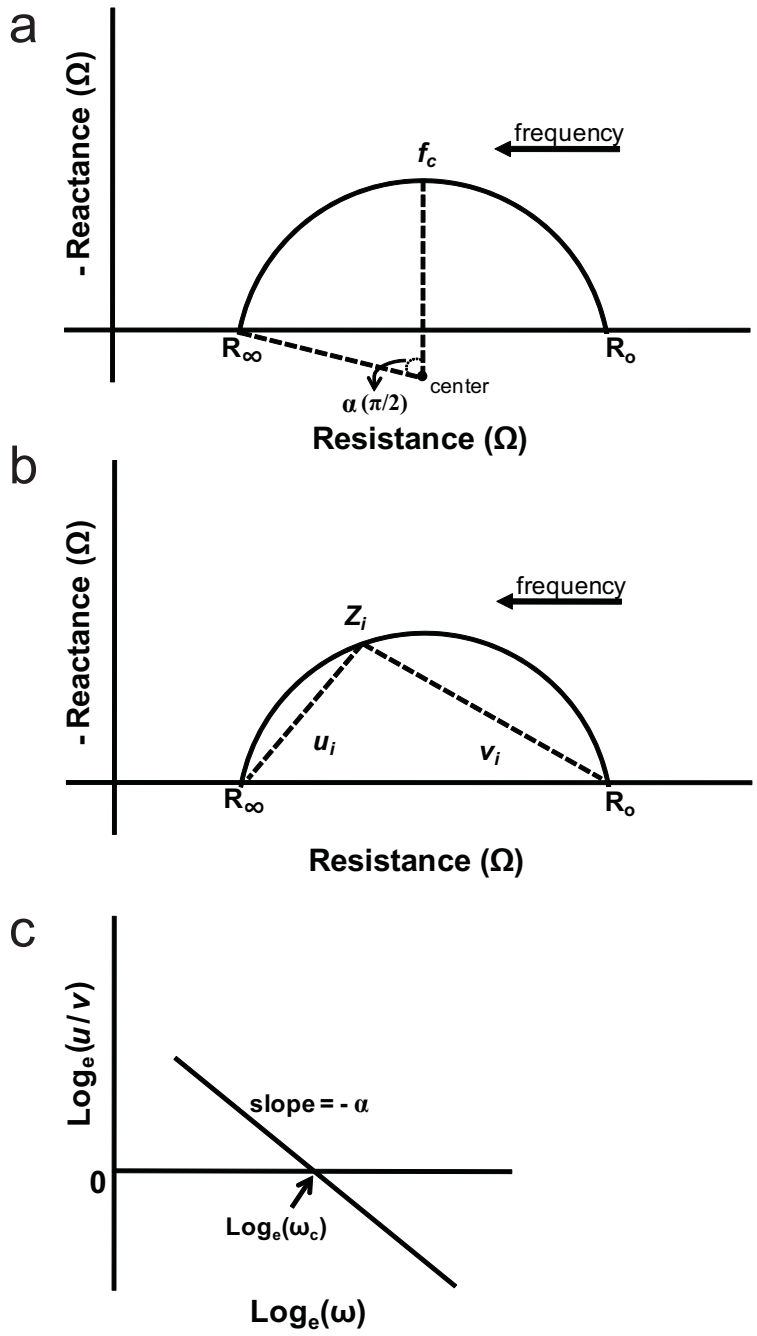

Figure 23: (a) Theoretical impedance spectra of biological tissue showing the Cole model parameters. The four Cole model parameters can be estimated geometrically from the impedance loci plot to characterize the impedance spectra. R_o and R_∞ are the resistances at zero and infinite frequency, respectively; f_c, characteristic frequency, is the frequency at which the reactive component of impedance is maximal; α is the angle of depression of the center of the circle below the real axis. (b)-(c) Calculation of the Cole model parameters f_c and α. (b) The chord lengths, u_i and v_i, are calculated at each complex impedance value, Z_i. (c) Theoretical plot showing the relationship between chord lengths and the Cole parameters f_c, where $f_c = 2\pi/\omega_c$, and α.

5.3.4 Tissue analysis: Brain tissue preparation for immunohistochemistry

Rats were perfused transcardially with 200 ml of PBS, followed by 200 ml of 4% paraformaldehyde in PBS ∼12 hrs after impedance spectroscopy measurement. The acrylic headcap, attached to the skull, along with the electrodes were carefully removed and stored in PBS at 4 ℃. The brain was then extracted and left in 4% paraformaldehyde solution overnight at 4 ℃. Brains were then transferred to PBS for 1 hr at 4 ℃, followed by 30% sucrose until they had sunk to the bottom (∼2-3 days). Brains were then cryoembedded using OCT compound, cryosectioned to a thickness of 30 μm, and stored sequentially to preserve cortical depth information.

5.3.5 Tissue analysis: Immunohistochemistry

Cell density and cell hypertrophy strongly influence the electrical impedance properties of tissue within the β dispersion frequency band, due to their relationship with cell volume fraction [43]. Therefore, GFAP expression, which is upregulated in response to injury, was used to estimate astrocyte hypertrophy. DAPI, which stains all cell nuclei, was used to estimate cell density.

Tissue sections were incubated in blocking solution, consisting of 4% goat serum in PBS, for 1 hr at room temperature. Sections were then incubated in primary solution, GFAP (DAKO, 1:2000) in blocking solution, overnight at 4 ℃. Following three rinses in PBS, sections were incubated in secondary solution, Alexa 488 IgG anti-rabbit (Molecular Probes, 1:220), for 1 hr at room temperature. After three rinses, sections were counterstained with DAPI (Invitrogen), mounted to slides and coverslipped using Fluoromount G.

5.3.6 Tissue analysis: Quantitative analysis of histological images

Fluorescent images were captured using a Microfire digital camera attached to a Zeiss Axioscop2 Plus upright microscope. Images were quantified using a custom program

written in MATLAB (Mathworks) [93]. Briefly, the recording track was outlined using GFAP-labeled images, and an ellipse was constructed to delineate the border between the electrode track and the surrounding tissue. Rectangular regions were drawn 500 μm away from the border on both the left and right sides of the electrode track, with the width of the quantified region approximately equal to the diameter of the electrode track.

5.3.7 Computer modeling

Computer simulations were constructed using software previously developed for the study of the relationship between tissue structure and its passive electrical impedance properties (Bioimpedance Simulator; source files are available at `http://www.cnm.es/~mtrans/BioZsim/`). This software generates electrical circuit equations analyzed using SPICE from a 2D map, representing a slice of living tissue. Each pixel of the 2D map represents electrode, extracellular medium, or intracellular medium, and is modeled with pure resistors. At intracellular-extracellular medium interfaces, a cell membrane is modeled as a capacitance and resistance in parallel. Simulation parameters used were: 30 x 30 pixels, slice thickness = 50 μm, pixel size = 5 μm, membrane capacitance = 1 μF cm^2, intracellular medium resistivity = extracellular medium resistivity = 100 Ω cm, electrode resistivity = 0.01 Ω cm, frequency range = 100 Hz - 1 MHz.

5.3.8 Statistical analysis

Correlations were tested using Pearson's correlation coefficient and the significance was tested using Student's t-test. For all tests, $p < 0.05$ was considered significant.

5.4 Results

5.4.1 Qualitative observations of the tissue response

There was a large variation in the tissue responses to the microwires. These ranged from a tight network of astrocytes only a few cell layers in thickness (Figure 24a) to reactions extending several hundred μm from the electrode (Figure 24b). Similarly, there was a large variation in cellular density as indicated by DAPI staining.

5.4.2 In vivo impedance spectroscopy

In order to minimize the contribution of electrode polarization on the measurement at low frequencies, the impedance contribution of the electrodes should be small in comparison to the biological component in a two-electrode measurement system. Impedance measurements in saline after removal of the electrodes from the brain, demonstrated that the electrode contribution was small in comparison with the tissue at frequencies fitted with the Cole model.

Figure 24c shows sample impedance spectra from two different electrodes corresponding to the reactions imaged in Figure 24a and Figure 24b. More extensive tissue reactions were associated with a more pronounced circular arc in the loci plots.

5.4.3 Quantitative correlation of impedance parameters with histology

Table 5 presents the correlations of Py with the total intensity of GFAP and DAPI labeled images for incremental radial distances away from the electrodes. This table shows that the data are significantly correlated only in the immediate vicinity of the electrode (0-50 μm from the interface) (see Figure 25a).

Table 5 also includes the correlations of the characteristic frequency, f_c, with the total pixel intensity of GFAP and DAPI labeled images for incremental radial distances away from the electrodes. This table shows that, as with the Py value, the data are significantly correlated only in the immediate vicinity of the electrode (0-50 μm from the interface) (see Figure 25b). No correlations were noted with histology

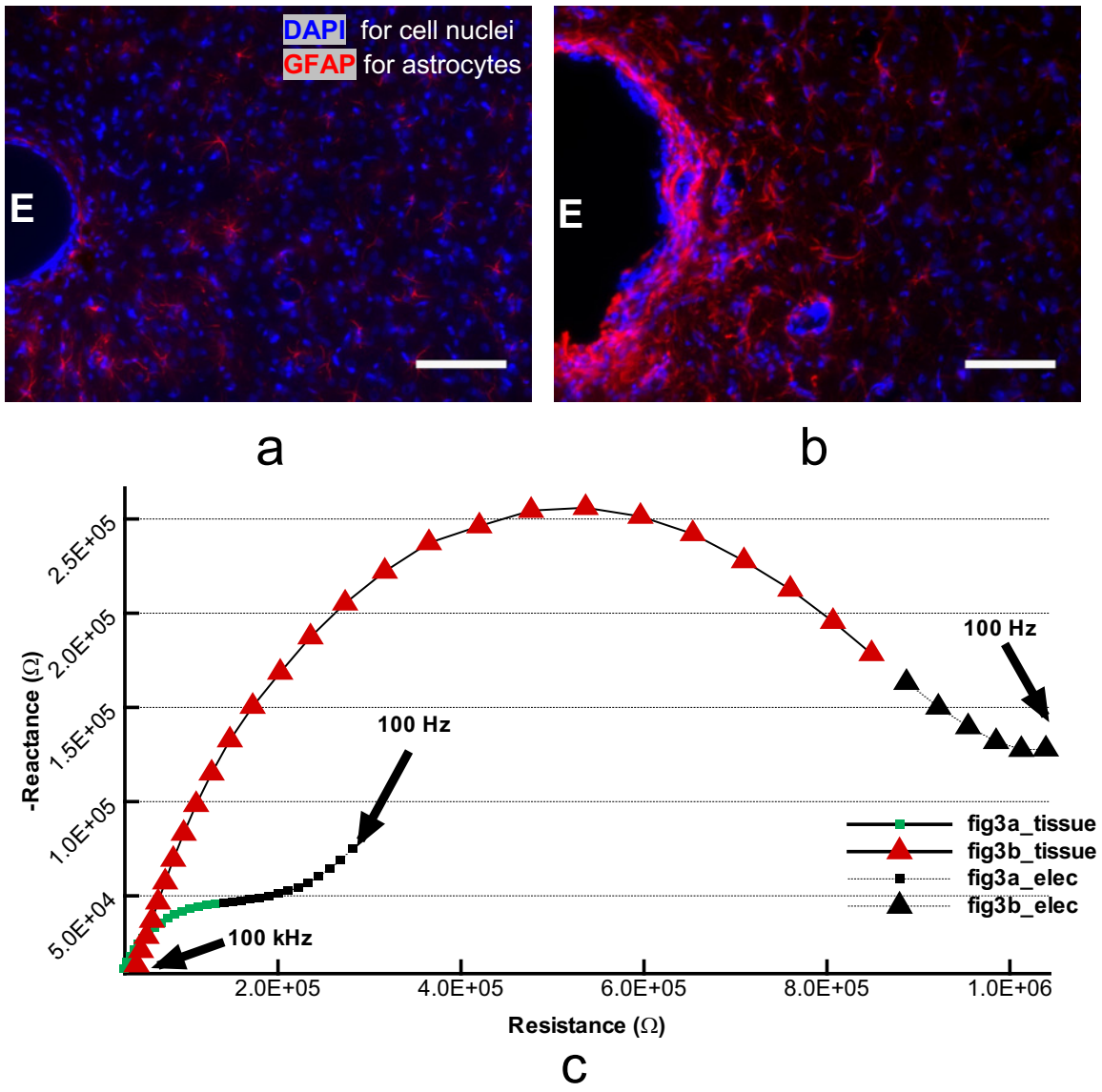

Figure 24: Example immunostained sections showing a (a) mild and (b) severe tissue response. (c) The corresponding impedance spectra show that severe reactions result in broader circular arc loci. (a)-(b) 'E's indicate the locations of the electrode tracks. Scale bar = 100 μm. (c) Green squares correspond to electrode in (a), with $Py = 0.9911$ and $f_c = 845$ Hz. Red triangles correspond to electrode in (b), with $Py = 0.9422$ and $f_c = 2819.3$ Hz. Black filled points were not included in Cole model, since at these lower frequencies electrode impedance decreased the goodness-of-fit to the Cole model due to electrode polarization.

Table 5: Results of Pearson's correlation between independent model parameters Py and f_c with GFAP intensity and DAPI intensity as a function of distance away from the microelectrode. Immunostaining of sections with the primary antibody omitted were not significantly correlated with Py or f_c at any distance, suggesting that the significant correlation between Py and f_c with GFAP at 0-50 μm away from the electrode is not due to non-specific binding. Bold text indicates conditions at which the Pearson's correlation was significant ($p < 0.05$).

Distance from Interface (μm)	Astrogliosis (GFAP)		Cell Nuclei (DAPI)		2°Antibody Only	
	Pearson's coefficient (r)	p-value	Pearson's coefficient (r)	p-value	Pearson's coefficient (r)	p-value
0-50^{Py}	**0.85131**	**0.00733**	**0.91805**	**0.00129**	0.26299	0.52916
0-50^{Fc}	**−0.8665**	**0.0054**	**−0.7111**	**0.048**	−0.2146	0.6098
50-100^{Py}	0.67771	0.064766	0.63465	0.09095	−0.56756	0.14227
50-100^{Fc}	−0.5497	0.1582	−0.2099	0.6179	0.4561	0.2561
0-100^{Py}	**0.83086**	**0.01062**	**0.86273**	**0.00582**	−0.03516	0.93412
0-100^{Fc}	**−0.7876**	**0.0203**	**−0.5428**	**0.1645**	0.0259	0.9514
100-200^{Py}	0.47008	0.23983	0.46	0.25145	−0.30123	0.5173
100-200^{Fc}	−0.3796	0.3537	−0.299	0.4719	0.6313	0.0932
200-300^{Py}	0.36199	0.37822	0.44631	0.26766	−0.35478	0.4815
200-300^{Fc}	−0.3558	0.387	−0.3033	0.4652	0.5845	0.1281
300-500^{Py}	0.30648	0.46032	0.26334	0.52859	−0.46245	0.2486
300-500^{Fc}	−0.3689	0.3685	−0.0909	0.8305	0.4809	0.2277
0-500^{Py}	0.70565	0.050509	0.58464	0.12798	−0.53081	0.17588
0-500^{Fc}	−0.6619	0.0738	−0.3495	0.3961	0.4775	0.2315

^{Py} Correlation with Py.
^{Fc} Correlation with f_c.

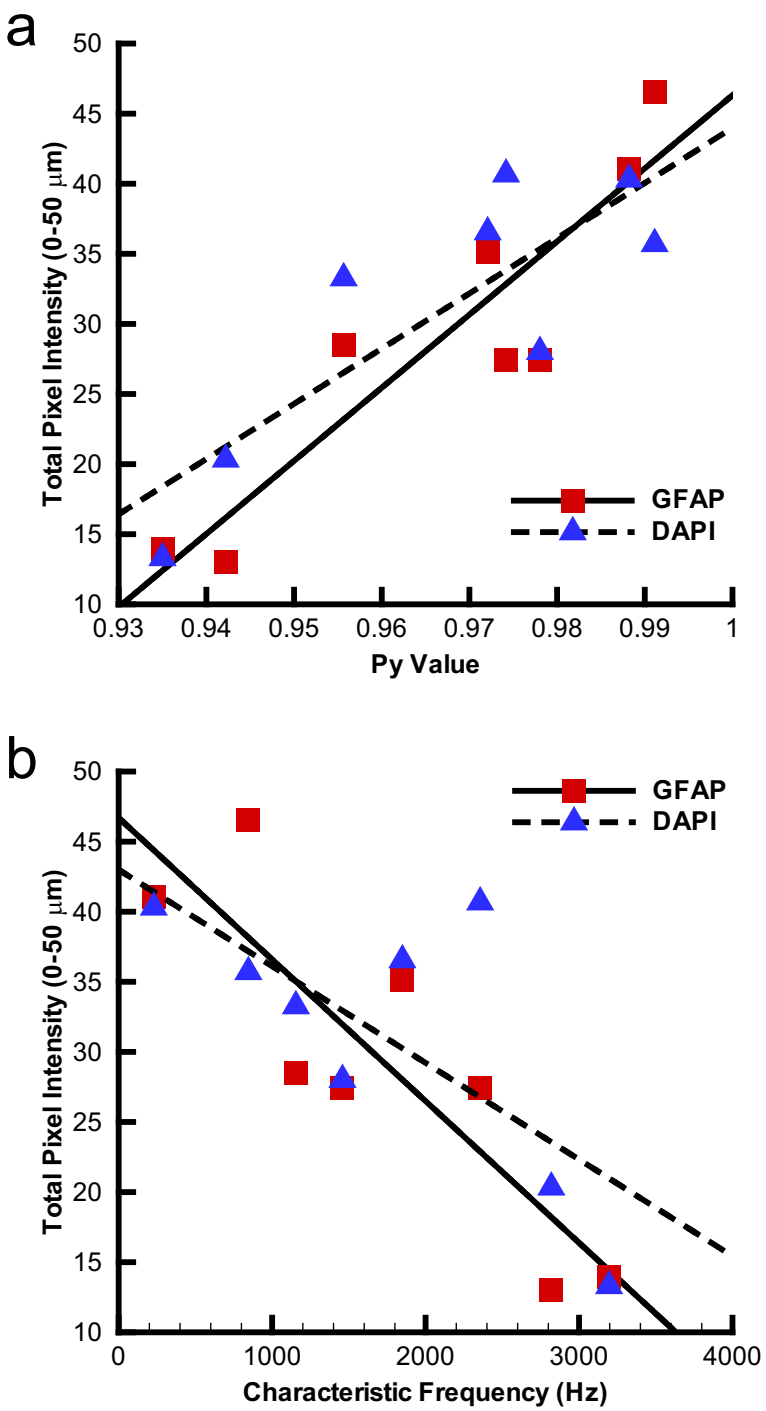

Figure 25: (a) Scatter plot of Py versus GFAP pixel intensity and Py versus DAPI pixel intensity 0-50 μm from the tissue-electrode interface. Black lines show the linear regression for GFAP (solid; $r = 0.85$) and DAPI (dashed; $r = 0.92$). (b) Scatter plot of f_c versus GFAP pixel intensity and f_c versus DAPI pixel intensity 0-50 μm from the tissue-electrode interface. Black lines show the linear regression for GFAP (solid; r = -0.87) and DAPI (dashed; r = -0.71).

for R_o, R_∞, α, or $|Z|_{1kHz}$ at any distance away from the electrode up to 500 μm (data not shown).

5.4.4 Computer modeling

To provide further insight into the mechanisms of cell density and cell hypertrophy on impedance spectra, computer simulations were carried out. Figure 26 shows the constructed modeled tissue slices with corresponding impedance spectra for increasing cell density (a)-(d) and cell hypertrophy (e)-(h). These simulations show that an increase in cell volume fraction, occurring as a result of either increased cell density or cell hypertrophy, produces an increase in the Py value and characteristic frequency, f_c, in the resulting impedance spectra (see Table 6).

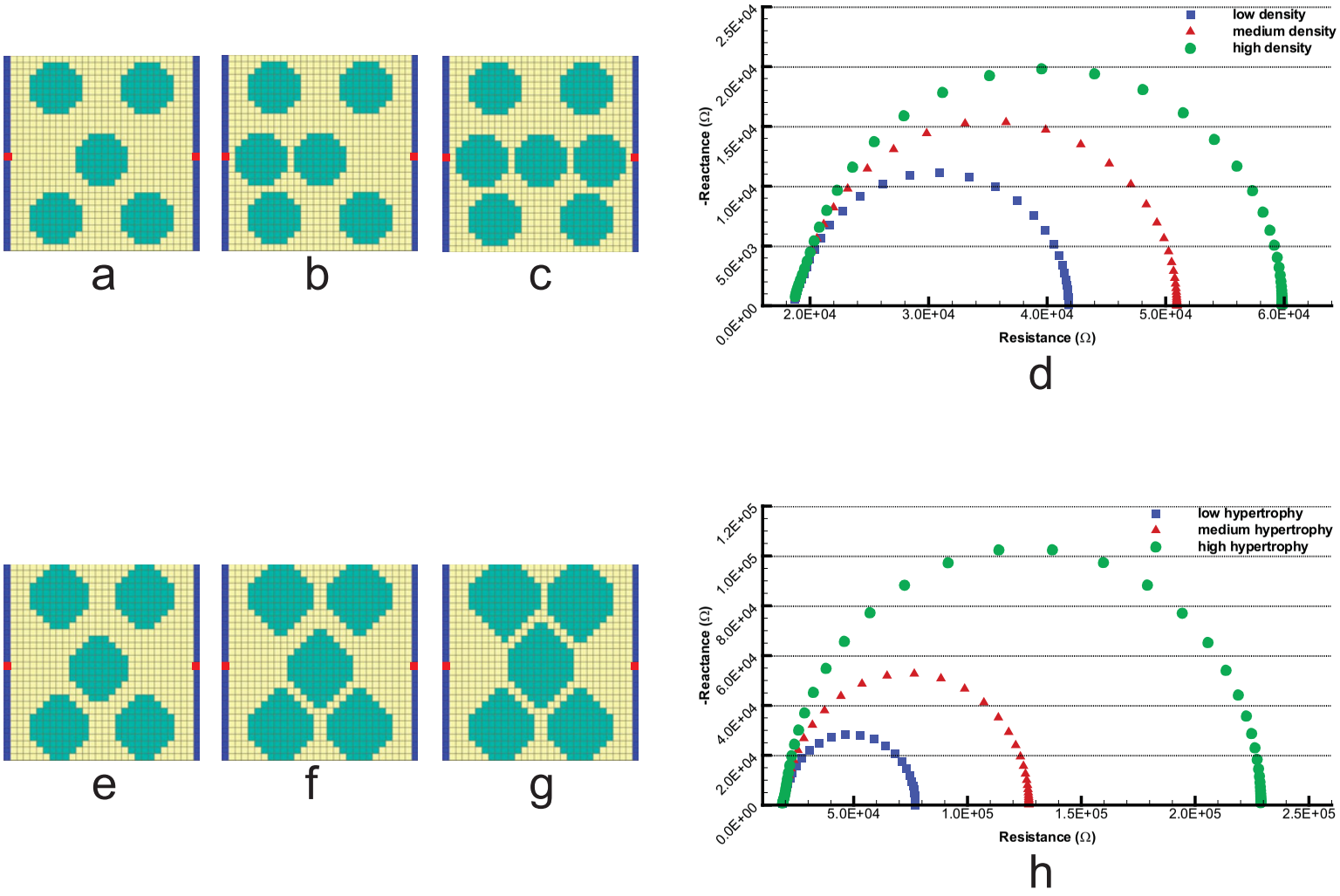

Figure 26: Computer simulations demonstrate the effect of an increase in cell density (low (a) medium (b), and high (c)) and the effect of an increase in cell hypertrophy (low (e), medium (f), and high (g)) on impedance spectra ((d) and (h) respectively). (a)-(f) Green pixels indicate the intracellular medium, yellow pixels indicate the extracellular medium, and blue pixels indicate the electrode. The electrical impedance is calculated between the two red pixels. The simulated impedance data were characterized using the same methods used for experimental data (see Table 6).

Table 6: Results of Cole model parameters, Py, and impedance magnitude at 1 kHz ($|Z|_{1kHz}$) for computer simulated data with varying cell density and cell hypertrophy (see Figure 26). An increase in cell volume fraction due to increasing either cell density or cell hypertrophy results in an increase in complex impedance, particularly at low frequencies. The parameters most sensitive to changes in cell density and cell hypertrophy are R_o, $|Z|_{1kHz}$, f_c, and Py, while R_∞ and α show slighter changes.

		Cole Model Parameters					
		R_o	R_∞	f_c	α	Py	$\|Z\|_{1kHz}$
Cell density	low	41854	18960	179750	0.9307	0.547	41811
	medium	51006	19033	149690	0.9308	0.627	50939
	high	59901	19144	136580	0.9389	0.680	59823
Cell hypertrophy	low	77272	19241	82098	0.9497	0.751	77164
	medium	127160	19510	47394	0.9500	0.847	126930
	high	229270	19813	25232	0.9466	0.914	228680

5.5 Discussion

In this study we present data supporting the use of impedance spectroscopy to non-invasively quantify cellular concentration in the immediate vicinity of the electrode. The predominant cell type was identified to be astrocytes using immunohistochemistry. Impedance spectroscopy was used to monitor chronically-implanted microwire electrodes and two independent parameters, Py and f_c, of the well-established Cole model were found to strongly correlate with cellular density and GFAP expression. Modeling studies show that not only cell density, but astrocyte hypertrophy as well, has a large influence on the impedance spectra, and the Py and f_c parameters in particular.

It is likely that astrocytes are the largest cellular contributor to the electrode impedance locus, because of the tight interstitial spaces that these cells form within the astroglial scar, which entirely encapsulates the electrode. The astroglial scar restricts the flow of current through the extracellular space, since cell membranes impede current flow at low frequencies. Several studies have investigated the diffusion

properties of the extracellular space in the CNS, and in astroglial scar there is an increase in tortuosity [114, 137, 138]. Our results corroborate previously reported correlations between impedance spectroscopy and histology [151]. Particularly, our results show along with Williams et al. that more reactive response to microelectrodes result in a more pronounced circular arc in the impedance spectra. In this paper, we additionally characterize the circular arc in the impedance spectra using well-established modeling methods in the bioimpedance literature. This then, along with quantitative histology, allowed us to investigate which features of the impedance spectra best correlate with the tissue response.

Traditionally, the impedance magnitude measured at 1 kHz has been used as an estimate of chronic recording electrode performance [88, 96, 143]. Our observation of no correlation between impedance magnitude at 1 kHz and GFAP or DAPI (data not shown) can best be explained by variation in the electrode impedances. Using a two-electrode impedance measurement configuration, electrode polarization is measured in addition to the surrounding tissue. The effect of electrode polarization on impedance measurements is significant up to 1 kHz [97]. These results, therefore, illustrate an advantage of a multiple frequency modeled approach over a measurement at a single frequency such as 1 kHz, since the model is based on higher frequency measurements where the effect of electrode polarization is greatly decreased. The normalization in the calculation of Py eliminates the electrode cell constant, which is dependent on electrode geometry, giving a relative index for estimating cell volume fraction across multiple electrodes. In a previous study using the Utah electrode array, SNR and $|Z|_{1kHz}$ were negatively correlated within each rat, but not across rats [135]. One potential explanation for the lack of correlation across animals is impedance differences in the electrodes themselves and not the surrounding tissue. Impedance measurement at multiple frequencies across a wide frequency range is necessary to separate the impedance contribution of the electrode alone from that of the

surrounding tissue.

The frequency at which the impedance reactance is maximal, f_c, has been cited as being more stable than either the complex or real impedance values alone [10, 94, 103]. Cole parameters have previously been used to characterize ischemia [17]. In this study, R_o and f_c were the two parameters that best characterized ischemia.

A disadvantage of any two-electrode measurement system is that the contribution of the electrode impedance may be larger than the contribution of the tissue impedance at low frequencies (<1 kHz). Future systems using three- or four-electrode designs to minimize or eliminate the contribution of electrode polarization from the measurement may open the possibility for simpler measurements such as $|Z|_{1kHz}$ and R_o to be useful parameters for predicting tissue response. Without the influence of electrode polarization, simulations suggest that these parameters are correlated with cell density and hypertrophy (Figure 6). R_∞ changes little, since the resistance at high frequencies is independent of cell membranes and intra- and extra-cellular resistances are comparable. The disadvantage of the three- and four-electrode measurement setups are the increased complexity of the measurement procedure and calculations.

The modeled parameters Py and f_c were only correlated with astroglial scar immediately adjacent to the microelectrode (up to 50 μm away), shedding light on the spatial resolution for this application of bioimpedance spectroscopy. This suggests that the bulk of the impedance measured is due to tissue in this region. Earlier reports of the tissue response to microelectrodes identified astroglial scar as spanning 50-100 μm away from the electrode-tissue interface [25, 54, 93, 122, 128, 142], consistent with our findings. This experimental data validates earlier finite element modeling studies that predicted the contribution of impedance to be 90% within the first 50 μm away from the electrode surface in an heterogeneous media like astroglial scar [150].

The measurement setup, consisting primarily of a lock-in amplifier, is a relatively

inexpensive alternative to commercially available impedance measurement systems previously used to measure impedance at multiple frequencies between chronic electrodes and a skull screw [65, 105, 151]. Commercial systems do have the advantage, however, that they can be used "out of the box", minimizing the temporal cost of building this system. For future electrode design, the simplified measurement system used in this work is amenable to miniaturization. On-chip lock-in amplifiers, such as that designed by Moe et al. [99], could be used to integrate a tissue reaction sensor on the implanted electrode.

For human use, this technique has potential for the real-time monitoring of chronic tissue response to microelectrodes. The technique allows the capability to non-invasively follow the same implant at multiple time points, a necessity for human use. The small currents applied at the electrode are well-below thresholds for eliciting neural activity, and allow the tissue to be probed without the risk of damaging the electrode or the tissue.

5.6 Acknowledgements

The authors gratefully acknowledge Edgar Brown, Dr. Steve P. DeWeerth, and Ben Haeffele for their technical assistance. Funding support was provided by the NIH, R01 DC 06849 (RVB) and NIH NS 045072 (RVB). GTEC, an NSF funded ERC located at Georgia Institute of Technology and Emory University (EEC-9731643), is also acknowledged for the use of core facilities.

CHAPTER VI

CONCLUSIONS AND FUTURE WORK

Neuroprosthetics offer the hope of restoring native limb movement to paralyzed individuals. While the feasibility of the technique has been demonstrated [149, 126, 141, 16, 76, 60], the unreliability of chronic neural recordings remains a significant obstacle to clinical applications. The long-term goal is to enable extraction of meaningful neuronal activity from interfaces which are reliable for a remaining lifetime of use (on the order of decades). In this dissertation, in contrast to the long-held view that astrogliosis alone is responsible for recording failure, we propose an alternative hypothesis for the inconsistency seen in chronic neural recordings: that neurodegeneration, mediated by chronic inflammation, leads to the silencing of activity of target neurons on some recording sites (see red arrows of Figure 1). In developing this idea, we are indebted to the neurodegenerative disease research community, particularly in Parkinson's Disease and Alzheimer's Disease, where the relationship between inflammation and neurodegeneration has been most thoroughly explored [12]. As the primary goal of this thesis was to test for a correlation between chronic inflammatory markers and local neurodegeneration, non-functional electrodes were used to minimize variability between conditions. Future studies will be important to further test the consequences of neurodegeneration on chronic recording failure.

Testing the effect of chronic inflammation on neurodegeneration required a reliable way of varying the degree of inflammation. In Chapter III, we demonstrate that inter-shank spacing modulates the degree of inflammation to microelectrode arrays. We used this to study the 'stickiness' of tissue to the electrode in order to better understand the role of micromotion in the chronic inflammatory response to

microelectrodes. Previous modeling studies suggested that interfacial strain is increased in the case of no adhesion between tissue and electrode in comparison to the case of the tissue and electrode being 'glued' together [77, 133]. We found that adhesion increased with implant duration, and we further investigated the potential cellular contributors to tissue-electrode adhesiveness through correlation analysis of the peak force of electrode extraction with immunohistochemical markers of the tissue response. We found that astrogliosis as indicated by GFAP was the only marker correlated to extraction force in both electrode designs (see Figure 1). These results provide computational modelers with experimental data for modeling the micromotion of Si microelectrode arrays in the brain tissue, since 'stickiness' of scar is proportional to interfacial strain. The contribution of micromotion to chronic inflammation is an area that the Bellamkonda Laboratory is currently studying, using cells cultured on stretchable membranes and studying how the cells respond to small levels of strain.

Regardless of the contribution of micromotion to chronic inflammation, important to our primary hypothesis is that activated microglia and reactive astrocytes surround the electrode interface for several months in primates [48], as we have observed in rats, and that this response can be modulated by electrode geometry. In Chapter IV, we investigated the effect of chronic inflammation on neurodegeneration. We evaluated three time points (2 weeks, 8 weeks, and 16 weeks) to test whether neurodegeneration is progressive. One important aspect of this study was the extended implant duration in comparison with previous studies. At the 16 week time point, we modulated inflammation by 1) stab wound control, 2) age-matched control, and 3) inter-shank spacing. In the case of a stab wound, we could no longer identify the original insertion, as there were no longer any indications of an inflammatory response or neurodegeneration. This finding demonstrates the importance of the persistent presence of the electrode and not only the initial trauma due to insertion. The age-matched control

group also did not show any indication of inflammation or markers of neurodegeneration, indicating that the changes we observed were due to the electrode presence and were not a consequence of aging. In the case of a closer shanked microelectrode, previously shown in Chapter III to elicit a larger inflammatory response, we observed increased neuronal death and dendritic loss after 16 weeks post implantation. Since the largest pyramidal neurons, and therefore strongest electrical signals for recordings, are found in layers IV and V they are commonly used for cortical recordings. Our analysis of depth suggests that neurons at lower cortical depths ($\sim$ layers IV and V) are strikingly more susceptible to dendritic loss than depths closer to the surface such as layers I and II, and suggests differences in susceptibility to degeneration of different neuronal types in the cortical column.

Lastly, in Chapter V, we present an investigation of bioimpedance modeling to monitor the astrocytic response to chronically implanted electrodes, as an indirect means of monitoring chronic inflammation. While a more direct, non-invasive measurement of activated microglia or pro-inflammatory mediators would likely be a better predictor of neurodegeneration, astrogliosis was a much easier target for non-invasive monitoring via impedance spectroscopy. It is important to note here our assumption that astrogliosis is an indicator of microgliosis, which is based on the knowledge that microglial activation precedes the astrogliotic response to intracortical electrodes and the pro-inflammatory cytokines TNF-α and IL1-β released by activated microglia are known to influence astrogliosis. Furthermore, activated microglial activation and astrogliosis were correlated in our Si MEA studies, supporting monitoring astrogliosis as an indirect measure of chronic inflammation. In this study, we measured impedance spectroscopy over a frequency range known to be largely influenced by cell membranes [50]. We modeled the electrical impedance spectra using the Cole model, since previous studies have shown a relationship between the parameters of this model and cell density and hypertrophy [109, 17, 10, 103, 94],

parameters which are known to increase with the extent of astrogliosis. By correlating the parameters of the model with fluorescent markers of cell density and GFAP expression we were able to identify features of the model that might be useful in monitoring surrounding tissue of microelectrodes. Our results suggest that the use of two parameters, f_c and Py, are well correlated with both DAPI and GFAP expression. This correlation was observed only within the first 50 μm away from the electrode interface, providing insight into the spatial resolution of this technique.

In summary, the results of this thesis support an intriguing hypothesis which sheds light on the inconsistency observed from long-term recordings. The hypothesis holds that it is not the astro-glial scar, per se, that is causing recording unreliability, but rather a local, neurodegenerative state. Neurodegenerative features, such as neuronal death, dendritic loss and tauopathy, present as far away as 500 μm from the electrode surface, suggest that neurodegeneration plays a significant role in recording unreliability. Importantly, these data also suggest that mitigating the inflammatory response would be beneficial to attain stable neural recordings. With an accurate understanding of the biological problem and a non-invasive technique for monitoring the root of the problem (inflammation), a closed-loop system can be envisioned to *monitor* inflammation at the electrode interface and control the delivery of anti-inflammatory drugs (i.e. dexamethasone, methylprednisolone) or coatings (see Appendix A) to *mitigate* this inflammation, before neurodegeneration can occur. In this way, it seems possible to *maintain* stable neural recordings and realize more fully the quality-of-life-enhancing potential of cortical neuroprosthetics.

6.1 Future Work

This work suggests that activated microglia are the primary cell type responsible for the observed local neurodegenerative state. The mechanistic link between chronically activated microglia and neurodegeneration, in the context of implanted microelectrodes is unclear, but, based on the neurodegenerative disease literature, pro-inflammatory cytokines and reactive oxygen species would be prime targets for further studies investigating the mechanism. From the literature on chronic electrode implants, little is known about the expression of pro-inflammatory cytokines, such as IL-1, IL-6, and TNF-α at the tissue electrode interface. Biran et al. showed that microglia cultured from retreived microelectrodes release monocyte chemotactic protein-1 (MCP-1) and TNF-α. A study from our lab supports the release of pro-inflammatory cytokines by activated microglia [55]. In this study, after one week, the pro-inflammatory cytokine TNF-α mRNA expression was detected using in situ hybridization at the electrode interface. The TNF-α mRNA was located at the same location as activated microglia visualized with ED-1, suggesting that activated microglia express at least TNF-α after one week implant. TNF-α mRNA levels after four weeks were not observed. ED-1 expression, however, was still present after four weeks. Since TNF-α is known to be important especially in the acute phase, it remains to be seen what, if any, chronic pro-inflammatory cytokines are released by activated microglia. Future work should investigate cytokine expression of fresh tissue across several early (days) and late (months) time points at the electrode interface. Work in the Bellamkonda Lab is currently underway to use laser cutting microscopy (LCM) to microdissect tissue surrounding the microelectrode interface and analyze the homogenized tissue with cytokine antibody arrays.

We do not currently know the relative importance of scar vs. neurodegeneration in long-term recording failure and future experiments will be necessary to tease out the

relative importance of each of these factors. Alternative ways of modulating inflammation to test the effects on neurodegeneration surrounding electrodes may provide clearer insight into the relationship between inflammation and neurodegeration surrounding chronic electrodes. Local delivery of minocyline, which blocks microglia activation, is one example of delivery of a drug with more specific effects than probe geometry. Systemic delivery of NSAIDs is another possibility for targeting inflammation more specifically. Our work on anti-inflammatory coatings for neural probes, including LN (Appendix A) and α-MSH [55], may also be useful in further studying the effects of modulation of microglial response on local neurodegeneration. Longer time points will be needed to investigate whether or not further progression of neurodegeneration occurs beyond 16 weeks. Earlier time points before 2 weeks will be necessary to further elucidate when neuronal loss occurs, since we only observed dead/dying neurons with Fluoro-Jade C at 1 hr and 24 hr time points, suggesting the loss occurs prior to 2 weeks. Inflammation is a double-edged sword, and future work will be necessary to develop methods for harnessing the beneficial effects of inflammation, while mitigating the neurotoxic effects. Indeed, our study of LN coating of neural probes suggests that a controlled, early activation of microglia results in a mitigated chronic microglial and astrocytic response (Appendix A).

In addition to the role of pro-inflammatory mediators in local neurodegeneration, future studies should also investigate the effect of inflammation and neurodegeneration surrounding chronic implants on the activity of nearby neurons. To the best of my knowledge, there are no peer-reviewed studies to date in vivo that have assessed both neural recordings and the tissue response. Recordings in conjunction with good histology would likely require cross-collaboration, since so few groups have the expertise necessary to recording neural signals and assess tissue response well. Recent training initiatives, such as a summer course offered by the Center for Neural Communication Technology (CNCT) at the University of Michigan, Ann Arbor, are seeking

to provide the training necessary to successfully perform the important studies that will combine these disparate techniques.

APPENDIX A

NANOSCALE LAMININ COATING MODULATES CORTICAL SCARRING RESPONSE AROUND IMPLANTED SILICON MICROELECTRODE ARRAYS

A.1 Abstract

Neural electrodes could significantly enhance the quality of life for patients with sensory and/or motor deficits as well as improve our understanding of brain functions. However, long-term electrical connectivity between neural tissue and recording sites is compromised by the development of astroglial scar around the recording probes. In this study we investigate the effect of a nanoscale laminin (LN) coating on Si-based neural probes on chronic cortical tissue reaction in a rat model. Tissue reaction was evaluated after 1 day, 1 week, and 4 weeks post-implant for coated and uncoated probes using immunohistochemical techniques to evaluate activated microglia/macrophages (ED-1), astrocytes (GFAP) and neurons (NeuN). The coating did not have an observable effect on neuronal density or proximity to the electrode surface. However, the response of microglia/macrophages and astrocytes was altered by the coating. One day post-implant, we observed an ∼60% increase in ED-1 expression near LN-coated probe sites compared with control uncoated probe sites. Four weeks post-implant, we observed an ∼20% reduction in ED-1 expression along with an ∼50% reduction in GFAP expression at coated relative to uncoated probe sites. These

results suggest that LN has a stimulatory effect on early microglia activation, accelerating the phagocytic function of these cells. This hypothesis is further supported by the increased mRNA expression of several pro-inflammatory cytokines (TNF-α, IL-1 and IL-6) in cultured microglia on LN-bound Si substrates. LN immunostaining of coated probes immediately after insertion and retrieval demonstrates that the coating integrity is not compromised by the shear force during insertion. We speculate, based on these encouraging results, that LN coating of Si neural probes could potentially improve chronic neural recordings through dispersion of the astroglial scar.

A.2 Introduction

Neural interface technology holds the exciting potential of allowing direct communication between nervous tissue and external electronics. This technology has already significantly enhanced the quality of life for many patients with sensory and/or motor deficits as is evident from both the prosthetic cochlear implant, commonly used for treatment of deafness [4, 112], and deep brain stimulation, which has been used to reduce motor symptoms associated with Parkinsons Disease [108, 14, 86]. Silicon microelectrode arrays (Si MEAs) have been a driving force in the advancement of neural interface technology with several advantages over competitive devices including high-density recording sites, batch fabrication, highly reproducible geometry and usercustomizable dimensions [58]. These micromachined neural prosthetic devices have been used to stimulate and record from the central and peripheral nervous systems [60, 70, 13, 118]. In order to further advance the clinical applications for silicon microelectrode technology, several issues need to be addressed, one of which is improving the reliability of longterm recordings from single units [38]. The underpinning reason for the unreliability is still being investigated. One speculated cause is adverse tissue response induced by the implant. Therefore, the effectiveness of these neural implants could decrease with time following their implantation, either due to

implant-induced astrogliosis, a process which electrically and mechanically isolates the prosthesis from the nervous system [139, 142], and/or due to neuronal cell loss surrounding these devices [7, 37].

Considering that neural interfaces must meet strict demands on long-term performance for clinical efficacy, several strategies have been undertaken to improve the biocompatibility of these devices [110]. One approach to improve the neuron-implant interface is to coat the microelectrode surface with molecules which promote tissue integration [30, 31, 91, 62]. We have previously reported an ultrathin coating of laminin-1 (LN) on Si/SiO_2 surfaces using surface modification by electrostatic layer-by-layer (LbL) self-assembly [52]. The advantage of this technique is its versatility and fine control over layer thickness, which has ramifications on both the stability and impedance characteristics of the coatings. As shown in the previous work, the impedance magnitude at 1 kHz for the coating-modified microelectrode was not statistically different from bare microelectrodes.

The biological contribution to degradation in recording quality over the duration of an implant is currently unknown. Neuronal-related hypotheses generally relate to the physical distance between neurons and recording sites being increased. This may be due to glial cells pushing neurons away and/or neuronal death in the immediate vicinity of the electrode. It has also been suggested that the glial cellular response plays a critical part in recording quality by increasing electrode impedance and creating shunt pathways for current to travel away from recording sites [48].

In this study, we investigate the cortical response, including glial and neuronal cells, to chronically implanted coated Si MEAs compared to uncoated controls in a rat model. We demonstrate that ultrathin LN coatings significantly decrease chronic immunoreactivity, specifically, the gliosis response around coated probes after 4 weeks compared to uncoated bare Si probes.

A.3 Materials and Methods

A.3.1 Preparation of nanoscale LN coatings by LbL

Polyethyleneimine (PEI, Aldrich, MW 25,000) was dissolved in Ultrapure water (MilliQ-plus system, Millipore) with a resistivity of 18.2 MΩ cm to a final concentration of 3 mg ml^{-1} and pH adjusted to 7.4. The solution was then sterilized by filtration through a 0.2 μm sterile filter in a laminar flow hood. Laminin-1 (LN) was purchased from BD Bioscience and diluted to a concentration of 0.2 mg ml^{-1} with phosphate buffered saline (PBS) solution at pH 7.4. Single shank neural probes were obtained from NeuroNexus Technologies. Shank dimensions were 5 mm in length, 33-200 μm wide and 15 μm thick.

LbL surface coatings on the neural probes were prepared according to the method described previously [52]. Briefly, a PEI layer was adsorbed for 30 min onto the neural probes as a precursor layer to initiate the LbL self-assembly. The build-up of the multilayer was accomplished by consecutive adsorption of the oppositely charged polycations PEI and polyanions LN onto the probes. Between each step, the excess polyelectrolyte was removed by rinsing the sample surface with sterile water. For each layer, an incubation time of 20 min and a rinsing time of 1 min were used. A total of eight bilayers of PEI-LN were built on the neural probes.

A.3.2 Evaluation of surface structure and coating integrity

Scanning electron microscopy (SEM) was performed on probes with or without the coating. Images were taken using a LEO 1530 thermally-assisted field emission (TFE) scanning electron microscope at a 5 kV accelerating voltage. In order to determine whether the insertion procedure disrupts the coating integrity, coated probes (n = 4) were inserted into a PBS-perfused rat brain, and subsequently retrieved. The retrieved probes were stained for LN using primary antibody rabbit anti- LN (1:500; Sigma) and secondary antibody goat anti-rabbit IgG Alexa 594 (1:220; Molecular

Probes).

A.3.3 Surgical procedures for chronic implants

Animal procedures adhered to the National Institute of Health (NIH) guidelines and followed a protocol approved by the Institutional Animal Care and Use Committee (IACUC) at Georgia Institute of Technology. Adult male Sprague-Dawley rats were used in this study. This animal model is relevant for the study of chronic tissue reaction to cortical implants, as the glial response has been reported to be similar between rat and non-human primate models [48]. Adult male rats (275-299 g) were anesthetized for 5 min with a mixture of 5% isoflurane and 1 L min-1 O_2 prior to surgery. Each animal was positioned into a stereotactic frame (Kopf) where anesthesia was maintained at 2-3% isoflurane during surgery (with 0.3 L min^{-1} O_2). The animals head was shaven over the incision area and the skin was disinfected with isopropyl alcohol and chlorohexaderm using a scrubbing motion before making the incision. Ophthalmic ointment was applied to the eyes to prevent drying. A midline incision was made along the scalp, the skin retracted, and the periosteum cleared to expose the bregma. A dental drill was used to create a 3.2 mm hole at +0.2 mm anterior and +3.0 mm lateral to the bregma with a custom trephine (24 tooth 3 mm O.D.) fabricated from stainless steel tubing (Small Parts). In order to minimize iatrogenic damage, room temperature saline was applied liberally to the spinning drill bit at the bone interface. The bone plug was carefully removed and the dura was gently pierced and retracted with fine microforceps. The bond-pad region of the coated microelectrode was grasped with Teflon-coated microforceps and the penetrating shank was inserted by hand through the pia into the cortex (Figure 27(A)). Electrode insertion by hand, used in this study,was shown by the previous work [139] to make little difference in tissue reaction around the electrode compared to the automated insertion method. The probe was inserted to the point where only the bond-pad region was visible

outside the cortical surface. A craniotomy of identical diameter was made over the contralateral location (+0.2 mm anterior to the Bregma and -3.0 mm lateral to the midline suture) where the control probe was inserted the same way as described above (Figure 27(B)). Variations were minimized between rats by having both the control and treated probes within the same animal. Variations in insertion depth between the two hemispheres were minimized by inserting the shanks up to the bond-pad, as opposed to estimating a more shallow insertion. After insertion, the bond-pad regions of the probes and the holes were covered with 1% SeaKem Agarose (Cambrex) gel. The craniotomy was further sealed using dental acrylic anchored to the skull using bone screws (Plastics One, Inc.). The skin was sutured shut with 4-0 monofilament nylon and the animals were monitored carefully until full recovery.

A.3.4 Brain tissue preparation for immunohistochemistry

Animals were prepared for immunohistochemistry 1 day, 1 week and 4 weeks after device insertion (n = 3 animals per time point). Each animal was anesthetized with a mixture of ketamine (45.65 mg kg^{-1}), xylazine (9.13 mg kg^{-1}) and acepromazine (1.52 mg kg^{-1}). Animals were then perfused intracardially with PBS prewash followed by 4% paraformaldehyde in PBS. The brains were removed and postfixed for 24 h (4 ℃). The implanted neural probes were then carefully pulled out of the tissue and the brains were placed into 30% sucrose (4 ℃) until they sank to the bottom. The brains were then cryoprotected with optimal cutting temperature (OCT) compound (Tissue-Tek). In order to differentiate between hemispheres, tissue dye was applied to one hemisphere posterior to the insertion sites. Horizontal 30 μm thick tissue sections were cut through the cortex of all brains and the sections were stored at 4 ℃in PBS with 0.01% sodium azide. While the recording sites were located below the cortex, probe width decreases toward the tip (the location of the recording sites). It was therefore assumed that cortical tissue reaction would be overestimated in comparison

(A)

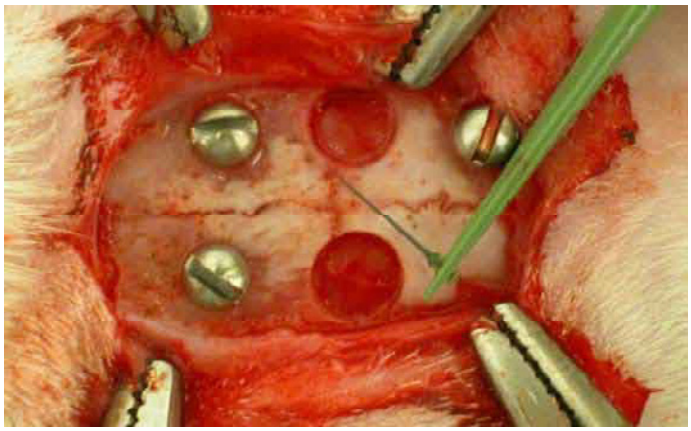

(B)

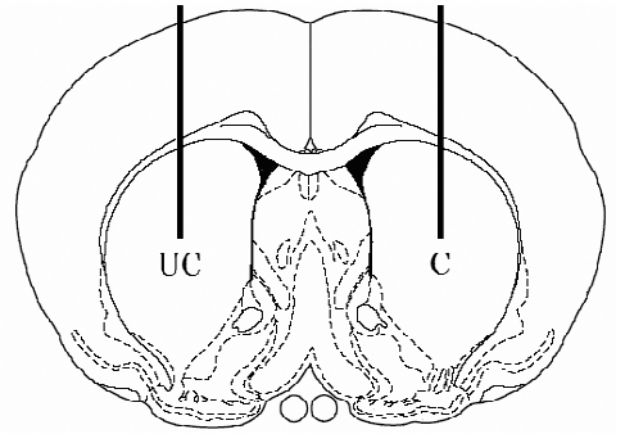

Figure 27: (A) Micrograph of surgical field of view prior to inserting probes. Background: two craniotomy sites and three stainless-steel bone screws. Foreground: probe grabbed with Teflon coated microforceps. (B) Schematic of insertion locations for uncoated (UC) and coated (C) probes (+0.2 mm Bregma, ±3 mm Lateral). Two vertical lines represent probes inserted through the cortex and striatum. Coronal section of adult rat brain adapted from Paxinos and Watson [107].

to the case where recording sites are located in the cortex.

A.3.5 Immunohistochemistry

To study brain tissue response in the cortical region, cortical sections taken from all brains from each group were stained simultaneously for the antibody of interest. Sections were blocked in 4% normal goat serum (GIBCO) with PBS containing 0.5% Triton X-100 (Sigma) for 1 h at room temperature. Sections were then immediately incubated overnight at 4 ℃with primary antibody prepared in blocking solution. Antibodies for the following molecules were used: ED-1 (marker of reactive microglia and macrophages; CD 68 monoclonal mouse IgG1, 1:1000; Serotec); GFAP (specific to astrocytes; polyclonal rabbit IgG, 1:2000; Dako); NeuN (specific to neurons; mouse IgG1, 1:500; Chemicon). After washing in 0.5% triton in PBS, sections were incubated in secondary antibodies for 1 h at room temperature. Secondary antibodies were diluted at a ratio of 1:220 in 0.5% triton in PBS, and included goat anti-rabbit IgG (H + L) Alexa 594 (Molecular Probes) and goat anti-mouse IgG1 Alexa 488 (Molecular Probes). All sections were counterstained by incubation with the nuclear dye DAPI (Molecular Probes) that labeled cell nuclei. Tissue sections were mounted on glass microscope slides with Fluoromount-G (Southern Biotechnology Associates).

A.3.6 Quantitative analysis of immunohistochemical data

All fluorescent images were acquired using a Microfire digital camera and a Zeiss Axioskop2 Plus upright microscope, with the probe site centered in the camera field. In order to minimize unequal illumination, all the images for each marker of interest, i.e. ED-1, GFAP and NeuN, were collected under the same exposure settings within the same day. Image analysis was performed using custom software developed in MATLAB (Image Processing Toolbox included). GFAP intensity as a function of distance from the probe-tissue interface was calculated based on a method used previously [69]. An example is given in Figure 28(A). For each image a point was

manually selected within the probe site and an edge detection algorithm was used to locate the probe-tissue interface (zero-crossing method). This functioned as the zero point for all further distance calculations. Equidistant, equiangular radial lines (n = 120) were drawn around the edge-detected interface and the mean vector was calculated for each image. The average integrals of the 'mean intensity versus distance from probe site vectors for all images were also used in comparing coated and control conditions.

ED-1 response was characterized by calculating the total intensity of each image. Since ED-1 fluorescent intensity was primarily localized to the region directly surrounding the probe site, total fluorescent intensity reflected the degree of macrophage reaction close to the probe-tissue interface. Therefore, a decrease in ED-1 intensity would indicate a lower number of macrophages and activated microglia at the probe-tissue interface.

Our objectives in analyzing the NeuN images were to quantify the number of neuronal nuclei and their proximity to the probe-tissue interface (Figure 28(C)). RGB images were first converted to black and white. The area and centroid position of each contiguous white region was then calculated, wherewhite regions represented cell bodies. Contiguous white regions with an area less than two standard deviations from the mean area were excluded from further analysis. Four endpoints were manually selected at the four corners of the remaining hole left after removal of the probe. From these four endpoints two lines were calculated which outlined the longest edges of the probe-tissue interface. White contiguous regions with centroids located less than or equal to 200 m perpendicular to the drawn interface lines were included in further processing. The following features were stored for further analysis: distance to nearest centroid, total number of centroids, mean perpendicular distance of probe-tissue interface to centroids, and density (no. of centroids/area).

All statistical inferences were made between coated and uncoated conditions using

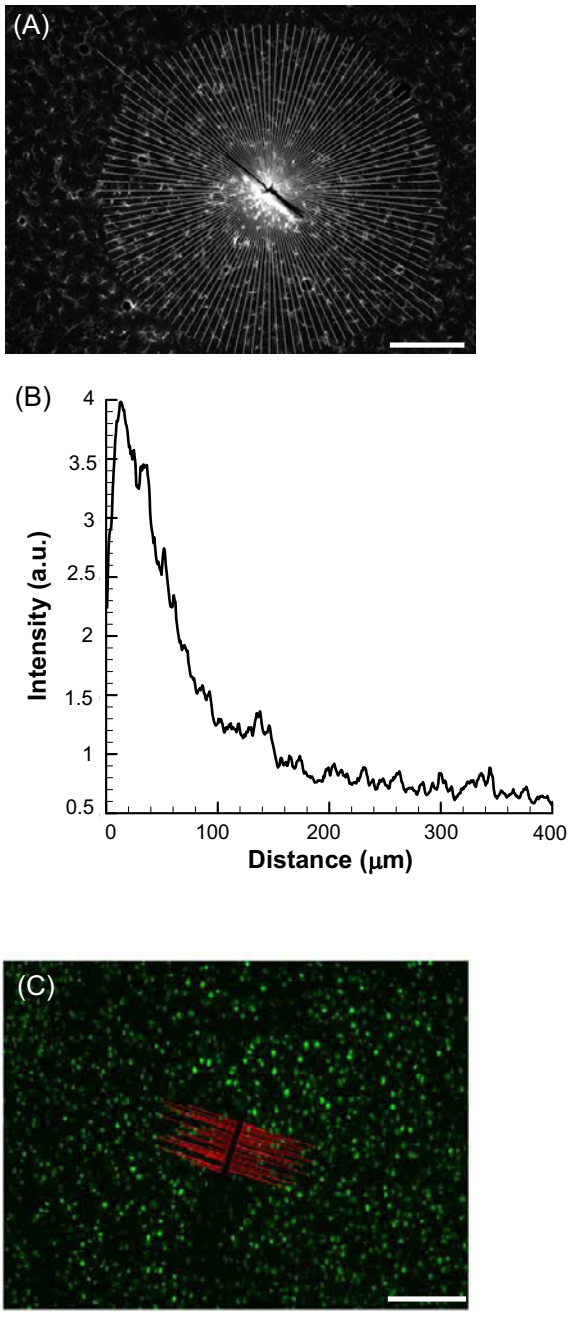

Figure 28: (A) Representative black and white sample image immunostained for GFAP with sampling lines (n=120). Scale bar = 200 μm. (B) Average fluorescent intensity profile plotted as a function of distance from the probe site. The area under the curve is the average total GFAP intensity. (C) Representative sample image immunostained for NeuN with probe site and distances to neuron centroid locations outlined in red. Scale bar = 200 μm.

Students t-test analysis (two-tailed) between like parameters. A minimum of four sections per cortical region was used to obtain the average for a particular marker.

A.3.7 In vitro primary microglial culture

To examine the response of microglia to the LN coating, in vitro microglial cell culture was studied. Primary mixed glial cell cultures were prepared from brains of newborn Sprague-Dawley rats on postnatal day 1 or day 2 as described by Giulian and Baker [46]. Briefly, the cerebral cortices of the animals were isolated aseptically and the meninges were carefully removed. The cleaned cortices were placed in a droplet of L15 medium (GIBCO) and mechanically dissociated using a fine dissecting knife. The tissue was further dissociated in 0.25% trypsin-EDTA (Invitrogen) at 37°C for 20 min. Following digestion, an equal volume of DMEM-F12 medium (GIBCO) with 10% fetal bovine serum was added to stop the reaction. After a brief centrifugation, the cells were resuspended and plated in 75 cm^2 tissue culture flasks (Fisher) coated with poly-L-lysine at a density of one brain per flask in culture medium consisting of DMEM-F12 media supplemented with 10% fetal bovine serum and 1% penicillin/streptomycin. After 7-10 days, flasks were lightly shaken and the medium containing detached microglial cells were collected and centrifuged into a pellet. The cells were resuspended in DMEM-F12 medium with 10% fetal bovine serum, counted, and plated at a density of 150,000 cells/cm^2 on sterile LN-coated and uncoated 1 X 1 cm Si wafers, which were placed in individual wells of a 24-well culture plate and cultured for 24 h in 5% CO_2 atmosphere at 37°C.

A.3.8 Real-time PCR

The relative expressions of the targeted genes from the above microglial culture were measured using reverse-transcription 'real-time' quantitative polymerase chain reaction (RT-qPCR). The mRNA extraction was carried out using the materials and protocol provided in the RNeasy Mini Kit (Qiagen). Total RNA concentration and

purity were determined by spectrophotometry at 260 and 280 nm. After isolation, the mRNA (0.5 μg) of each sample was reverse-transcribed with 20 μl of iScript cDNA Synthesis Kit (Bio-Rad) containing random hexamer primers, oligo-(dT) and reverse transcriptase. The cDNA products were stored at -20 ℃or used immediately for PCR.

Real-time RT-PCR reactions were performed under each cytokine-specific condition to amplify three kinds of inflammatory cytokines, tumor necrosis factor alpha (TNF-α), interleukin-1 (IL-1) and interleukin-6 (IL-6) (Figure 29). These cytokines were chosen based on the compelling evidence of the pivotal roles they play in influencing CNS response to injury [64]. For each of the primer sets, nonspecific amplification was confirmed absent after electrophoresis and ethidium bromide staining of agarose gels. PCR was carried out using the QuantiTect SYBR Green RT-PCR Kit and protocol. All RT-PCR experiments were performed using the iCycler (Bio-Rad). The protocol utilizes the following thermal parameters: activation step, 3 min at 95 ℃; three-step cycling (35 cycles): denaturation, 30 s at 95 ℃, annealing, 30 s at either 60.5 ℃(TNF-α) or 55 ℃(IL-1 and IL-6), extension, 1 min at 72 ℃. A melt curve was subsequently performed to confirm that there was no primer dimer in the PCR products, which began at 55 ℃and increased to 95 ℃in 0.4 ℃increments. Relative standard curves for the candidate genes were performed each time the genes were analyzed and used for all the samples to obtain the relative quantity from the RT-qPCR of the targeted gene expression of each sample.

Cytokine	Size (bp)	Primers	Optimal condition		Accession number
			Tm (°C)	$MgCl_2$ (mM)	
TNF-α F (5')	76	TGCCTCAGCCTCTTCTCATT	60.5	1.5	**NM_012675**
TNF-α R (5')		CAATCACCCCGAAGTTCAGT			
IL-1 F (5')	103	TGAAGAAGAGACGGCTAAGTTTC	55.0	1.5	**NM_017019**
IL-1 R (5')		TGAGGTGCTGATCTGGGTTG			
IL-6 F (5')	162	CCACCAGGAACGAAAGTC	55.0	1.5	**NM_012589**
IL-6 R (5')		GGTATCCTCTGTGAAGTCGT			

Figure 29: Oligonucleotide primers and optimal condition for real-time RT-PCR.

A.4 Results

A.4.1 Surface characterization and coating integrity

SEM was used to examine the surface of the LN-coated probe. As shown in Figure 30(A), little difference was observed between surfaces of uncoated and coated probes. The surface appeared to be smooth and the coating was homogeneous, both on and around the recording site. A common concern with coating is the risk of delamination upon device insertion. Using an antibody against LN, we evaluated the coating integrity after the probe was subjected to insertion process. LN-positive antibody binding was observed along the shank and on the recording sites (Figure 30(B)), suggesting that the insertion step did not disrupt the distribution of the coating on the probe surface.

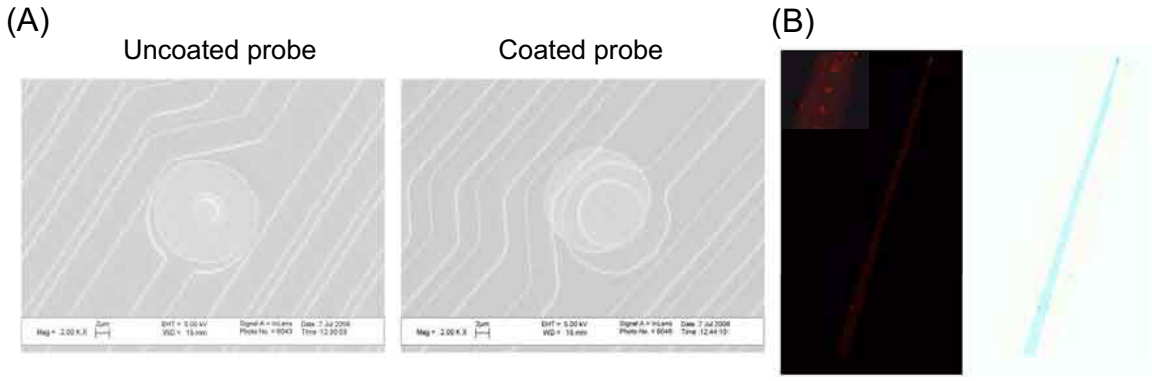

Figure 30: (A) SEM images of the uncoated and coated probes. Scale bar in the images is 2 μm. (B) Montage image of LN staining on probe that was subjected to insertion test. Inset is a higher magnification image showing detail of the recording sites. To aid in visualization, the corresponding pseudocolor image is shown.

A.4.2 ED-1 immunoreactivity

Activated microglia and macrophages were identified via ED- 1 staining. One day after surgery, the uncoated probe site was characterized by a faint diffusive ED-1 staining with a few labeled cells (Figure 31). On the coated probe site, the staining showed a significant increase in the number of small, ameboid ED-1 positive cells

surrounding the area. The intensity of the ED-1 staining for the coated probe was ∼60% higher than that of the uncoated probe ($p < 0.05$).

One week after insertion, the responses were very similar between the uncoated and coated probes (Figure 31). The majority of the ED-1+ cells had the appearance of large, round, blood-borne monocytes/macrophages. Smaller, processbearing microglia were also seen at various distances from the injury site. However, differences in ED-1 staining were seen 4 weeks post-surgery. Lower ED-1+ staining was observed for the coated probe: ∼20% less than that of the uncoated probe ($p < 0.05$). The ED-1+ cell layer was more compact (shown by the arrow) in contrast to the observation of 1 week, and only phagocytic ameboid microglia/macrophage cells were seen around the insertion site.

A.4.3 GFAP immunoreactivity

GFAP is a commonly used marker to evaluate reactive gliosis as an astrocytic reaction to injury. One day after surgery, both coated and control insertion sites were characterized by appearance of elevation in GFAP intensity (Figure 32(A)), compared to the normal cortical tissue far away from the insertion site. Such elevation was observed up to 400 μm from the site.

After 1 week, in both control and LN-coated cases, the insertion sites showed a substantial increase in GFAP reactivity (Figure 32(A)). The staining revealed astrocytes surrounding the insertion sites became hypertrophic, elongated with thick processes as compared to those in the intact brain region, which were more stellate in appearance. GFAP immunoreactivity was maximum in the immediate border zones of the insertion site and declined progressively as a function of distance from the site, extending up to 300 μm either side. There was little difference in terms of GFAP intensity between the coated probe and uncoated probe at the 1 day and 1 week post-implantation, as demonstrated by the average intensity line profile (Figure 32(B) and

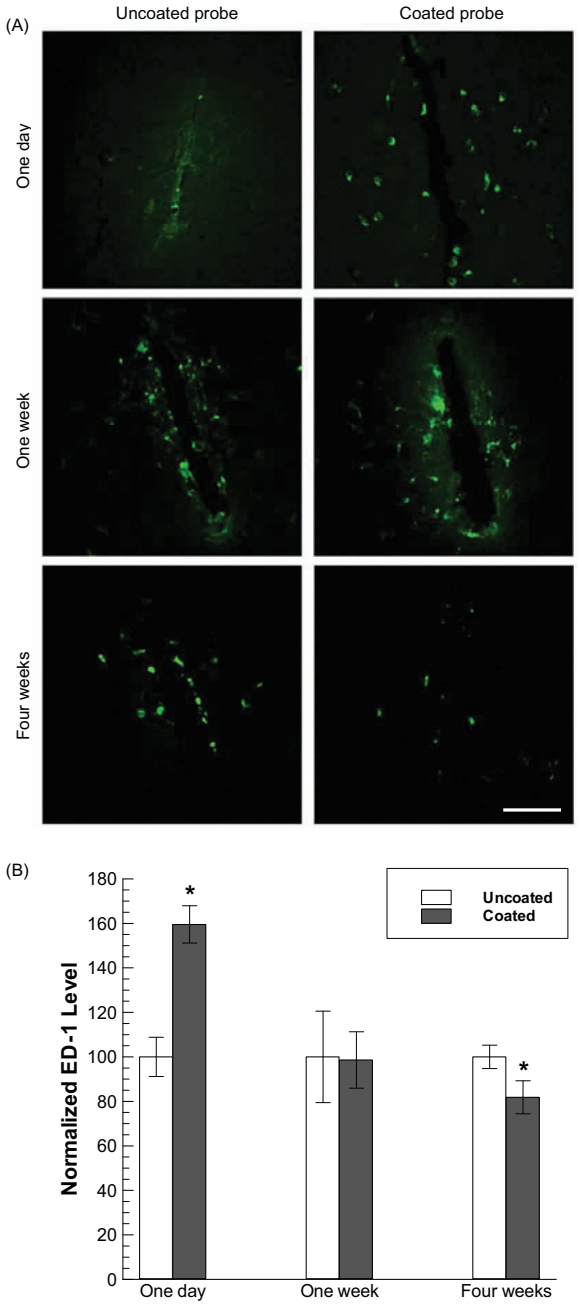

Figure 31: (A) Representative images of ED-1 staining for both uncoated and coated conditions at one day, one week and four weeks post insertion. (B) The percentage of ED-1 fluorescent intensity of coated compared to uncoated was plotted. At day one, the coated probe showed significantly higher ED-1 intensity than the uncoated probe ($p < 0.05$). No significant difference was observed between conditions at the one-week time point. Intensity was significantly reduced for coated probes at the four-week time point ($p < 0.05$). Scale bar = 50 μm.

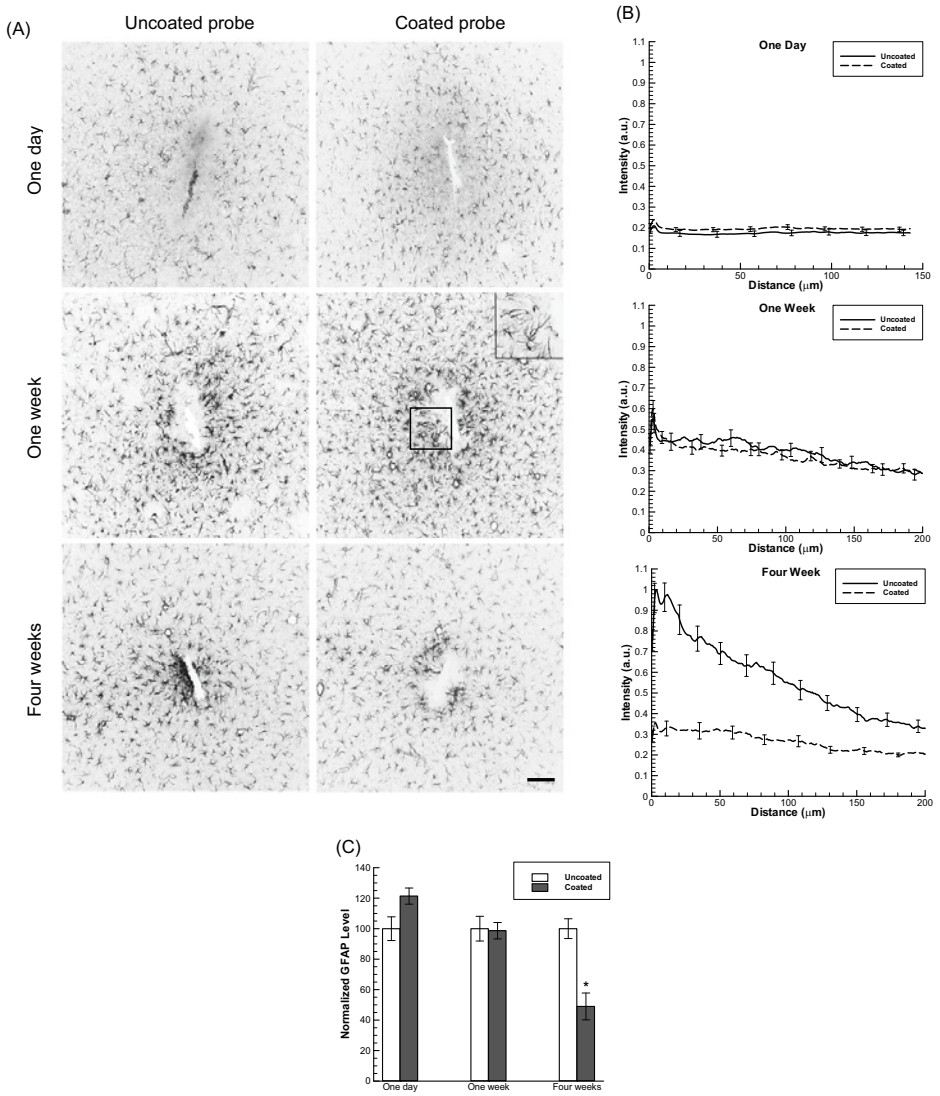

Figure 32: (A) GFAP immunohistochemistry of tissue sections from brains implanted with uncoated probes and LN coated probes at one day, one week and four weeks post insertion. One day after surgery, elevation of GFAP intensity started to emerge surrounding the insertion site. By one-week post surgery, hypertrophic astrocytes with intense GFAP labeling were observed around probe sites (see inset). The response was similar between the uncoated and coated probes. However, by week four, a less intense GFAP staining was located around the coated than the uncoated probe site. (B) Quantitative comparison of GFAP immunoreactivity between the uncoated and coated probes was made via GFAP intensity profiles as a function of distance from the probe site. SEM bars from 20% of the data points were displayed. (C) Total GFAP intensity for the coated probe, defined as the integral of each intensity line profile shown in (B), was normalized to that of the uncoated probe. As shown in the plots, no statistical difference in mean fluorescent intensity profile was observed at the one-day and one-week time points. At the four-week time point, GFAP intensity was higher for uncoated than coated ($p < 0.01$), in other words, the percentage of coated GFAP fluorescent intensity compared to uncoated was significantly reduced ($p < 0.01$). Scale bar = 100 μm.

(C)).

By week 4, the GFAP positive zone became compact around the uncoated probe insertion site, approximately 100 μm in radius (Figure 32(A)). These astrocytes exhibited an interwoven appearance. For the coated probe, the GFAP intensity within the vicinity of the insertion site decreased even more dramatically and was comparable to that in the intact region. The average intensity line profiles indicated a significant GFAP reduction for the coated probe ($\sim$50% less than the uncoated probe ($p < 0.01$), Figure 32(B) and (C)).

A.4.4 Immunostaining of neurons

Neuronal response to the probes was characterized via NeuN staining (Figure 33), which is specific to neuronal nuclei. One day post-surgery, a decrease in the number of neurons immediately adjacent to the insertion site was observed for both the uncoated and coated probes. By the end of 1 week, a neuron-depleted zone approximately 30 μm away from the probe site was developed for both uncoated and coated probes. At the end of 4 weeks, little change was seen for the zone. NeuN quantitative analysis did not reveal any statistical differences between coated and uncoated conditions. This was the case in all of the parameters we investigated, including distance to nearest neuron, total number of neurons, mean perpendicular distance of probe-tissue interface to neurons, and density (no. of neurons/area). This may imply that a coating employing a diffusible pharmacological agent, e.g. nerve growth factor, is necessary to modulate neurons beyond the glial scar.

A.4.5 Real-time PCR

Real-time RT-PCR analysis of cytokine production indicated that there were significant, quantitative differences in microglial responses to bare silicon and LN-coated silicon samples (Figure 34). Overall, the pro-inflammatory cytokine expression was significantly higher ($p < 0.01$) for microglia cultured on the LN-coated silicon sample.

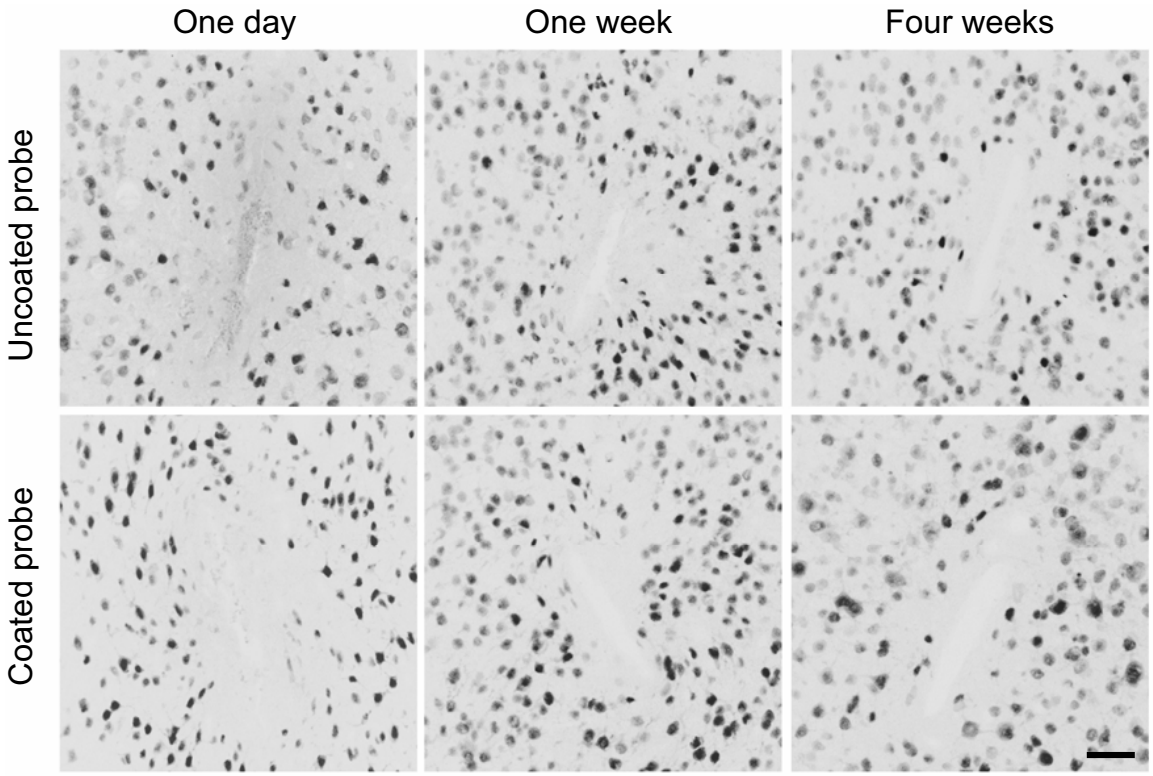

Figure 33: Immunostaining of neurons with NeuN at one day, one week and four weeks post insertion. The distribution of NeuN positive cells around the probe site was similar for both probes at all three time points. Scale bar = 100 μm.

Cells had a more than three-fold increase in TNF-α expression, 14-fold increase in IL-1 expression, and 11-fold increase in IL-6 expression. Regardless of the substrate type, TNF-α expression was higher than IL-1, and IL-6 expression was lowest.

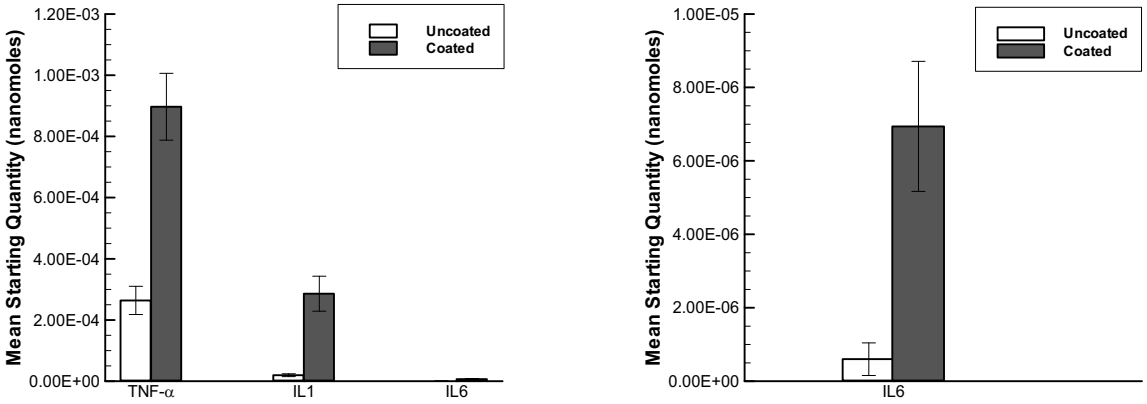

Figure 34: Gene expression of pro-inflammatory cytokines TNF-α, IL-1 and IL-6 after 24 h microglial culture quantified by real time RT-PCR. There was statistic difference for each gene between microglia grown on the bare Si and on LN coated Si ($p < 0.01$).

A.5 Discussion

The main objective of this study was to evaluate in vivo brain tissue response to micromachined Si neural probes modified with nanoscale coating of LN. Several studies have investigated CNS response to LN in vitro including isolated neurons [61], neurons and astrocytes in co-culture [28], and microglia [19]. However, the effect of LN on microglia/macrophage and astrocyte function in vivo, to our knowledge, has not been explored. In this study, local presence of neurons, macrophages/activated microglia and reactive astrocytes at the implantation site of Si probes were compared between bare and LN-coated probes 1 day, 1 week and 4 weeks post-implantation.

Studies have shown that following a penetrating injury to the central nervous system (CNS), a complex cellular event occurs which usually leads to reactive gliosis [41, 130]. Given the high vascular density in the brain, inserting the micromachined silicon probe into the brain inevitably ruptures blood vessels. Recently, Bjornsson et

al [9] have demonstrated the vascular damage generated by the neuroprosthetic device insertion. As a result of vascular damage, macrophages derived from the bloodstream are recruited to the injury site and microglia, the resident immune cell of the brain, become activated. One indication of microglial activation is their transformation in morphology from ramified to ameboid configuration [72]. In our study, ED-1+ microglia/macrophages were observed immediately next to the insertion site, indicating that these cells form the front line of defense against the implanted probes. Although little difference between LN-coated and uncoated probes was observed in microglia/macrophage response after 1 week, differences were noted in both the earlier acute phase (1 day) and later chronic phase (4 weeks). The coated probe induced a considerably higher ED-1 staining at 1 day postimplantation, suggesting that the LN coating initiated a greater response frommicroglia/macrophages. In vitro real-time PCR results have shown that microglia cultured on the LN surface had substantial upregulation of pro-inflammatory cytokines, namely, TNF-α, IL-1 and IL-6 mRNA expression. Our observation ofmicroglia activation by LNis consistent with the observation of Chamak and Mallat [19]. Studies have shown that these pro-inflammatory cytokines secreted by activated microglia can further activate adjacent microglia and astrocytes, via autocrine and paracrine pathways, leading to propagation and enhancement of the acute inflammatory response [51, 73]. These findings suggest that LN may have an acute stimulatory effect on microglia, which is further supported by the observed higher ED-1 response for coated probes after 1 day. Significantly lower ED-1 staining observed after 4 weeks for the coated probe implies that the coating evoked less microglia activation in the long term.

One possible mechanism for the beneficial attenuation in astrogliosis at 4 weeks with LN-coated probes is that LN triggers a boosted, well-coordinated, clean-up response from microglia/macrophages of the necrotic debris after injury. Mitigation

of astrogliosis by activation of microglia/macrophages is supported by several relevant studies. Using a microlesion model which resulted in minimal necrotic debris, Davies et al reported that ameboid microglia appeared 1 day after injury and quickly disappeared [32]. The disappearance of microglia was likely due to their successful removal of the debris resulting from the microlesions. Schwartz et al have investigated treatment strategies for tissue repair in the injured spinal cord using the approach of stimulating, as opposed to suppressing, the CNS immune system through activated macrophages [75, 74, 162].

Besides microglia, astrocytes play an important role in response to injury. In our study, the response patterns of astrocytes to injury caused by probe insertion were qualitatively comparable to that observed by Szarowski et al [139]. Initially, a broad zone of reactive astrocytes, characterized by their larger size, longer and thicker processes, and increased GFAP expression, surrounded both uncoated and LN-coated probe insertion sites. This broad band of reactive astrocytes indicated that astrocytes started to form a barrier between the injury site and the surrounding tissue. After 4 weeks post-implantation, the zone had evolved into a narrow sheath of tightly interwoven astrocyte layer encircling the uncoated probe. In contrast, a mild astrocytic response, as characterized by disconnected segments of relatively low GFAP expression, was seen after 4 weeks for the coated probe.

The observed correlation between ED-1 immunoreactivity and GFAP immunoreactivity chronically is interesting as it indicates intercellular crosstalk between microglia/macrophages and astrocytes. As mentioned above, upon activation, microglia release cytokine products, such as IL-1, IL-6 and TNF-α, which can mediate astrogliosis [51]. It is possible that the diminished astrocytic response for the coated probe in the chronic phase resulted from the reduced number of activated microglia present at the injury site, which induced a lower cytokine production. The lack of difference in astrocyte response 1 day following surgery between the uncoated and coated probes

may be due to a sub-threshold concentration of the produced cytokines required for astrocyte activation in vivo at this time point.

The high-density cellular sheath surrounding Si MEAs has been suggested as being a significant cause in the electrical isolation of implants in the brain [142]. At least three hypotheses for how the glial scar degrades signal quality over time have been proposed: (1) by promoting a chemically inhibitory environment for neural processes [41], (2) by increasing the distance between recording site and nearest neurons [84], and (3) by insulating the probe from surrounding neurons, thus increasing impedance [142, 41].

Neuronal proximity to electrode recording sites, neuronal density, and current flow between neurons and electrode sites are three primary factors affecting recording quality. Differences in neuronal proximity to electrode recording site and neuronal density between bare and LN-coated probeswere not observed. This finding sheds light on the cellular audience of immobilized and diffusion-based coating strategies. A coating based on protein/drug immobilization to the electrode surface is perhaps not well suited for targeting neurons, since the cellular layers ofmicroglia and reactive astrocytes separate neurons from 'seeing' the electrode surface. A coating based on the diffusion of a pharmacological agent(s) might be a better method to influence neurons beyond the glial scar. While a diffusion-based coating has the potential for modulating neuronal and glial cells, immobilized coatings affect those cells in contact with the electrode surface, namely, microglia and astrocytes. Although neuron-to-recording site distance is a critical factor in neural recordings, it is not sufficient. It has been suggested that glial cells are a major cause of these phenomena by obstructing pathways for current flow between neurons and recording sites [113]. It follows that a tightly woven glial sheath between electrode and neuron would block any low resistance paths between recording site and nearby neurons. This line of reasoning is

supported by a study reporting that regions in and around glial scar have less permissible diffusion [114]. As with molecules, glial scars impede current flow between electrodes and nearby neurons by a combination of a decrease in extracellular fluid volume between astrocytes and an increase in resistivity due to the tissue composition itself [49]. The intimate relationship between extracellular fluid volume and electrode impedance has been studied in the cochlea [35]. A mitigated glial scar with extracellular clefts between astrocytes may significantly improve recording reliability by sustaining low resistance channels for current flow between firing neurons and recording sites. Since a complete analysis of chronic recording data was beyond the scope of this study, we are at this time unable to correlate our histological results to recording quality over time.

In summary, the surface modification of Si MEAs with PEI-LN LbL coating is able to mitigate the long-term tissue response to chronic implants. Long-term reduction of glial scar surrounding the coated implant was correlated with an initial amplified local activation of resident and blood-borne macrophages induced by LN. These findings suggest that LN may be useful in mitigating astrogliosis in other neural-related chronic applications as well. We suggest that the addition of diffusible neurotrophic factors may further facilitate the active 'management of the interface to promote long-term recording stability.

A.6 Acknowledgements

The authors gratefully acknowledge the contributions of Mr Matt Davis, Dr Youngtae Kim and Dr Rupal Thazhath for their technical assistance. Funding support was provided by the National Institute of Health, R01 DC06849 and NS45072 (RVB). GTEC, an NSF funded ERC located at Georgia Institute of Technology and Emory University, is also acknowledged for the use of core facilities.

REFERENCES

[1] Abidian, M., Kim, D., and Martin, D., "Conducting-polymer nanotubes for controlled drug release," *Adv Mat*, vol. 18, no. 4, pp. 405–409, 2006.

[2] Alonso, A., Zaidi, T., Novak, M., Grundke-Iqbal, I., and Iqbal, K., "Hyperphosphorylation induces self-assembly of tau into tangles of paired helical filaments/straight filaments," *Proc Natl Acad Sci U S A*, vol. 98, no. 12, pp. 6923–8, 2001.

[3] Augustinack, J. C., Schneider, A., Mandelkow, E. M., and Hyman, B. T., "Specific tau phosphorylation sites correlate with severity of neuronal cytopathology in alzheimer's disease," *Acta Neuropathol (Berl)*, vol. 103, no. 1, pp. 26–35, 2002.

[4] Bell, T., Wise, K., and Anderson, D., "A flexible micromachined electrode array for a cochlear prosthesis," *Sens Actuators A*, vol. 66, pp. 63–69, 1998.

[5] Bhadra, N. and Mortimer, J., "Extraction forces and tissue changes during explant of cwru-type intramuscular electrodes from rat gastrocnemius," *Ann Biomed Eng*, vol. 25, no. 6, pp. 1017–1025, 1997.

[6] Bhadra, N. and Mortimer, J., "Extraction force and tissue change during removal of a tined intramuscular electrode from rat gastrocnemius," *Ann Biomed Eng*, vol. 34, no. 6, pp. 1042–1050, 2006.

[7] Biran, R., Martin, D. C., and Tresco, P. A., "Neuronal cell loss accompanies the brain tissue response to chronically implanted silicon microelectrode arrays," *Exp Neurol*, vol. 195, no. 1, pp. 115–26, 2005.

[8] Biran, R., Martin, D. C., and Tresco, P. A., "The brain tissue response to implanted silicon microelectrode arrays is increased when the device is tethered to the skull," *J Biomed Mater Res A*, vol. 82, no. 1, pp. 169–78, 2007.

[9] Bjornsson, C. S., Oh, S. J., Al-Kofahi, Y. A., Lim, Y. J., Smith, K. L., Turner, J. N., De, S., Roysam, B., Shain, W., and Kim, S. J., "Effects of insertion conditions on tissue strain and vascular damage during neuroprosthetic device insertion," *J Neural Eng*, vol. 3, no. 3, pp. 196–207, 2006.

[10] Blad, B., "Clinical applications of characteristic frequency measurements: preliminary in vivo study," *Med Biol Eng Comput*, vol. 34, no. 5, pp. 362–5, 1996.

[11] Block, M. L. and Hong, J. S., "Microglia and inflammation-mediated neurodegeneration: multiple triggers with a common mechanism," *Prog Neurobiol*, vol. 76, no. 2, pp. 77–98, 2005.

[12] Block, M. L., Zecca, L., and Hong, J. S., "Microglia-mediated neurotoxicity: uncovering the molecular mechanisms," *Nat Rev Neurosci*, vol. 8, no. 1, pp. 57–69, 2007.

[13] Branner, A., Stein, R., and Normann, R., "Selective stimulation of cat sciatic nerve using an array of varying-length microelectrodes," *J Neurophysiol*, vol. 85, pp. 1585–1594, 2001.

[14] Breit, S., Schulz, J. B., and Benabid, A. L., "Deep brain stimulation," *Cell Tissue Res*, vol. 318, no. 1, pp. 275–88, 2004.

[15] Buee, L., Bussiere, T., Buee-Scherrer, V., Delacourte, A., and Hof, P. R., "Tau protein isoforms, phosphorylation and role in neurodegenerative disorders," *Brain Res Brain Res Rev*, vol. 33, no. 1, pp. 95–130, 2000.

[16] Carmena, J. M., Lebedev, M. A., Crist, R. E., O'Doherty, J. E., Santucci, D. M., Dimitrov, D. F., Patil, P. G., Henriquez, C. S., and Nicolelis, M. A., "Learning to control a brain-machine interface for reaching and grasping by primates," *PLoS Biol*, vol. 1, no. 2, p. E42, 2003.

[17] Casas, O., Bragos, R., Riu, P. J., Rosell, J., Tresanchez, M., Warren, M., Rodriguez-Sinovas, A., Carreno, A., and Cinca, J., "In vivo and in situ ischemic tissue characterization using electrical impedance spectroscopy," *Ann N Y Acad Sci*, vol. 873, pp. 51–8, 1999.

[18] Castillo-Ruiz, M. M., Campuzano, O., Acarin, L., Castellano, B., and Gonzalez, B., "Delayed neurodegeneration and early astrogliosis after excitotoxicity to the aged brain," *Exp Gerontol*, vol. 42, no. 4, pp. 343–54, 2007.

[19] Chamak, B. and Mallat, M., "Fibronectin and laminin regulate the in vitro differentiation of microglial cells," *Neuroscience*, vol. 45, no. 3, pp. 513–27, 1991.

[20] Chapin, J. K., Moxon, K. A., Markowitz, R. S., and Nicolelis, M. A., "Real-time control of a robot arm using simultaneously recorded neurons in the motor cortex," *Nat Neurosci*, vol. 2, no. 7, pp. 664–70, 1999.

[21] Cho, J. H. and Johnson, G. V., "Primed phosphorylation of tau at thr231 by glycogen synthase kinase 3beta (gsk3beta) plays a critical role in regulating tau's ability to bind and stabilize microtubules," *J Neurochem*, vol. 88, no. 2, pp. 349–58, 2004.

[22] Choi, S. H., Lee, D. Y., Kim, S. U., and Jin, B. K., "Thrombin-induced oxidative stress contributes to the death of hippocampal neurons in vivo: role of microglial nadph oxidase," *J Neurosci*, vol. 25, no. 16, pp. 4082–90, 2005.

[23] Cole, K. S., "Permeability and impermeability of cell membranes for ions," *Cold Spring Harbor Sympos Quant Biol*, vol. 8, pp. 110–122, 1940.

[24] Cole, K. S. and Cole, R. H., "Dispersion and adsorption in dielectrics," *J. Chem. Rev.*, vol. 9, pp. 341–352, 1941.

[25] Collias, J. C. and Manuelidis, E. E., "Histopathological changes produced by implanted electrodes in cat brains; comparison with histopathological changes in human and experimental puncture wounds," *J Neurosurg*, vol. 14, no. 3, pp. 302–28, 1957.

[26] Collombet, J. M., Masqueliez, C., Four, E., Burckhart, M. F., Bernabe, D., Baubichon, D., and Lallement, G., "Early reduction of neun antigenicity induced by soman poisoning in mice can be used to predict delayed neuronal degeneration in the hippocampus," *Neurosci Lett*, vol. 398, no. 3, pp. 337–42, 2006.

[27] Cornish, B. H., Thomas, B. J., and Ward, L. C., "Improved prediction of extracellular and total body water using impedance loci generated by multiple frequency bioelectrical impedance analysis," *Phys Med Biol*, vol. 38, no. 3, pp. 337–46, 1993.

[28] Costa, S., Planchenault, T., Charriere-Bertrand, C., Mouchel, Y., Fages, C., Juliano, S., Lefrancois, T., Barlovatz-Meimon, G., and Tardy, M., "Astroglial permissivity for neuritic outgrowth in neuron-astrocyte cocultures depends on regulation of laminin bioavailability," *Glia*, vol. 37, no. 2, pp. 105–13, 2002.

[29] Csicsvari, J., Henze, D. A., Jamieson, B., Harris, K. D., Sirota, A., Bartho, P., Wise, K. D., and Buzsaki, G., "Massively parallel recording of unit and local field potentials with silicon-based electrodes," *J Neurophysiol*, vol. 90, no. 2, pp. 1314–23, 2003.

[30] Cui, X., Lee, V., Raphael, Y., Wiler, J., Hetke, J., Anderson, D., and Martin, D., "Surface modification of neural recording electrodes with conducting polymer/biomolecule blends," *J Biomed Mater Res.*, vol. 56, no. 2, pp. 261–72, 2001.

[31] Cui, X., Wiler, J., Dzaman, M., Altschuler, R. A., and Martin, D. C., "In vivo studies of polypyrrole/peptide coated neural probes," *Biomaterials*, vol. 24, no. 5, pp. 777–87, 2003.

[32] Davies, S., Field, P., and Raisman, G., "Regeneration of cut adult axons fails even in the presence of continuous aligned glial pathways," *Exp Neurol*, vol. 142, pp. 203–216, 1996.

[33] De Lorenzo, A., Andreoli, A., Matthie, J., and Withers, P., "Predicting body cell mass with bioimpedance by using theoretical methods: a technological review," *J Appl Physiol*, vol. 82, no. 5, pp. 1542–58, 1997.

[34] Dias-Santagata, D., Fulga, T. A., Duttaroy, A., and Feany, M. B., "Oxidative stress mediates tau-induced neurodegeneration in drosophila," *J Clin Invest*, vol. 117, no. 1, pp. 236–45, 2007.

[35] Duan, Y., Clark, G., and Cowan, R., "A study of intra-cochlear electrodes and tissue interface by electrochemical impedance methods in vivo," *Biomaterials*, vol. 25, pp. 3813–3828, 2004.

[36] Eckermann, K., Mocanu, M. M., Khlistunova, I., Biernat, J., Nissen, A., Hofmann, A., Schonig, K., Bujard, H., Haemisch, A., Mandelkow, E., Zhou, L., Rune, G., and Mandelkow, E. M., "The beta -propensity of tau determines aggregation and synaptic loss in inducible mouse models of tauopathy," *J Biol Chem*, 2007.

[37] Edell, D. J., Toi, V. V., McNeil, V. M., and Clark, L. D., "Factors influencing the biocompatibility of insertable silicon microshafts in cerebral cortex," *IEEE Trans Biomed Eng*, vol. 39, no. 6, pp. 635–43, 1992.

[38] Editorial, "Is this the bionic man?," *Nature*, vol. 442, p. 109, 2006.

[39] Eisch, A. J. and Marshall, J. F., "Methamphetamine neurotoxicity: dissociation of striatal dopamine terminal damage from parietal cortical cell body injury," *Synapse*, vol. 30, no. 4, pp. 433–45, 1998.

[40] Faulkner, J. R., Herrmann, J. E., Woo, M. J., Tansey, K. E., Doan, N. B., and Sofroniew, M. V., "Reactive astrocytes protect tissue and preserve function after spinal cord injury," *J Neurosci*, vol. 24, no. 9, pp. 2143–55, 2004.

[41] Fawcett, J. and Asher, R., "The glial scar and central nervous system," *Brain Res Bulletin*, vol. 49, pp. 377–391, 1999.

[42] Fillit, H., Ding, W. H., Buee, L., Kalman, J., Altstiel, L., Lawlor, B., and Wolf-Klein, G., "Elevated circulating tumor necrosis factor levels in alzheimer's disease," *Neurosci Lett*, vol. 129, no. 2, pp. 318–20, 1991.

[43] Fomekong, R. D., Pliquett, U., and Pliquett, F., "Passive electrical properties of rbc suspensions: changes due to distribution of relaxation times in dependence on the cell volume fraction and medium conductivity," *Bioelectrochemistry and Bioenergetics*, vol. 47, p. 8188, 1998.

[44] Gander, W., Golub, G. H., and Strebel, R., "Least-squares fitting of circles and ellipses," *BIT*, vol. 43, p. 558578, 1994.

[45] Gao, H. M., Liu, B., Zhang, W., and Hong, J. S., "Novel anti-inflammatory therapy for parkinson's disease," *Trends Pharmacol Sci*, vol. 24, no. 8, pp. 395–401, 2003.

[46] Giulian, D. and Baker, T., "Characterization of ameboid microglia isolated from developing mammalian brain," *J Neurosci*, vol. 6, pp. 2163–78, 1986.

[47] Gonzalez-Scarano, F. and Baltuch, G., "Microglia as mediators of inflammatory and degenerative diseases," *Annu Rev Neurosci*, vol. 22, pp. 219–40, 1999.

[48] Griffith, R. W. and Humphrey, D. R., "Long-term gliosis around chronically implanted platinum electrodes in the rhesus macaque motor cortex," *Neurosci Lett*, vol. 406, no. 1-2, pp. 81–6, 2006.

[49] Grill, W. M. and Mortimer, J. T., "Electrical properties of implant encapsulation tissue," *Ann Biomed Eng*, vol. 22, no. 1, pp. 23–33, 1994.

[50] Grimnes, S. and Martinsen, . G., *Bioimpedance and Bioelectricity Basics*. New York: Academic, 2000.

[51] Hanisch, U. K., "Microglia as a source and target of cytokines," *Glia*, vol. 40, no. 2, pp. 140–55, 2002.

[52] He, W. and Bellamkonda, R. V., "Nanoscale neuro-integrative coatings for neural implants," *Biomaterials*, vol. 26, no. 16, pp. 2983–90, 2005.

[53] He, W. and Bellamkonda, R. V., "A molecular perspective on understanding and modulating the performance of chronic cns recording electrodes. submitted.," 2007.

[54] He, W., McConnell, G. C., and Bellamkonda, R. V., "Nanoscale laminin coating modulates cortical scarring response around implanted silicon microelectrode arrays," *J Neural Eng*, vol. 3, no. 4, pp. 316–26. Both authors contributed equally, 2006.

[55] He, W., McConnell, G. C., Schneider, T. M., and Bellamkonda, R. V., "A novel anti-inflammatory surface for neural electrodes," *Advanced Material*, vol. 19, pp. 3529–3533, 2007.

[56] Hellmich, H. L., Eidson, K. A., Capra, B. A., Garcia, J. M., Boone, D. R., Hawkins, B. E., Uchida, T., Dewitt, D. S., and Prough, D. S., "Injured fluoro-jade-positive hippocampal neurons contain high levels of zinc after traumatic brain injury," *Brain Res*, vol. 1127, no. 1, pp. 119–26, 2007.

[57] Henze, D., Borhegyi, Z., Csicsvari, J., Mamiya, A., Harris, K., and Buzsaki, G., "Intracellular features predicted by extracellular recordings in the hippocampus in vivo," *J Neurophysiol*, vol. 84, pp. 390–400, 2000.

[58] Hetke, J. and Anderson, D., "Silicon microelectrodes for extracellular recording," in *Handbook of Neuroprosthetic Methods*, Boca Raton, FL: CRC Press, 2002.

[59] Hochberg, L. R. and Donoghue, J. P., "Sensors for brain-computer interfaces," *IEEE Eng Med Biol Mag*, vol. 25, no. 5, pp. 32–8, 2006.

[60] Hochberg, L. R., Serruya, M. D., Friehs, G. M., Mukand, J. A., Saleh, M., Caplan, A. H., Branner, A., Chen, D., Penn, R. D., and Donoghue, J. P., "Neuronal ensemble control of prosthetic devices by a human with tetraplegia," *Nature*, vol. 442, no. 7099, pp. 164–71, 2006.

[61] Ignatius, M. J., Sawhney, N., Gupta, A., Thibadeau, B. M., Monteiro, O. R., and Brown, I. G., "Bioactive surface coatings for nanoscale instruments: effects on cns neurons," *J Biomed Mater Res*, vol. 40, no. 2, pp. 264–74, 1998.

[62] James, C., Davis, R., Kam, L., Craighead, H., Isaacson, M., Turner, J. N., and Shain, W., "Patterned protein layers on solid substrates by thin stamp microcontact printing," *Langmuir*, vol. 14, pp. 741–4, 1998.

[63] Jicha, G. A., Lane, E., Vincent, I., Otvos, L., J., Hoffmann, R., and Davies, P., "A conformation- and phosphorylation-dependent antibody recognizing the paired helical filaments of alzheimer's disease," *J Neurochem*, vol. 69, no. 5, pp. 2087–95, 1997.

[64] John, G. R., Lee, S. C., and Brosnan, C. F., "Cytokines: powerful regulators of glial cell activation," *Neuroscientist*, vol. 9, no. 1, pp. 10–22, 2003.

[65] Johnson, M. D., Otto, K. J., and Kipke, D. R., "Repeated voltage biasing improves unit recordings by reducing resistive tissue impedances.," *IEEE Trans Neural Syst Rehabil Eng*, vol. 13, no. 2, pp. 160–5, 2005.

[66] Kim, D. H. and Martin, D. C., "Sustained release of dexamethasone from hydrophilic matrices using plga nanoparticles for neural drug delivery," *Biomaterials*, vol. 27, no. 15, pp. 3031–7, 2006.

[67] Kim, D., Abidian, M., and Martin, D., "Conducting polymers grown in hydrogel scaffolds coated on neural prosthetic devices," *J Biomed Mater Res A*, vol. 71A, no. 4, pp. 577–585, 2004.

[68] Kim, W. G., Mohney, R. P., Wilson, B., Jeohn, G. H., Liu, B., and Hong, J. S., "Regional difference in susceptibility to lipopolysaccharide-induced neurotoxicity in the rat brain: role of microglia," *J Neurosci*, vol. 20, no. 16, pp. 6309–16, 2000.

[69] Kim, Y. T., Hitchcock, R. W., Bridge, M. J., and Tresco, P. A., "Chronic response of adult rat brain tissue to implants anchored to the skull," *Biomaterials*, vol. 25, no. 12, pp. 2229–37, 2004.

[70] Kipke, D. R., Vetter, R. J., Williams, J. C., and Hetke, J. F., "Silicon-substrate intracortical microelectrode arrays for long-term recording of neuronal

spike activity in cerebral cortex," *IEEE Trans Neural Syst Rehabil Eng*, vol. 11, no. 2, pp. 151–5, 2003.

[71] Kitazawa, M., Oddo, S., Yamasaki, T. R., Green, K. N., and LaFerla, F. M., "Lipopolysaccharide-induced inflammation exacerbates tau pathology by a cyclin-dependent kinase 5-mediated pathway in a transgenic model of alzheimer's disease," *J Neurosci*, vol. 25, no. 39, pp. 8843–53, 2005.

[72] Kreutzberg, G. W., "Microglia: a sensor for pathological events in the cns," *Trends Neurosci*, vol. 19, no. 8, pp. 312–8, 1996.

[73] Kyrkanides, S., O'Banion, M. K., Whiteley, P. E., Daeschner, J. C., and Olschowka, J. A., "Enhanced glial activation and expression of specific cns inflammation-related molecules in aged versus young rats following cortical stab injury," *J Neuroimmunol*, vol. 119, no. 2, pp. 269–77, 2001.

[74] Lazarov-Spiegler, O., Rapalino, O., Agranov, G., and Schwartz, M., "Restricted inflammatory reaction in the cns: a key impediment to axonal regeneration?," *Mol Med Today*, vol. 4, no. 8, pp. 337–42, 1998.

[75] Lazarov-Spiegler, O., Solomon, A. S., Zeev-Brann, A. B., Hirschberg, D. L., Lavie, V., and Schwartz, M., "Transplantation of activated macrophages overcomes central nervous system regrowth failure," *FASEB J*, vol. 10, no. 11, pp. 1296–302, 1996.

[76] Lebedev, M. A., Carmena, J. M., O'Doherty, J. E., Zacksenhouse, M., Henriquez, C. S., Principe, J. C., and Nicolelis, M. A., "Cortical ensemble adaptation to represent velocity of an artificial actuator controlled by a brain-machine interface," *J Neurosci*, vol. 25, no. 19, pp. 4681–93, 2005.

[77] Lee, H., Bellamkonda, R., Sun, W., and Levenston, M., "Biomechanical analysis of silicon microelectrode-induced strain in the brain," *J Neural Engineering*, vol. 2, pp. 81–89, 2005.

[78] Lee, V. M., Goedert, M., and Trojanowski, J. Q., "Neurodegenerative tauopathies," *Annu Rev Neurosci*, vol. 24, pp. 1121–59, 2001.

[79] Leung, B., Williamson, T., Chen, C. F., Pollock, A., and Tresco, P. A., "Brain tissue reaction surrounding planar silicon penetrating microelectrode arrays varies as a function of depth in the rat cerebral cortex," in *Society for Neuroscience*, 2006.

[80] Liesi, P., Kaakkola, S., Dahl, D., and Vaheri, A., "Laminin is induced in astrocytes of adult brain by injury," *EMBO J*, vol. 3, no. 3, pp. 683–686, 1984.

[81] Lin, G., Chawla, M. K., Olson, K., Barnes, C. A., Guzowski, J. F., Bjornsson, C., Shain, W., and Roysam, B., "A multi-model approach

to simultaneous segmentation and classification of heterogeneous populations of cell nuclei in 3d confocal microscope images," *Cytometry A*, vol. 71, no. 9, pp. 724–36, 2007.

[82] Liu, B. and Hong, J. S., "Role of microglia in inflammation-mediated neurodegenerative diseases: mechanisms and strategies for therapeutic intervention," *J Pharmacol Exp Ther*, vol. 304, no. 1, pp. 1–7, 2003.

[83] Liu, L., Li, Y., Van Eldik, L. J., Griffin, W. S., and Barger, S. W., "S100b-induced microglial and neuronal il-1 expression is mediated by cell type-specific transcription factors," *J Neurochem*, vol. 92, no. 3, pp. 546–53, 2005.

[84] Liu, X., McCreery, D. B., Carter, R. R., Bullara, L. A., Yuen, T. G., and Agnew, W. F., "Stability of the interface between neural tissue and chronically implanted intracortical microelectrodes," *IEEE Trans Rehabil Eng*, vol. 7, no. 3, pp. 315–26, 1999.

[85] Loeffler, D. A., DeMaggio, A. J., Juneau, P. L., Havaich, M. K., and LeWitt, P. A., "Effects of enhanced striatal dopamine turnover in vivo on glutathione oxidation," *Clin Neuropharmacol*, vol. 17, no. 4, pp. 370–9, 1994.

[86] Lozano, A. M., Dostrovsky, J., Chen, R., and Ashby, P., "Deep brain stimulation for parkinson's disease: disrupting the disruption," *Lancet Neurol*, vol. 1, no. 4, pp. 225–31, 2002.

[87] Ludt, H. and Herrmann, H. D., "In vitro measurement of tissue impedance over a wide frequency range," *Biophysik*, vol. 10, no. 4, pp. 337–45, 1973.

[88] Ludwig, K. A., Uram, J. D., Yang, J., Martin, D. C., and Kipke, D. R., "Chronic neural recordings using silicon microelectrode arrays electrochemically deposited with a poly(3,4-ethylenedioxythiophene) (pedot) film," *J Neural Eng*, vol. 3, no. 1, pp. 59–70, 2006.

[89] Luna-Munoz, J., Garcia-Sierra, F., Falcon, V., Menendez, I., Chavez-Macias, L., and Mena, R., "Regional conformational change involving phosphorylation of tau protein at the thr231, precedes the structural change detected by alz-50 antibody in alzheimer's disease," *J Alzheimers Dis*, vol. 8, no. 1, pp. 29–41, 2005.

[90] Mandelkow, E. M., Stamer, K., Vogel, R., Thies, E., and Mandelkow, E., "Clogging of axons by tau, inhibition of axonal traffic and starvation of synapses," *Neurobiol Aging*, vol. 24, no. 8, pp. 1079–85, 2003.

[91] Massia, S. P., Holecko, M. M., and Ehteshami, G. R., "In vitro assessment of bioactive coatings for neural implant applications," *J Biomed Mater Res*, vol. 68A, pp. 177–86, 2003.

[92] Massia, S., Holecko, M., and Ehteshami, G., "In vitro assessment of bioactive coatings for neural implant applications," *J Biomed Mater Res A*, vol. 68, no. 1, pp. 177–86, 2004.

[93] McConnell, G. C., Schneider, T. M., Owens, D. J., and Bellamkonda, R. V., "Extraction force and cortical tissue reaction of silicon microelectrode arrays implanted in the rat brain," *IEEE Trans Biomed Eng*, vol. 54, no. 6 Pt 1, pp. 1097–107, 2007.

[94] McGree, J. M., Duffull, S. B., Eccleston, J. A., and Ward, L. C., "Optimal designs for studying bioimpedance," *Physiol Meas*, vol. 28, no. 12, pp. 1465–83, 2007.

[95] Melov, S., Adlard, P. A., Morten, K., Johnson, F., Golden, T. R., Hinerfeld, D., Schilling, B., Mavros, C., Masters, C. L., Volitakis, I., Li, Q. X., Laughton, K., Hubbard, A., Cherny, R. A., Gibson, B., and Bush, A. I., "Mitochondrial oxidative stress causes hyperphosphorylation of tau," *PLoS ONE*, vol. 2, no. 6, p. e536, 2007.

[96] Merrill, D. R. and Tresco, P. A., "Impedance characterization of microarray recording electrodes in vitro," *IEEE Trans Biomed Eng*, vol. 52, no. 11, pp. 1960–5, 2005.

[97] Miklavcic, D., Pavselj, N., and Hart, F. X., "Electric properties of tissues," in *Wiley Encyclopedia of Biomedical Engineering*, p. 357889, John Wiley & Sons, Inc., 2006.

[98] Minghetti, L., Ajmone-Cat, M. A., De Berardinis, M. A., and De Simone, R., "Microglial activation in chronic neurodegenerative diseases: roles of apoptotic neurons and chronic stimulation," *Brain Res Brain Res Rev*, vol. 48, no. 2, pp. 251–6, 2005.

[99] Moe, A., Marx, S., Bhinderwala, I., and Wilson, D., "A miniaturized lock-in amplifier design suitable for impedance measurements in cells," in *IEEE Sensors*, (Vienna, Austria), 2004.

[100] Nicolelis, M. A., Dimitrov, D., Carmena, J. M., Crist, R., Lehew, G., Kralik, J. D., and Wise, S. P., "Chronic, multisite, multielectrode recordings in macaque monkeys," *Proc Natl Acad Sci U S A*, vol. 100, no. 19, pp. 11041–6, 2003.

[101] O'Connell, M. J., Baum, H., and Peters, T. J., "Haemosiderin-like properties of free-radical-modified ferritin," *Biochem J*, vol. 240, no. 1, pp. 297–300, 1986.

[102] Oh, S., Smith, K., Bjornsson, C., Turner, J., Song, J., Kim, S., and Shain, W., "Regional differences of reactive responses against silicon neural probe implanted into deep brain regions," (Bethesda, MD), Neural Prosthesis Workshop, October 2003.

[103] Osterman, K. S., Paulsen, K. D., and Hoopes, P. J., "Application of linear circuit models to impedance spectra in irradiated muscle," *Ann N Y Acad Sci*, vol. 873, pp. 21–9, 1999.

[104] Otani, N., Nawashiro, H., Fukui, S., Ooigawa, H., Ohsumi, A., Toyooka, T., Shima, K., Gomi, H., and Brenner, M., "Enhanced hippocampal neurodegeneration after traumatic or kainate excitotoxicity in gfap-null mice," *J Clin Neurosci*, vol. 13, no. 9, pp. 934–8, 2006.

[105] Otto, K. J., Johnson, M. D., and Kipke, D. R., "Voltage pulses change neural interface properties and improve unit recordings with chronically implanted microelectrodes.," *IEEE Trans Biomed Eng*, vol. 53, no. 2, pp. 333–40, 2006.

[106] Parvathenani, L. K., Tertyshnikova, S., Greco, C. R., Roberts, S. B., Robertson, B., and Posmantur, R., "P2x7 mediates superoxide production in primary microglia and is up-regulated in a transgenic mouse model of alzheimer's disease," *J Biol Chem*, vol. 278, no. 15, pp. 13309–17, 2003.

[107] Paxinos, G. and Watson, C., *The Rat Brain in Stereotaxic Coordinates*. San Diego, CA: Academic, 1997.

[108] Piper, M., Abrams, G., and Marks, Jr., W., "Deep brain stimulation for the treatment of parkinson's disease: overview and impact on gait and mobility," *NeuroRehabilitation*, vol. 20, pp. 223–232, 2005.

[109] Pliquett, F. and Pliquett, U., "Stress action on biological tissue and tissue models detected by the py value," *Ann N Y Acad Sci*, vol. 873, pp. 227–38, 1999.

[110] Polikov, V. S., Tresco, P. A., and Reichert, W. M., "Response of brain tissue to chronically implanted neural electrodes," *J Neurosci Methods*, vol. 148, no. 1, pp. 1–18, 2005.

[111] Qin, L., Liu, Y., Cooper, C., Liu, B., Wilson, B., and Hong, J. S., "Microglia enhance beta-amyloid peptide-induced toxicity in cortical and mesencephalic neurons by producing reactive oxygen species," *J Neurochem*, vol. 83, no. 4, pp. 973–83, 2002.

[112] Rauschecker, J. and Shannon, R., "Sending sound to the brain," *Science*, vol. 295, pp. 1025–1029, 2002.

[113] Robinson, D., "The electrical properties of metal microelectrodes," *Proc IEEE*, vol. 56, pp. 1065–1071, 1968.

[114] Roitbak, T. and Sykova, E., "Diffusion barriers evoked in the rat cortex by reactive astrogliosis," *Glia*, vol. 28, no. 1, pp. 40–8, 1999.

[115] Rousche, P. J. and Normann, R. A., "Chronic recording capability of the utah intracortical electrode array in cat sensory cortex," *J Neurosci Methods*, vol. 82, no. 1, pp. 1–15, 1998.

[116] Rousche, P. J., Pellinen, D. S., Pivin, D. P., J., Williams, J. C., Vetter, R. J., and Kipke, D. R., "Flexible polyimide-based intracortical electrode arrays with bioactive capability," *IEEE Trans Biomed Eng*, vol. 48, no. 3, pp. 361–71, 2001.

[117] Rousche, P. and Normann, R., "Chronic recording capability of the utah intracortical electrode array in cat sensory cortex," *J Neurosci Methods*, vol. 82, p. 115, 1998.

[118] Rutten, W., van Wier, H., and Put, J., "Sensitivity and selectivity of intraneural stimulation using a silicon electrode array," *IEEE Trans Biomed Eng*, vol. 38, pp. 192–198, 1991.

[119] Santhanam, G., Ryu, S., Yu, B., Afshar, A., and Shenoy, K., "A high-performance brain-computer interface," *Nature*, vol. 442, no. 7099, pp. 195–198, 2006.

[120] Schindowski, K., Bretteville, A., Leroy, K., Begard, S., Brion, J. P., Hamdane, M., and Buee, L., "Alzheimer's disease-like tau neuropathology leads to memory deficits and loss of functional synapses in a novel mutated tau transgenic mouse without any motor deficits," *Am J Pathol*, vol. 169, no. 2, pp. 599–616, 2006.

[121] Schmued, L. C., Stowers, C. C., Scallet, A. C., and Xu, L., "Fluorojade c results in ultra high resolution and contrast labeling of degenerating neurons," *Brain Res*, vol. 1035, no. 1, pp. 24–31, 2005.

[122] Schultz, R. L. and Willey, T. J., "The ultrastructure of the sheath around chronically implanted electrodes in brain," *J Neurocytol*, vol. 5, no. 6, pp. 621–42, 1976.

[123] Schwan, H. P., "Electrical properties of tissue and cell suspensions," *Adv Biol Med Phys*, vol. 5, pp. 147–209, 1957.

[124] Schwartz, A. B., "Cortical neural prosthetics," *Annu Rev Neurosci*, vol. 27, pp. 487–507, 2004.

[125] Scott, S. H., "Neuroscience: converting thoughts into action," *Nature*, vol. 442, no. 7099, pp. 141–2, 2006.

[126] Serruya, M. D., Hatsopoulos, N. G., Paninski, L., Fellows, M. R., and Donoghue, J. P., "Instant neural control of a movement signal," *Nature*, vol. 416, no. 6877, pp. 141–2, 2002.

[127] Seymour, J. P. and Kipke, D. R., "Neural probe design for reduced tissue encapsulation in cns," *Biomaterials*, vol. 28, no. 25, pp. 3594–607, 2007.

[128] Shain, W., Spataro, L., Dilgen, J., Haverstick, K., Retterer, S., Isaacson, M., Saltzman, M., and Turner, J. N., "Controlling cellular reactive responses around neural prosthetic devices using peripheral and local intervention strategies," *IEEE Trans Neural Syst Rehabil Eng*, vol. 11, no. 2, pp. 186–8, 2003.

[129] Shellswell, G., Restall, D., Duance, V., and Bailey, A., "Identification and differential distribution of collagen types in the central and peripheral nervous systems," *FEBS Letters*, vol. 106, no. 2, pp. 305–308, 1979.

[130] Silver, J. and Miller, J., "Regeneration beyond the glial scar," *Nat Rev Neurosci*, vol. 5, pp. 146–156, 2004.

[131] Spataro, L., Dilgen, J., Retterer, S., Spence, A. J., Isaacson, M., Turner, J. N., and Shain, W., "Dexamethasone treatment reduces astroglia responses to inserted neuroprosthetic devices in rat neocortex," *Exp Neurol*, vol. 194, no. 2, pp. 289–300, 2005.

[132] Spataro, L., Dilgen, J., Retterer, S., Spence, A., Isaacson, M., Turner, J., and Shain, W., "Dexamethasone treatment reduces astroglia responses to inserted neuroprosthetic devices in rat neocortex," *Exp Neurol*, vol. 194, pp. 289–300, 2005.

[133] Subbaroyan, J., Martin, D., and Kipke, D., "A finite-element model of the mechanical effects of implantable microelectrodes in the cerebral cortex," *J Neural Engineering*, vol. 2, pp. 103–113, 2005.

[134] Sun, D. A., Yu, H., Spooner, J., Tatsas, A. D., Davis, T., Abel, T. W., Kao, C., and Konrad, P. E., "Postmortem analysis following 71 months of deep brain stimulation of the subthalamic nucleus for parkinson disease," *J Neurosurg*, vol. 109, no. 2, pp. 325–9, 2008.

[135] Suner, S., Fellows, M. R., Vargas-Irwin, C., Nakata, G. K., and Donoghue, J. P., "Reliability of signals from a chronically implanted, silicon-based electrode array in non-human primate primary motor cortex," *IEEE Trans Neural Syst Rehabil Eng*, vol. 13, no. 4, pp. 524–41, 2005.

[136] Suo, Z., Wu, M., Citron, B. A., Palazzo, R. E., and Festoff, B. W., "Rapid tau aggregation and delayed hippocampal neuronal death induced by persistent thrombin signaling," *J Biol Chem*, vol. 278, no. 39, pp. 37681–9, 2003.

[137] Sykova, E., "Glia and volume transmission during physiological and pathological states," *J Neural Transm*, vol. 112, no. 1, pp. 137–47, 2005.

[138] Sykova, E., Vargova, L., Prokopova, S., and Simonova, Z., "Glial swelling and astrogliosis produce diffusion barriers in the rat spinal cord," *Glia*, vol. 25, no. 1, pp. 56–70, 1999.

[139] Szarowski, D. H., Andersen, M. D., Retterer, S., Spence, A. J., Isaacson, M., Craighead, H. G., Turner, J. N., and Shain, W., "Brain responses to micro-machined silicon devices," *Brain Res*, vol. 983, no. 1-2, pp. 23–35, 2003.

[140] Tagliati, M., Shils, J., Sun, C., and Alterman, R., "Deep brain stimulation for dystonia," *Expert Rev Med Devices*, vol. 1, pp. 33–41, 2004.

[141] Taylor, D. M., Tillery, S. I., and Schwartz, A. B., "Direct cortical control of 3d neuroprosthetic devices," *Science*, vol. 296, no. 5574, pp. 1829–32, 2002.

[142] Turner, J. N., Shain, W., Szarowski, D. H., Andersen, M., Martins, S., Isaacson, M., and Craighead, H., "Cerebral astrocyte response to micromachined silicon implants," *Exp Neurol*, vol. 156, no. 1, pp. 33–49, 1999.

[143] Vetter, R. J., Williams, J. C., Hetke, J. F., Nunamaker, E. A., and Kipke, D. R., "Chronic neural recording using silicon-substrate microelectrode arrays implanted in cerebral cortex," *IEEE Trans Biomed Eng*, vol. 51, no. 6, pp. 896–904, 2004.

[144] Vincent, I., Zheng, J. H., Dickson, D. W., Kress, Y., and Davies, P., "Mitotic phosphoepitopes precede paired helical filaments in alzheimer's disease," *Neurobiol Aging*, vol. 19, no. 4, pp. 287–96, 1998.

[145] Wadhwa, R., Lagenaur, C., and Cui, X., "Electrochemically controlled release of dexamethasone from conducting polymer polypyrrole coated electrode," *J Control Rel*, vol. 110, no. 3, pp. 531–541, 2006.

[146] Ward, L. C., Essex, T., and Cornish, B. H., "Determination of cole parameters in multiple frequency bioelectrical impedance analysis using only the measurement of impedances," *Physiol Meas*, vol. 27, no. 9, pp. 839–50, 2006.

[147] Weaver, C. L., Espinoza, M., Kress, Y., and Davies, P., "Conformational change as one of the earliest alterations of tau in alzheimer's disease," *Neurobiol Aging*, vol. 21, no. 5, pp. 719–27, 2000.

[148] Weldon, D. T., Rogers, S. D., Ghilardi, J. R., Finke, M. P., Cleary, J. P., O'Hare, E., Esler, W. P., Maggio, J. E., and Mantyh, P. W., "Fibrillar beta-amyloid induces microglial phagocytosis, expression of inducible nitric oxide synthase, and loss of a select population of neurons in the rat cns in vivo," *J Neurosci*, vol. 18, no. 6, pp. 2161–73, 1998.

[149] Wessberg, J., Stambaugh, C. R., Kralik, J. D., Beck, P. D., Laubach, M., Chapin, J. K., Kim, J., Biggs, S. J., Srinivasan, M. A., and Nicolelis, M. A., "Real-time prediction of hand trajectory by ensembles of cortical neurons in primates," *Nature*, vol. 408, no. 6810, pp. 361–5, 2000.

[150] Williams, J. C., *Performance of Chronic Neural Implants*. PhD thesis, 2001.

[151] Williams, J. C., Hippensteel, J., Dilgen, J., Shain, W., and Kipke, D. R., "Complex impedance spectroscopy for monitoring tissue responses to inserted neural implants," *Journal of Neural Engineering*, vol. 4, pp. 410–423, 2007.

[152] Williams, J. C., Rennaker, R. L., and Kipke, D. R., "Long-term neural recording characteristics of wire microelectrode arrays implanted in cerebral cortex," *Brain Res Brain Res Protoc*, vol. 4, no. 3, pp. 303–13, 1999.

[153] Wilms, H., Zecca, L., Rosenstiel, P., Sievers, J., Deuschl, G., and Lucius, R., "Inflammation in parkinson's diseases and other neurodegenerative diseases: cause and therapeutic implications," *Curr Pharm Des*, vol. 13, no. 18, pp. 1925–8, 2007.

[154] Wu, D. C., Teismann, P., Tieu, K., Vila, M., Jackson-Lewis, V., Ischiropoulos, H., and Przedborski, S., "Nadph oxidase mediates oxidative stress in the 1-methyl-4-phenyl-1,2,3,6-tetrahydropyridine model of parkinson's disease," *Proc Natl Acad Sci U S A*, vol. 100, no. 10, pp. 6145–50, 2003.

[155] Wyss-Coray, T., "Inflammation in alzheimer disease: driving force, bystander or beneficial response?," *Nat Med*, vol. 12, no. 9, pp. 1005–15, 2006.

[156] Xiao, Y., Cui, X., and Martin, D., "Electrochemical polymerization and properties of pedot/s-edot on neural microelectrode arrays," *J Electroanalytical Chemistry*, vol. 573, no. 1, pp. 43–48, 2004.

[157] Yang, J., Kim, D., Hendricks, J., Leach, M., Northey, R., and Martin, D., "Ordered surfactant-templated poly(3,4-ethylenedioxythiophene) (pedot) conducting polymer on microfabricated neural probes," *Acta Biomaterialia*, vol. 1, pp. 125–136, 2005.

[158] Yang, J. and Martin, D., "Microporous conducting polymers on neural microelectrode arrays - i - electrochemical deposition.," *Sensors and Actuators B-Chemical*, vol. 101, no. 1-2, pp. 133–142, 2004.

[159] Yang, J. and Martin, D., "Microporous conducting polymers on neural microelectrode arrays ii. physical characterization.," *Sensors and Actuators A-Physical*, vol. 113, no. 2, pp. 204–211, 2004.

[160] Yoshiyama, Y., Higuchi, M., Zhang, B., Huang, S. M., Iwata, N., Saido, T. C., Maeda, J., Suhara, T., Trojanowski, J. Q., and Lee,

V. M., "Synapse loss and microglial activation precede tangles in a p301s tauopathy mouse model," *Neuron*, vol. 53, no. 3, pp. 337–51, 2007.

[161] Yuen, T. G. and Agnew, W. F., "Histological evaluation of polyesterimide-insulated gold wires in brain," *Biomaterials*, vol. 16, no. 12, pp. 951–6, 1995.

[162] Zeev-Brann, A. B., Lazarov-Spiegler, O., Brenner, T., and Schwartz, M., "Differential effects of central and peripheral nerves on macrophages and microglia," *Glia*, vol. 23, no. 3, pp. 181–90, 1998.

[163] Zekry, D., Epperson, T. K., and Krause, K. H., "A role for nox nadph oxidases in alzheimer's disease and other types of dementia?," *IUBMB Life*, vol. 55, no. 6, pp. 307–13, 2003.

[164] Zhao, W., Xie, W., Le, W., Beers, D. R., He, Y., Henkel, J. S., Simpson, E. P., Yen, A. A., Xiao, Q., and Appel, S. H., "Activated microglia initiate motor neuron injury by a nitric oxide and glutamate-mediated mechanism," *J Neuropathol Exp Neurol*, vol. 63, no. 9, pp. 964–77, 2004.

[165] Zhong, Y. and Bellamkonda, R. V., "Controlled release of anti-inflammatory agent alpha-msh from neural implants," *J Control Release*, vol. 106, no. 3, pp. 309–18, 2005.

[166] Zhong, Y., McConnell, G., Ross, J., DeWeerth, S., and Bellamkonda, R., "A novel dexamethasone-releasing, antiinflammatory coating for neural implants," *Proc of the 2nd Intl IEEE EMBS Conf on Neural Eng*, 2005.